



HAL
open science

Development of testing methods for characterization of delamination behavior under pure mode III and mixed modes in a laminated composite

Yangyang Ge

► **To cite this version:**

Yangyang Ge. Development of testing methods for characterization of delamination behavior under pure mode III and mixed modes in a laminated composite. Mechanics of materials [physics.class-ph]. Université Paul Sabatier - Toulouse III, 2016. English. NNT : 2016TOU30130 . tel-01490573

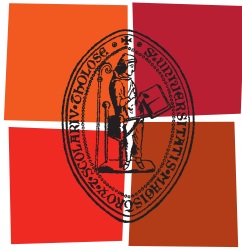
HAL Id: tel-01490573

<https://theses.hal.science/tel-01490573>

Submitted on 15 Mar 2017

HAL is a multi-disciplinary open access archive for the deposit and dissemination of scientific research documents, whether they are published or not. The documents may come from teaching and research institutions in France or abroad, or from public or private research centers.

L'archive ouverte pluridisciplinaire **HAL**, est destinée au dépôt et à la diffusion de documents scientifiques de niveau recherche, publiés ou non, émanant des établissements d'enseignement et de recherche français ou étrangers, des laboratoires publics ou privés.



Université
de Toulouse

THÈSE

En vue de l'obtention du

DOCTORAT DE L'UNIVERSITÉ DE TOULOUSE

Délivré par :

Université Toulouse 3 Paul Sabatier (UT3 Paul Sabatier)



Présentée et soutenue par :

M. YANGYANG GE

Le mercredi 28 septembre 2016

Titre :

DEVELOPMENT OF TESTING METHODS FOR CHARACTERIZATION OF
DELAMINATION BEHAVIOR UNDER PURE MODE III AND MIXED MODES IN A
LAMINATED COMPOSITE

ED MEGEP : Génie mécanique, mécanique des matériaux



Unité de recherche :

Institut Clément Ader

Directeur(s) de Thèse :

Mme. XIAOJING GONG

Mme. ANITA HUREZ

M. EMMANUEL DE LUYCKER

Rapporteurs :

M. JACQUES LAMON, Rapporteur

M. ROSTAND MOUTOU PITTI, Rapporteur

Autre(s) membre(s) du jury :

M. LAURENT MICHEL, Examineur

M. SHAHRAM AIVAZZADEH, Examineur

M. ZOHEIR ABOURA, Examineur

ACKNOWLEDGEMENTS

First of all, I would like to express my sincere and heartfelt thanks to Professor Gong XiaoJing, Professor De Luycker Emmanuel and Professor Hurez Anita for their patience and guidance through my studies during the thesis. They have tried their best to help me get over the difficulties.

Sincere appreciation is extended to Professor LAMON Jacques and Professor MOUTOU PITTI Rostand for their willingness to be the reviewers of my thesis. I gratefully appreciate Professor AIVAZZADEH Shahram, Professor ABOURA Zoheir and Professor MICHEL Laurent for their willingness to be the members of jury. Their valuable comments and suggestions are highly acknowledged.

I am indebted to many of the academic, administrative and technical staff at Clément Ader Institute and IUT Tarbes. Special thanks to M. RUIZ Marc for his support to make experimental devices; to Mme PERRIN Marianne for her help in destructive testing experiments; to M. CANTAREL Arthur for his generosity in sharing knowledge of resin. Thanks to all the technicians for assisting me to use testing machines. Not to forget Madam DURAN Patricia in secretariat who is always there whenever I need help.

To all the colleagues and friends, thank you very much.

Five-year financial support is provided by the China Scholarship Council.

My deepest appreciation is delivered to my family members for all their sacrifices, love and care throughout all these years. You are always the source of power in my life.

Table of contents

CHAPTER I. INTRODUCTION	12
CHAPTER II. LITTERATURE REVIEW	17
II.1. Introduction	17
II.2. Mechanisms of damage and fracture of laminated composite.....	17
II.2.1. The principal mechanisms of damage in a single ply.....	17
II.2.2. Delamination	21
II.2. Fracture criteria.....	23
II.2.1. Criteria without stress interaction.....	23
II.2.2. Interactive criteria.....	23
II.2.3. Semi-interactive criteria.....	24
II.2.4. Mixed mode delamination criteria.....	26
II.3. Delamination tests under pure mode I, II, III and mixed mode I+II+III	28
II.3.1. Introduction	28
II.3.2. Pure mode I.....	28
II.3.3. Pure mode II	28
II.3.4. Pure mode III.....	29
II.3.4.1. Crack Rail Shear test	29
II.3.4.2. Split Cantilever Beam.....	30
II.3.4.3. Edge Crack Torsion	34
II.3.4.4. Torque Shell (TS) fixture	36
II.3.4.5. Comparison and conclusions	38
II.3.5. Mixed mode I+II+III	39
II.3.6. Summary.....	41
II.4. Finite element analysis for simulation of delamination behavior.....	41
II.4.1. VCCT method to calculate strain energy release rate	41
II.4.2. J-integral method	42
II.4.3. Perturbation method	43
II.4.4. Cohesive Zone Model.....	44
II.4.5. Summary.....	45
II.5. Summary.....	45
CHAPTER III. PRELIMINARY STUDY	47
III.1. Materials and laminate manufacturing.....	47

III.2. Composite materials characterization	47
III.2.1. Characterization tests	47
III.2.2. Experimental	47
III.2.3. Results and discussions	48
III.3. Establishment of the finite element models	49
III.4. Tests of delamination under pure mode I (DCB) and pure mode II (ENF)	51
III.4.1. Experimental	51
III.4.2. Finite element analysis	55
III.4.3. Results and discussions	56
III.4.4. Conclusions	60
CHAPTER IV. STUDY OF DELAMINATION UNDER PURE MODE III	62
IV.1. Pure mode III delamination tests proposed in literature	62
IV.1.1. Edge Crack Torsion-1 (ECT-1) test	62
IV.1.1.1. Experimental	62
IV.1.1.2. Finite element analysis	63
IV.1.1.3. Results and discussions	64
IV.1.1.4. Conclusions	68
IV.1.2. Edge Crack Torsion -2 (ECT-2) test	68
IV.1.2.1. Experimental	68
IV.1.2.2. Finite element analysis	69
IV.1.2.3. Results and discussions	70
IV.1.2.4. Conclusions	73
IV.2. Edge Ring Crack Torsion (ERCT or ERC-III) test	73
IV.2.1. Introduction	73
IV.2.2. Experimental	74
IV.2.3. Finite element analysis	77
IV.2.4. Results and discussions	79
IV.2.5. Conclusions	82
IV.3. Factors affecting the evolution of G_{III} along the crack front of ERCT test	83
IV.3.1. Influence factor from the device	83
IV.3.2. Influence factor due to the nature of the laminate	85
IV.3.3. Influence factor due to ratio d/D_{ring}	86
IV.3.4. Combination of influence factors	88
IV.3.5. Optimization of the device	89
IV.3.6. Conclusions	90
IV.4. Modified Edge Ring Crack Torsion tests	90
IV.4.1. Experimental	90

IV.4.1.1. ERC-III-1 test.....	91
IV.4.1.2. ERC-III-2 test.....	92
IV.4.2. Sensitivity to the defaults of the geometry of the specimen and the device	94
IV.4.2.1. Outer shape of the specimen	95
IV.4.2.2. Circularity of the crack front.....	96
IV.4.2.3. Relative position of the crack front.....	97
IV.4.3. Data reduction methods	99
IV.4.4. Results and discussions	100
IV.4.4.1. Modified Edge Ring Crack Torsion-1 (ERC-III-1) test.....	100
IV.4.4.2. Modified Edge Ring Crack Torsion-2 (ERC-III-2) test.....	100
IV.4.5. Conclusions	103
IV.5. Conclusions.....	104
IV.5.1. Comparison of pure mode III toughness G_{IIIc} obtained by different methods	104
IV.5.2. Comparison of G_{IC} , G_{IIc} and G_{IIIc}	106
CHAPTER V. DELAMINATION UNDER PURE MODE I, PURE MODE II AND MIXED MODE USING MODIFIED EDGE RING CRACK SPECIMEN	108
V.1. Pure mode I and pure mode II.....	108
V.1.1. Experimental	108
V.1.2. Finite element analysis	109
V.1.3. Results and discussions	110
V.1.3.1. Edge Ring Crack mode I test (ERC-I).....	110
V.1.3.2. Edge Ring Crack mode II test (ERC-II).....	112
V.1.4. Conclusions	114
V.2. Mixed mode I+II	114
V.2.1. Introduction	114
V.2.2. Finite element analysis	115
V.2.3. Results and discussions	115
V.2.4. Summary	116
V.3. Tests of delamination under mixed mode I+III.....	116
V.3.1. Introduction	116
V.3.2. Finite element analysis	116
V.3.3. Results and discussions	116
V.3.4. Summary	117
V.4. Delamination tests under mixed mode I+II+III.....	117
V.4.1. Introduction	117
V.4.2. Finite element analysis	117
V.4.3. Results and discussions	118

V.4.4. Summary	118
V.5. Conclusions	118
CHAPTER VI. CONCLUSIONS AND PERSPECTIVES.....	120
VI.1. Concluding remarks	120
VI.2. Suggestions for future work.....	122
REFERENCE	123

List of Figures

Figure I. 1. Young's modulus and shear modulus for the laminate in membrane	14
Figure I. 2. Young's modulus and shear modulus for the laminate in flexion	15
Figure II. 1. Longitudinal traction: fiber fracture ^[3]	17
Figure II. 2. (a) Transverse fracture of matrix (b) shear fracture of matrix (c) debonding of the fiber-matrix interface (d) longitudinal fracture of the matrix ^[3]	18
Figure II. 3. Local buckling of a fiber	18
Figure II. 4. Longitudinal traction: transverse fracture of the matrix ^[3]	19
Figure II. 5. Longitudinal traction: longitudinal fracture of the matrix ^[3]	19
Figure II. 6. Longitudinal traction: fracture of the fiber-matrix interface ^[3]	20
Figure II. 7. Crack growth in the case of strong adhesion fiber-matrix ^[3]	20
Figure II. 8. Crack growth in the case of weak adhesion fiber-matrix ^[3]	21
Figure II. 9. Fracture of a unidirectional composite under transverse traction ^[3]	21
Figure II. 10. Mechanism of fracture observed in a laminate composite	22
Figure II. 11. Three basic fracture modes	22
Figure II. 12. Experimental compliance calibration	23
Figure II. 13. Typical set-up for DCB test	28
Figure II. 14. Typical set-up for ENF test	29
Figure II. 15. Crack Rail Shear specimen geometry ^[22]	30
Figure II. 16. Typical spilt cantilever beam test ^[23]	31
Figure II. 17. test jig used for modified SCB test ^[25]	32
Figure II. 18. 3D view of the experimental equipment. Assembled state (a) and exploded view(b) ^[28]	33
Figure II. 19. Schematic illustration of the MSCB specimen ^[28]	33
Figure II. 20. Geometry of the MSCB specimen with small edge delamination ^[31]	34
Figure II. 21. Schematic of ECT specimen	34
Figure II. 22. ECT-1 specimen and test fixture ^[38]	35
Figure II. 23. MECT-1 specimen and test fixture ^[38]	35
Figure II. 24. Photograph and schematic diagram of test fixture ^[44]	36
Figure II. 25. Exploded view of the test specimen obtained by bonding of two rectangular plates (left) and cross section of the circular-shaped adhesive joint (right). ^[50]	37
Figure II. 26. Exploded view of the shells and of the specimen being tested. ^[50]	37
Figure II. 27. Layout of the testing apparatus ^[50]	38
Figure II. 28. The mixed-mode I/II/III PENF specimen (d) as the superposition of the DCB (a), ENF (b) and MSCB (c) specimens	39
Figure II. 29. The mixed-mode I/II/III Double-Prestressed End-notched Flexure specimen	40
Figure II. 30 STB specimen and loading ^[31]	40
Figure II. 31 Schematic of test set-up ^[31]	41
Figure II. 32 VCCT for three dimensional eight-nodded solid elements. ^[55]	42
Figure II. 33 Contour for evaluation of J-integral.	43
Figure II. 34. Cohesive Zone Model.....	44
Figure II. 35. Various forms of TSLC laws.....	45

Figure III. 1. Experimental load/displacement curve for the specimens 0 ° and 90 °	49
Figure III. 2. Experimental load/displacement curve for the specimen 45 °	49
Figure III. 3. Schema of Double Cantilever Beam test	51
Figure III. 4. A picture of DCB specimen and test	52
Figure III. 5. Schema of End Notched Flexion test	54
Figure III. 6. A picture of ENF test	54
Figure III. 7. Mesh for DCB test	55
Figure III. 8. Mesh for ENF test	56
Figure III. 9. An experimental load-displacement curve in DCB test	56
Figure III. 10. Interpolation of C/a^3 for Beam compliance law (Eq. 36)	57
Figure III. 11. Interpolation of C/a for Berry compliance law (Eq. 35)	57
Figure III. 12. Evolution of G_I , G_{II} and G_{III} along the crack front of DCB specimen and comparison of the average value of G_{IC} from different methods	58
Figure III. 13. An experimental load-displacement curve in ENF test	59
Figure III. 14. Interpolation of C/a^3 for Beam model compliance law (Eq. 36)	59
Figure III. 15. Evolution of G_I , G_{II} and G_{III} along the crack front of ENF specimen and comparison of the average value of G_{IIC} from different methods	60
Figure IV. 1. Schematic of ECT-1 test	62
Figure IV. 2. A picture of ECT-1 test	63
Figure IV. 3. Finite element model of ECT-1 test	64
Figure IV. 4. (a) Experimental load-displacement curves; (b) Omniscan image of ECT-1 specimen	65
Figure IV. 5. Interpolation between $1/C$ and a/B	65
Figure IV. 6. Evolution of G_I , G_{II} and G_{III} along the crack front of ECT-1 test	66
Figure IV. 7. SEM observations in ECT-1 specimen	67
Figure IV. 8. Model of MECT-1 test	67
Figure IV. 9. Evolution of G_I , G_{II} and G_{III} normalized by G_T along the crack front in the MECT-1 test	68
Figure IV. 10. Schema of Edge Crack Torsion-2 test (ECT-2)	69
Figure IV. 11. Model of ECT-2 test	70
Figure IV. 12. Schematic of ECT-2 test	70
Figure IV. 13. Experimental torque/rotation curves and Omniscan image of ECT-2 test ...	71
Figure IV. 14. Interpolation of $(1/C)$ vs (a/B) (Eq. 41)	72
Figure IV. 15. Comparison of G_{IIC} results from ECT-2 test	72
Figure IV. 16. Evolution of G_I , G_{II} and G_{III} along the crack front of ECT-2 specimen	73
Figure IV. 17. Schema of ERCT specimen	74
Figure IV. 18. Definition of d , d_{ring} and D_{ring}	74
Figure IV. 19. Rigid plates in the device of ERCT	75
Figure IV. 20. Schema of ERCT device	75
Figure IV. 21. A picture of ERCT test	76
Figure IV. 22. Cylindrical beam with a ring crack	76
Figure IV. 23. Bilinear TSLC law used in cohesive element model	77
Figure IV. 24. Mesh of ERCT specimen	78
Figure IV. 25. Model of ERCT test	79
Figure IV. 26. Experimental torque-rotation curves of ERCT specimen with $d=30\text{mm}$	79
Figure IV. 27. Ultrasonic C-scan image before and after propagation on the three ERCT specimens with $d=30\text{mm}$	80
Figure IV. 28. Definition of angle Θ between fiber orientation and crack front	80

Figure IV. 29. Evolution of G_I , G_{II} and G_{III} along the circular crack front of ERCT specimen with $d=30\text{mm}$	81
Figure IV. 30. Evolution of G_I , G_{II} and G_{III} along the circular crack front of ERCT specimen with $d=50\text{mm}$	82
Figure IV. 31: Cohesive element model for ERCT specimen	82
Figure IV. 32. Finite element models of device A and C	84
Figure IV. 33. Evolution of normalized G_{III} along the circular crack front with device A and C	85
Figure IV. 34. Top view of ERCT device	85
Figure IV. 35. Evolution of normalized G_{III} along the circular crack front with device C and steel and composite specimens	86
Figure IV. 36. Evolution of normalized G_{III} along the circular crack front with device A and different diameters of steel specimens	87
Figure IV. 37. Evolution of normalized G_{III} along the circular crack front with device C and different diameters of composite specimens	87
Figure IV. 38. Δ vs d/D_{ring}	88
Figure IV. 39. Evolution of normalized G_{III} along the circular crack front with device C and A	89
Figure IV. 40. Models for device B and B45	89
Figure IV. 41. Evolution of normalized G_{III} along the circular crack front with device	90
Figure IV. 42. Schema of MERCT test	91
Figure IV. 43. A picture of ERC-III-1 device and specimen	91
Figure IV. 44. A picture of ERC-III-1 test	92
Figure IV. 45. Dimensions of ERC-III-2 specimen	93
Figure IV. 46. Schematic of ERC-III-2 test	93
Figure IV. 47. Specimen and device of ERC-III-2 test	93
Figure IV. 48. A picture of ERC-III-2 test	94
Figure IV. 49. Model of MERCT test	95
Figure IV. 50. Evolution along the crack front of G_{III} normalized by the average value with round specimen and square specimen	95
Figure IV. 51. Evolution along the crack front of G_I , G_{II} and G_{III} normalized by G_T with oval crack front	96
Figure IV. 52. Evolution along the crack front of G_{III} normalized by the average value with oval and circular crack front	96
Figure IV. 53. Evolution along the crack front of G_I , G_{II} and G_{III} normalized by G_T with inclined crack front	97
Figure IV. 54. Evolution along the crack front of G_{III} normalized by the average value with parallel and inclined crack front	98
Figure IV. 55. Evolution along the crack front of G_I , G_{II} and G_{III} normalized by G_T with loading axis deviation	99
Figure IV. 56. Evolution along the crack front of G_{III} normalized by its average value with and without the default of the alignment	99
Figure IV. 57. Typical experimental torque/rotation angle curve of ERC-III-1 test	100
Figure IV. 58. Typical experimental torque/rotation angle curve of ERC-III-2 test	101
Figure IV. 59. Evolution along the crack front of G_{III} normalized by the average value obtained from ERCT test and from ERC-III-1 test	102
Figure IV. 60. Evolution along the crack front of G_I , G_{II} and G_{III} normalized by G_T obtained from ERC-III-1 test	102
Figure V. 1. A picture of ERC-I test	109

Figure V. 2. A picture of ERC-II test	109
Figure V. 3. Mesh for ERC-I test	110
Figure V. 4. Mesh for ERC-II test	110
Figure V. 5. Typical experimental force/displacement curve of ERC-I test	111
Figure V. 6. Evolution along the crack front of G_I , G_{II} , G_{III} normalized by G_T in ERC-I test	112
Figure V. 7. Evolution along the crack front of G_I normalized by G_{I-av} in ERC-I test.....	112
Figure V. 8. Typical experimental force/displacement curve of ERC-II test.....	113
Figure V. 9. Evolution along the crack front of G_I , G_{II} , G_{III} normalized by G_T in ERC-II test	113
Figure V. 10. Evolution along the crack front of G_{II} normalized by G_{II-av} in ERC-II test	114
Figure V. 11. Evolution along the crack front of G_I , G_{II} , G_{III} normalized by G_T in ERC-I+II test	116
Figure V. 12. Evolution along the crack front of G_I , G_{II} , G_{III} normalized by G_T in ERC-I+III test.....	117
Figure V. 13. Evolution along the crack front of G_I , G_{II} , G_{III} normalized by G_T in ERC-I+II+III test.....	118

List of Tables

Table. 1. Mechanic properties of the tested laminates	13
Table. 2. Comparison of the main pure mode III tests	38
Table. 3. Dimensions of the unidirectional specimens	48
Table. 4. Mechanical properties of the tested laminates.....	49
Table. 5. Mechanic properties of steel devices.....	50
Table. 6. Mechanic properties of steel devices.....	50
Table. 7. Mechanic properties of bondline	50
Table. 8. Dimension of DCB specimens	53
Table. 9. Dimensions of ENF specimens	55
Table. 10. Results of G_{IC} from different methods for DCB test.....	58
Table. 11. Results of G_{IIC} from different methods	60
Table. 12. Toughness of pure mode I, pure mode II	61
Table. 13. Dimensions of ECT-1 specimen.....	63
Table. 14. G_{IIIC} measured by ECT-1 tests	65
Table. 15. Dimensions of ECT-2 specimens	69
Table. 16. Parameters of cohesive element material model	77
Table. 17. G_{IIIC} obtained from Tada's formula for ERCT tests.....	81
Table. 18. G_{IIIC} obtained from Tada's formula for MERCT tests	103
Table. 19. Comparison of G_{IIIC} obtained from different methods	104
Table. 20. Toughness of pure mode I, pure mode II and pure mode III.....	107

CHAPTER I. INTRODUCTION

I.1. Motivation

High performance laminated composites are widely used in aerospace industry where mass reduction is a main concern. The laminated composites have interesting mechanical properties such as their high specific strength and specific stiffness. They have good behavior under fatigue, impact loading and corrosion. In addition a structure in laminated composite can be optimized according to their mechanical loads in service, thus allow a considerable flexibility of design. On the contrary, the damage modes are quite complex and deserve special attention. The heterogeneity and anisotropy introduce difficulties of calculation, and manufacturing processes introduces defects. Especially the laminated composite structures are usually in the form of plates and shells, but the low strength of fracture between the layers presents an essential weakness. This kind of interlaminar fracture, named delamination, is one of the most dangerous damage modes. Herein, the interlaminar stresses are the key parameters; they cannot be determined by classic plaque or shell theory usually applied for calculating the laminates.

Fracture mechanics is preferred to study delamination in modern materials science because the loading field at the crack tip is singular. In fracture mechanics, three basic modes of fractures are defined: mode I (opening), mode II (in-plane shear) and mode III (out-of-plane shear). Generally, delamination in a laminated composite structure in service propagates in mixed mode I+II+III, whose prediction needs a general criterion including the participation of mode I, mode II and mode III. In literature, pure mode I and pure mode II delamination are well characterized. Then, mixed mode I+II criteria have been proposed thanks to the achievements of pure mode I, II and mixed mode I+II delamination tests. On the contrary, work regarding the participation of mode III remains a complex issue because even the pure mode III tests are very difficult to achieve. As a result, in this work we focus on characterizing the pure mode III delamination toughness, and then mixed mode delamination testing method with participation of mode III will be discussed.

I.2. Objectives and scopes

The aim of this research work is to develop testing methods for characterizing the delamination behavior of laminate composite materials under the three pure modes and mixed modes, focusing especially on the complex issue of mode III. Both experimental and numerical works were performed, validating the existing and new testing methods. Correlation between the results obtained aims, on one hand to a better understanding of the distribution of strain energy release rates (G_I , G_{II} , G_{III}) along the crack front and on the other hand, to propose and improve testing methods, and also to propose and validate simple approaches for the determination of delamination toughness.

Firstly, some testing methods proposed and largely used in the literature have been studied experimentally and numerically, including Double Cantilever Beam (DCB) for pure mode I;

End Notched Flexure (ENF) for pure mode II; Edge Crack Torsion using tensile machine (ECT-1) and Edge Crack Torsion using torsion machine(ECT-2) for pure mode III. Secondly, novel testing methods named Edge Ring Crack Torsion (ERCT or ERC-III) tests, have been developed in order to obtain pure mode III loading condition, as well as a more uniform distribution of mode III component along the crack front. Thirdly, original testing methods for pure mode I and pure mode II delamination are proposed using the Edge Ring Crack specimens. The toughness measured by ERC tests were compared to the ones obtained by the testing methods proposed in literature, the advantages and disadvantages of ERC tests were also discussed. Finally, mixed mode I+II, mixed mode I+III and mixed mode I+II+III delamination are expected to be achieved with the Edge Ring Crack specimens. All the work above is fundamental for the establishment of a general criterion to characterize mixed mode resistance to delamination propagation in a laminated composite structure.

The scopes of the study cover:

(1) Materials:

In this research work, all tests were obtained from a woven carbon/epoxy taffeta fabric prepreg (ref: IMP503Z), whose properties are listed in Table. 1. The values with "*" mean the measured values, which will be presented in the preliminary study in chapter III, whereas the other parameters were obtained from reference or in literature.

Fabric weight	200 (g/m ²)
Glass transition temperature: T_g	120 (°C)
Percentage of matrix: V_m	42%
Longitudinal and transverse modulus : $E_{11}=E_{22}$	55250 (MPa)*
Young's modulus in thickness: E_{33}	7100 (MPa)
Out-of-plane shear modulus: $G_{13}=G_{23}$	5400(MPa)
656Tensile strength in direction 1 and 2: $X^+ = Y^+$	669 (MPa)*
Poisson's ratio 12: ν_{12}	0.044*
Poisson's ratio 13: ν_{13}	0.0858
Poisson's ratio 23: ν_{13}	0.0858
Shear modulus in direction 12: G_{12}	4062 (MPa)*
Shear strength in direction 12: S_{12}	117 (MPa)*
Transverse compressive strength	360 MPa

Table. 1. Mechanic properties of the tested laminates

A 13 μm thick polyester film was inserted in the laminate in order to create a pre-crack, which is a classical method to create a pre-crack. In fact, there is a rich zone of resin at the crack tip, which is different from the real crack. Cyanoacrylate glue and Araldite 2012 were used to paste specimens on some devices used in our experiments.

(2) Stacking sequence

The polyester film separates the laminate into two sub-laminates. The stacking sequence of each sub-laminate was optimized in order to obtain special material parameters according to the study of VANNUCCI and GONG^[1;2]. Note that 0 represents a taffeta balanced fabric ply with yarns oriented in 0° and 90° while 45 represents $\pm 45^\circ$.

To meet the geometry requirements, the stacking sequence for Double Cantilever Beam (DCB), End Notched Flexure (ENF) and Edge Crack Torsion (ECT-1) (using tensile machine) tests is designed as:
 (45/0/0/45/0/45/45/0)//crack//(0/45/45/0/45/0/0/45)

The stacking sequence for tests Edge Crack Torsion (ECT-2) test (using torsional machine) and Edge Ring Crack (ERC) tests is designed as:
 (0/45/45/0/45/0/0/45/45/0/0/45/0/45/45/0)//crack//(0/45/45/0/45/0/0/45/45/0/0/45/0/45/45/0)

These laminates are quasi-homogeneous, i.e. the same elastic stiffness properties in tension and in bending; and they are also quasi-isotropic, i.e. the same elastic stiffness properties in tension and in bending in all direction; the elimination of all possible coupling terms: $B_{ij}=A_{16}=A_{26}=D_{16}=D_{26}=0$, as shown in Figure I. 1 and Figure I. 2.

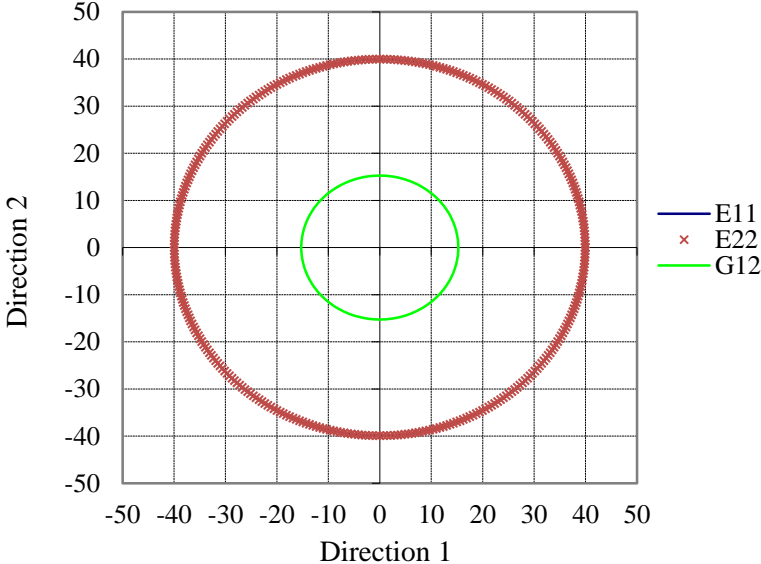


Figure I. 1. Young's modulus and shear modulus (GPa) for the laminate in membrane

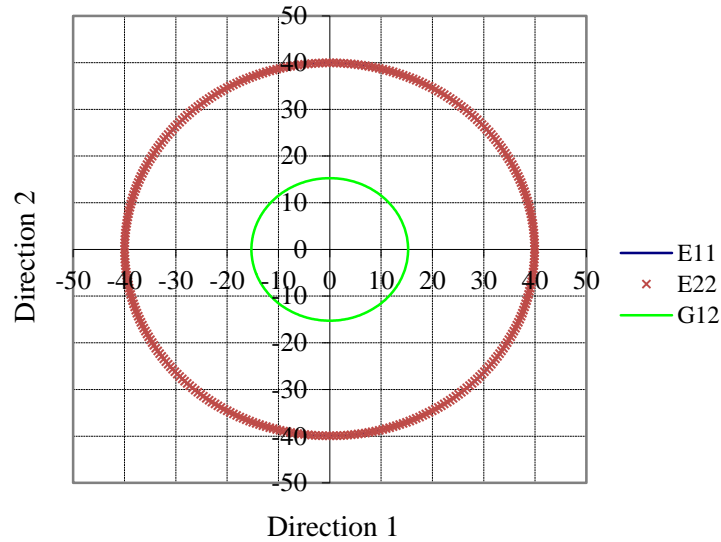


Figure I. 2. Young's modulus and shear modulus (GPa) for the laminate in flexion

The stacking sequence for ERC-I+II and ERC-I+II+III tests is designed as:
 (0/45/45/0/45/0/0/45/0/0/45/0/45/45/0)//crack//(0/45/45/0)

Note that the Poisson's ratios for the two sub-laminates are different.

For all of the stacking sequence of laminates used in this study, the fiber orientation of the adjacent 4 plies close to the crack plane is the same. The design aims at avoiding the interference caused by different fiber orientations in adjacent plies next to the crack plane when different tests are compared. In the traditional pure mode delamination tests, delamination propagates between two plies with the fiber orientation 0/0.

(3) Testing parameters and variables:

All the tests were realized at ambient temperature. Static loading was applied for all the tests using tensile/compression machine For DCB, ENF, ECT-1 ERC-I and ERC-II tests, the loading speed is 2mm/min; for ECT-2 and ERC-III tests, a torsion machine is needed and the loading speed is 0.5 %/min.

(4) Finite element analysis was performed on all the tests in this study using the simulation software package LS-dyna.

I.3. Organization of thesis

This thesis is divided in 6 chapters as follows:

Chapter I mainly expresses the motivations, objectives and scopes of the work.

Chapter II gives a general literature review of all kinds of physical damages in laminated composites, especially the delamination in a laminated composite. Then the majority of criteria to characterize the damages are summarized. Delamination and criterion based on fracture mechanics are introduced particularly. Different kinds of testing methods to study

delamination with the participation of mode III are discussed and compared. At last, finite element methods to evaluate strain energy release rate are summarized.

Chapter III presents the preliminary study on the tested laminated composite. Firstly the mechanical characterization results of the composites are provided. And then the traditional tests of delamination including DCB pure mode I and ENF pure mode II have been performed and simulated.

Chapter VI focuses on the characterization of pure mode III delamination behavior of a laminated composite. At the beginning two kinds of Edge Crack Torsion tests, proposed in the literature, were carried out. The distribution of G_{III} along the crack front was determined by finite element analysis (FEA) using virtual crack closure technique (VCCT). The performances of these tests are discussed. And then a novel mode III testing method was developed, named Edge Ring Crack Torsion test (ERCT or ERC-III later). A closed-form solution proposed by Tada is applied to determine mode III delamination toughness. Actually, a numerical study on the factors affecting the distribution of G_{III} was carried out in this study. In order to understand the influence of potential defaults on the performance of ERCT test, sensitivity study was performed on the relative position of the crack front, the circularity of the crack front and the specimen shape. Optimum specimen's relative pre-crack geometry is given and a method for reducing the variation of the G_{III} along the crack front is provided.

Chapter V presents the studies of the extension of the use of Edge Ring Crack (ERC) specimens from pure mode III to pure mode I (named ERC-TE or ERC-I), pure mode II (named ERC-F or ERC-II) and mixed mode delamination testing. For the testing under pure mode I and pure mode II, both of experiments and FEA are carried out. Tests of delamination under mixed mode I+II, mode I+III and mixed mode I+II+III are only investigated numerically.

The thesis is concluded by Chapter VI, which gives general conclusions of this study and some recommended future work.

CHAPTER II. LITTERATURE REVIEW

II.1. Introduction

In this chapter, a general literature review is given in order to expose the background of this work. Firstly, mechanisms of damage and fracture of laminated composite are introduced, especially delamination. Secondly, most existing fracture criterions are introduced. Thirdly, mode III delamination testing methods existing in literature are discussed. Finally, finite element methods available in literature in order to calculate strain energy release rates are studied.

II.2. Mechanisms of damage and fracture of laminated composite

In the book *Composite Materials: Mechanical Behavior and Structural Analysis* ^[3], laminated composite is defined: “laminates are made of successive layers of reinforcements impregnated with resins” and mechanisms of damage and fracture of laminated composite are introduced. Here we give a brief presentation.

II.2.1. The principal mechanisms of damage in a single ply

The fracture process of a laminated composite consists of three stages: initiation of damage, the propagation of the damaged area and the final fracture. The principal mechanisms of damage in a composite laminate are summarized as follows:

(1) The fibers fracture

In a composite material subjected to mechanical loads, fiber fracture occurs when the tensile stress σ_f in a fiber reaches the fracture stress σ_{fu} (Figure II. 1). The fiber fracture then leads to a stress concentration around the fracture. Redistribution of these constraints mainly depends on the tensile strength σ_{fu} of fibers, the ability of the matrix to absorb the energy released, the properties of the fiber-matrix interface, etc. Figure II. 2 shows the various fracture modes of the matrix associated with the fracture of a fiber.

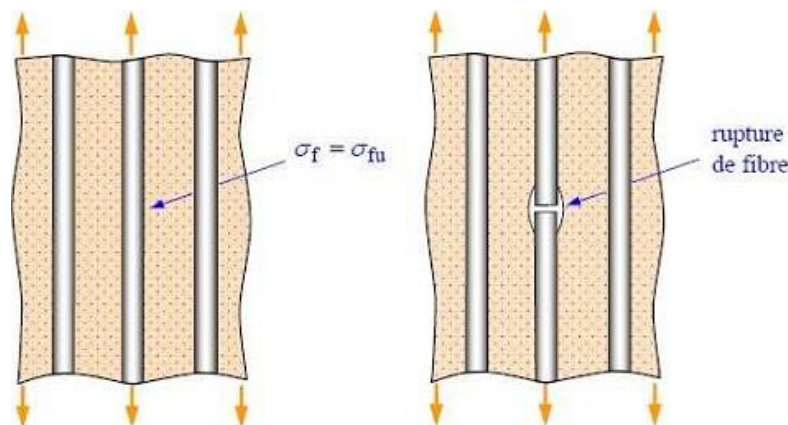


Figure II. 1. Longitudinal traction: fiber fracture ^[3]

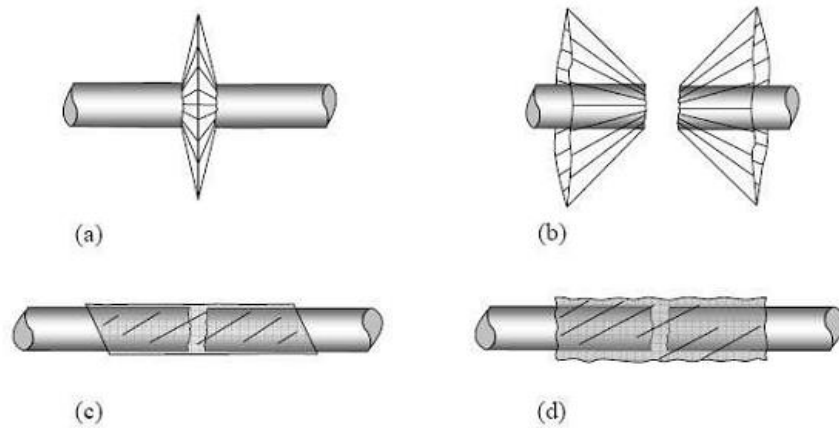


Figure II. 2. (a) Transverse fracture of matrix (b) shear fracture of matrix (c) debonding of the fiber-matrix interface (d) longitudinal fracture of the matrix^[3]

(2) Local buckling of the fibers

The local buckling of fibers may occur if loading is in compression around the partially loosened fibers. (Figure II. 3)

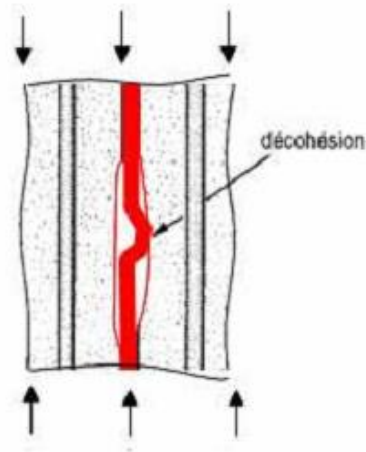


Figure II. 3. Local buckling of a fiber

(3) Plastic strain of the matrix

The plastic deformation of the matrix happens if the matrix is a ductile material and the level of applied stress exceeds the elastic limit.

(4) Transverse fracture of the matrix

The transverse cracking of matrix (Figure II. 4) can occur when the stress in traction σ_m reaches the fracture stress of the matrix σ_{mu} .

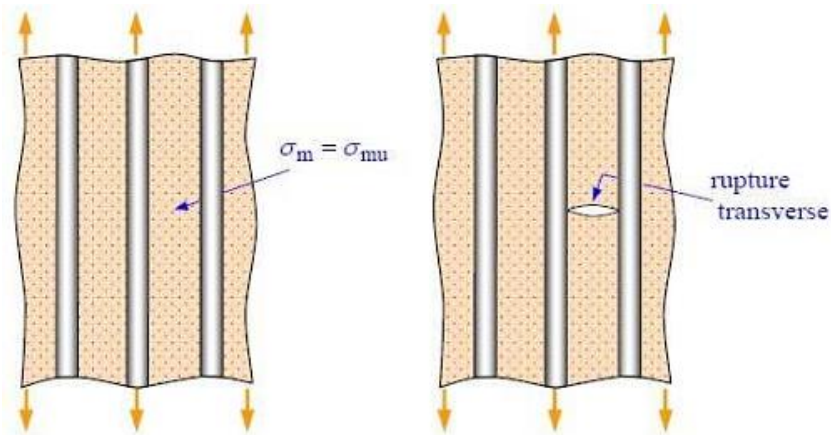


Figure II. 4. Longitudinal traction: transverse fracture of the matrix^[3]

(5) Longitudinal fracture of the matrix

The longitudinal cracking of the matrix (Figure II. 5) can occur when the shear stress τ_m in the matrix reaches the shear stress fracture of the matrix τ_{mu} , generally near a fiber.

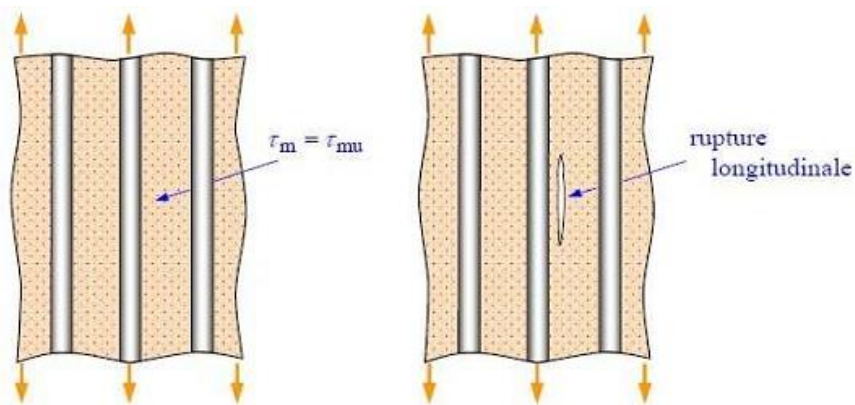


Figure II. 5. Longitudinal traction: longitudinal fracture of the matrix^[3]

(6) Fracture of the fiber-matrix interface

The fracture of the fiber-matrix interface occurs when the debonding stress is below the shear stress of the matrix fracture $\tau_d < \tau_{mu}$ (Figure II. 6)

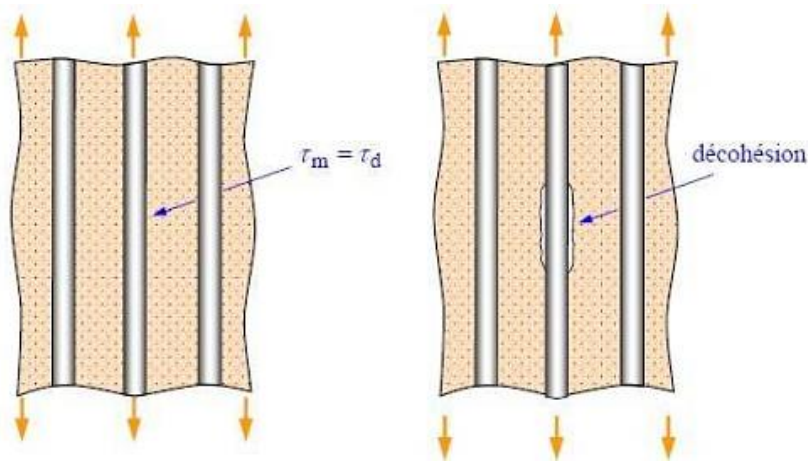


Figure II. 6. Longitudinal traction: fracture of the fiber-matrix interface ^[3]

(7) The mixture of mechanisms of damage

In the case of a unidirectional composite subjected to a longitudinal traction, the initiation of the fracture is generally produced either by the fracture of the fibers or by transverse fracture in the matrix. After initiation, propagation of the fracture differs according to the nature of the fiber-matrix interface.

In the case of a high fiber-matrix adhesion, the fracture is initiated, either by the fracture of the fibers or by fracture of the matrix. Figure II. 7 shows the coupling between a longitudinal fracture of the matrix and fiber-matrix debonding.

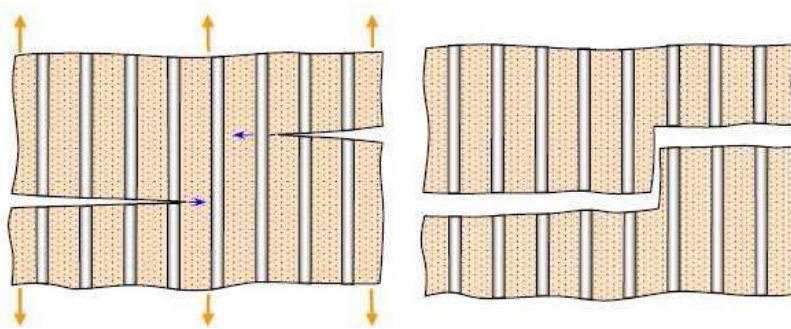


Figure II. 7. Crack growth in the case of strong adhesion fiber-matrix ^[3]

In the case of a weak fiber-matrix adhesion, the transverse crack propagation can be schematized as Figure II. 8.

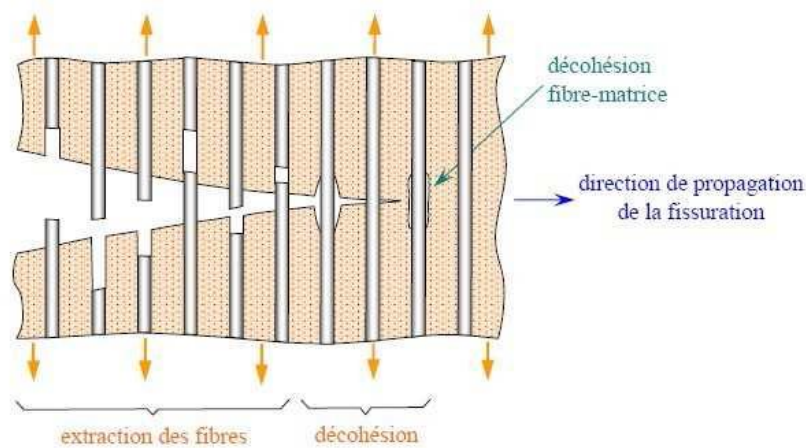


Figure II. 8. Crack growth in the case of weak adhesion fiber-matrix^[3]

In the case of a unidirectional composite subject to transverse traction, the fracture occurs either by fracture of the matrix or by debonding of the fiber-matrix interface. The fracture of the matrix occurs when σ_m reaches σ_{mu} . This process occurs when σ_{mu} is below the debonding stress in traction of the fiber-matrix interface σ_d . Otherwise, the fracture of the composite occurs through the fracture of the fiber-matrix interface (Figure II. 9)

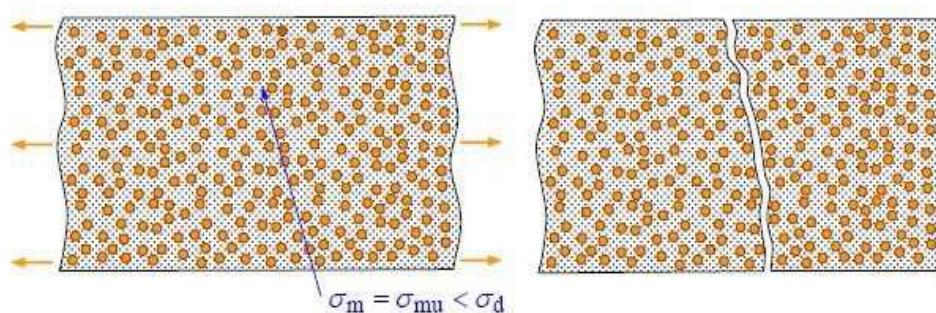


Figure II. 9. Fracture of a unidirectional composite under transverse traction^[3]

II.2.2. Delamination

The damages of multidirectional laminated composites can be very complex. Among all kinds of damages, delamination is one of the most dangerous and common modes. It is the interlaminar fracture between two sub-laminates and the fracture plane is always tangential to the reinforcements, shown in Figure II. 10. In fact, delamination in a laminated composite is a particular type of fracture by its position and its physical mechanisms.

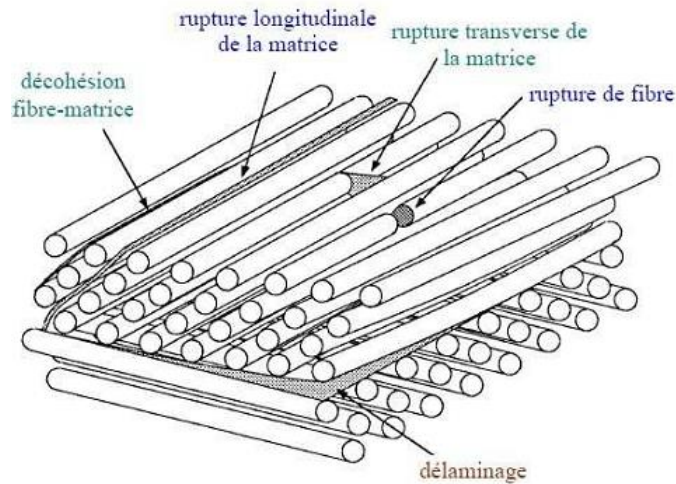


Figure II. 10. Mechanism of fracture observed in a laminate composite

Fracture mechanics is usually applied to describe delamination because of the singularity at the crack front, in which we define three basic modes: mode I (opening), mode II (in-plane shear) and mode III (out-of-plane shear), shown in Figure II. 11. The delamination resistance of a composite can be characterized firstly by three intrinsic material constants: G_{IC} , G_{IIC} and G_{IIIC} which are the critical strain energy release rate in the 3 pure modes; secondly by R-curve which shows the variation of the resistance to the crack propagation as a function of the crack extension.

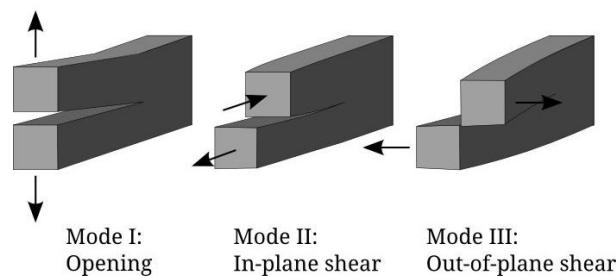


Figure II. 11. Three basic fracture modes

G_C can be determined using the Irwin-Kies equation ^[4]:

$$G_C = \frac{P_C^2}{2B} \frac{dC}{da} \quad \text{Eq. 1}$$

, where P_C is the critical load corresponding to crack onset; B is the width of the crack; C is the compliance and a = the initial crack length. If the specimen maintains a constant fracture mode during crack propagation, C can be calibrated as a function of a . First of all, it can be calculated analytically with certain assumption and simplification. In most cases, compliance calibration method (CC) can be realized both empirically and numerically. Empirically, experimental tests with specimens of different initial crack length are carried out aiming at evaluating the slope of the linear part from the load-displacement curve and the inverse of the slope gives the compliance for each specimen with different initial crack length. Then, the values of the compliance are interpolated as a function of the crack length a . Numerically, the evolution of C according to a can also come from simulation results and then the same interpolation method can be used.

The steps are as below:

- (1) Make a series of test specimens of the same geometry except for different initial crack length;
- (2) Measure the compliance of each specimen: $C_i = \delta_i / P_i$ (Displacement/load) on the linear domain (shown in Figure II. 12(a));
- (3) Interpolate these measured C_n as a function of the crack length to determine the compliance law: $C = f(a)$ (shown in Figure II. 12(b));
- (4) Determine strain energy release rate by the Irwin-Kies' formula. When P reaches P_C the critical loading, then G equals G_C .

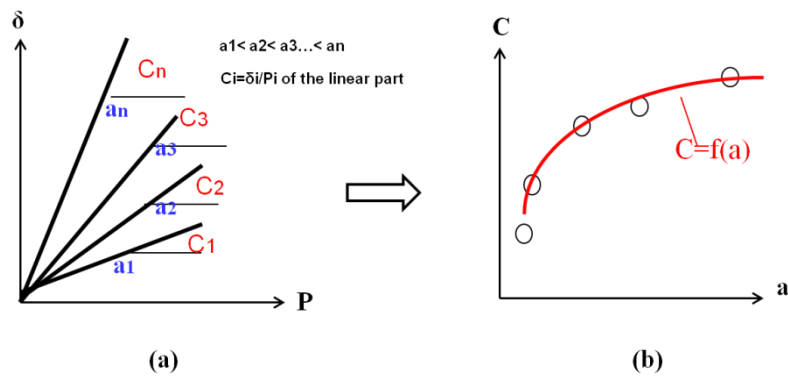


Figure II. 12. Experimental compliance calibration

II.2. Fracture criteria

A large number of fracture criteria have been established in order to characterize the damage and fracture in a laminated composite. Classical mechanics and fracture mechanics are applied in order to model different kinds of damages in a laminated composite. Fracture mechanics is preferred to characterize delamination behavior due to the singularity of stress at crack tip. The criteria can be classified as criteria without stress interaction, interactive criteria and semi-interactive criteria.

II.2.1. Criteria without stress interaction

The criteria without stress interaction are the basic criteria and contain the criteria of the maximum stress and the criteria of the maximum strain. They are very simple to apply, but they do not allow accounting the combination of experimental results. Criteria of the maximum stress and criteria of the maximum strain belong to this kind of criteria.

II.2.2. Interactive criteria

The criteria of the maximum stress and maximum strain exclude the existence of interactions between stress and strain in the axes of materials: mechanisms in longitudinal, transverse or shear fracture are supposed to occur independently. Interactive criteria were then developed by extending to orthotropic materials, Von Mises criterion. Von Mises criterion is connected to the strain energy stored per unit volume of the deformed material. However, these criteria

are no longer connected exclusively to the deformation energy in the case of orthotropic materials.

One of the first interactive fracture criteria applied to anisotropic materials was introduced by R. Hill^[5]. It should be noted that the criterion of Hill does not take into account the difference of the behavior of materials in tension and compression, so it is suitable for composites having a very close tensile and compression strength. Moreover, this criterion does not give information on fracture modes.

The previous fracture criterion for in plane stress has been simplified by V. D. AZZI et S. W. Tsai^[6] in the case of unidirectional composites.

A generalization of the Hill's criterion was formulated by O. Hoffman^[7]. Hoffman's criterion takes into account the different behavior of the material in traction and compression.

The previous criteria are usually sufficient to describe the various experimental results. One way to improve the correlation between experimental and theoretical results is to increase the number of parameters of the theoretical equations. S. W Tsai and E. M. Wu^[8] gave a fracture criterion who allows more parameters to correlate with experimental results.

II.2.3. Semi-interactive criteria

Although the criteria discussed in the previous part take into account interaction between the applied stresses, they do not allow relating the rupture with the damage mechanisms. The semi-interactive criteria developed more recently, allow giving material properties to all identified damage mechanisms.

(1) Hashin's Criterion

The test proposed by Hashin^[9] clearly associates the responsible stress with a well defined damage mode, which can take into account the influence of damage identified in the calculation of the structure. This criterion is expressed in four inequalities:

Fracture of fibers in traction:

$$\left(\frac{\sigma_{11}}{X^+}\right)^2 + \left(\frac{\tau_{12}}{S}\right)^2 \leq 1 \quad \text{Eq. 2}$$

Fracture of fibers in compression:

$$\left(\frac{\sigma_{11}}{X^-}\right)^2 \leq 1 \quad \text{Eq. 3}$$

Fracture of matrix in traction:

$$\left(\frac{\sigma_{22}}{Y^+}\right)^2 + \left(\frac{\tau_{12}}{S}\right)^2 \leq 1 \quad \text{Eq. 4}$$

Fracture of matrix in compression:

$$\left(\frac{\sigma_{22}}{2S}\right)^2 + \left(\frac{\tau_{12}}{S}\right)^2 + \left[\left(\frac{Y^-}{2S}\right) - 1\right] \frac{\sigma_{22}}{Y^-} \leq 1 \quad \text{Eq. 5}$$

(2) Chang-Chang Criterion

The Chang-Chang criterion ^[10] modifies the Hashin's criterion integrating the nonlinear behavior in shear, frequently observed for composites:

$$\nu_{12} = \left(\frac{1}{G_{12}}\right)\tau_{12} + \alpha\tau_{12}^3 \quad \text{Eq. 6}$$

where α comes from the non-linear shear equation

The expression of this criterion can be summarized in:

Fracture of fibers in traction:

$$\left(\frac{\sigma_{11}}{X^+}\right)^2 + \frac{\frac{\tau_{12}^2}{2G_{12}} + \frac{3}{4}\alpha\tau_{12}^4}{\frac{S_{12}^2}{2G_{12}} + \frac{3}{4}\alpha S_{12}^4} \leq 1 \quad \text{Eq. 7}$$

Fracture of fibers in compression:

$$\left(\frac{\sigma_{11}}{X^-}\right)^2 \leq 1 \quad \text{Eq. 8}$$

Fracture of matrix in traction:

$$\left(\frac{\sigma_{22}}{Y^+}\right)^2 + \frac{\frac{\tau_{12}^2}{2G_{12}} + \frac{3}{4}\alpha\tau_{12}^4}{\frac{S_{12}^2}{2G_{12}} + \frac{3}{4}\alpha S_{12}^4} \leq 1 \quad \text{Eq. 9}$$

Fracture of matrix in compression:

$$\left(\frac{\sigma_{22}}{Y^-}\right)^2 + \frac{\frac{\tau_{12}^2}{2G_{12}} + \frac{3}{4}\alpha\tau_{12}^4}{\frac{S_{12}^2}{2G_{12}} + \frac{3}{4}\alpha S_{12}^4} \leq 1 \quad \text{Eq. 10}$$

The criteria in the third category are widely implemented in finite element software.

Longitudinal traction:

$$\left(\frac{\sigma_{11}}{X^+}\right)^2 + \left(\frac{\sigma_{12}}{S_{12}}\right)^2 + \left(\frac{\sigma_{13}}{S_{13}}\right)^2 \leq 1 \quad \text{Eq. 11}$$

Transverse traction:

$$\left(\frac{\sigma_{22}}{Y^+}\right)^2 + \left(\frac{\sigma_{12}}{S_{12}}\right)^2 + \left(\frac{\sigma_{23}}{S_{23}}\right)^2 \leq 1 \quad \text{Eq. 12}$$

In plane shear:

$$\left(\frac{\sigma_{11}}{X^+}\right)^2 + \left(\frac{\sigma_{13}}{S_{13}}\right)^2 \leq 1 \quad \text{Eq. 13}$$

Out of plane shear:

$$\left(\frac{\sigma_{22}}{Y^+}\right)^2 + \left(\frac{\sigma_{23}}{S_{23}}\right)^2 \leq 1 \quad \text{Eq. 14}$$

Longitudinal compression:

$$\left(\frac{\sigma_{11}}{X^+}\right)^2 \leq 1 \quad \text{Eq. 15}$$

Transverse compression:

$$\left(\frac{\sigma_{22}}{S_{12}+S_{23}}\right)^2 + \frac{\sigma_{22}Y^-}{(S_{12}+S_{23})Y^- - 1} + \left(\frac{\sigma_{12}}{S_{12}}\right)^2 + \left(\frac{\sigma_{23}}{S_{23}}\right)^2 \leq 1 \quad \text{Eq. 16}$$

Out of plane compression:

$$\left(\frac{\sigma_{33}}{S_{13}+S_{23}}\right)^2 + \frac{\sigma_{33}Z^-}{(S_{13}+S_{23})Z^- - 1} + \left(\frac{\sigma_{13}}{S_{13}}\right)^2 + \left(\frac{\sigma_{23}}{S_{23}}\right)^2 \leq 1 \quad \text{Eq. 17}$$

Delamination:

$$\left(\frac{\sigma_{33}}{Z^+}\right)^2 + \left(\frac{\sigma_{23}}{S_{23}}\right)^2 + \left(\frac{\sigma_{13}}{S_{13}}\right)^2 \leq 1 \quad \text{Eq. 18}$$

Where σ_{11} , σ_{22} , σ_{33} are the normal stress along the three orthotropic axis of elemental layer. The corresponding strength are named X^+ , Y^+ , Z^+ in traction and X , Y , Z in compression, respectively. The shear stresses in the plane 12, 23 and 13 are denoted σ_{12} , σ_{23} , σ_{13} . Their associated strengths are defined by S_{12} , S_{23} , S_{13} .

It is interesting to note that if the base material is considered as a transverse isotropic where $Y_i=Z_i$ and $S_{12}=S_{13}$, as in the majority of cases for unidirectional composite, the material behavior in the delamination presented by Eq. 18 returns to the one of delamination(Eq. 12). This situation is not at all realistic in a multidirectional laminated composite.

II.2.4. Mixed mode delamination criteria

(1) Semi-empirical criterion in mixed mode I+II

Theoretically, the fracture criterion under mixed mode I+II could be in a polynomial form K_I et $(K_{II})^2$. However, the form of the criterion proposed in the literature is often in a power form:

$$\left(\frac{K_I}{K_{IC}}\right)^n + \left(\frac{K_{II}}{K_{IIC}}\right)^{2m} = 1 \quad \text{Eq. 19}$$

$$\left(\frac{G_I}{G_{IC}}\right)^{\frac{n}{2}} + \left(\frac{G_{II}}{G_{IIC}}\right)^m = 1 \quad \text{Eq. 20}$$

where K_i and G_i respectively correspond to the stress intensity factors and strain energy release rate in mode i .

In the works of Gong ^[11, 12], an unexpected observation was raised by the analysis of a composite toughness measured on Glass-Epoxy: participation of mode I delamination under mixed mode I + II may be greater than tenacity under pure mode I. The ratio G_I/G_{IC} can reach 2.5 for the tested composite. This phenomenon was also observed by other authors in fragile matrix composites. In this case, the criteria given in the form of Eq. 19 and Eq. 20 are no longer valid whatever the values of the exponents m and n are.

A polynomial criterion was proposed by focusing on the participation of mode II: $G_{TC}=k_1+k_2G_{II}^\beta$, where β is a constant determined empirically. The exact value of β can be easily determined by the interpolation of the experimental results. One can get the following expression applying the extreme cases under pure mode I and pure mode II:

$$G_{TC} = G_{IC} + (G_{IIC} - G_{IC}) \left(\frac{G_{II}}{G_{IIC}} \right)^\beta \quad \text{Eq. 21}$$

This criterion has also been applied to the results published in the literature. By choosing the constant β , all the results we used are perfectly represented by this criterion. Some fronts were given by the authors:

β is a constant of the material, which depends mainly on the quality of the matrix and the fiber / matrix interface;

β appears to be independent of the absorbed moisture even if G_{IC} and G_{IIC} are highly dependent on it;

β is not sensitive to the orientation of adjacent plies of fiber although G_{IC} and G_{IIC} are dependent heavily;

β is between 2/3 and 1 for a brittle epoxy matrix composite.

(2) Empirical criterion in mixed mode I+II

Despite excellent correlations between the criterion of Eq. 21 and the experimental results, it is neither reassuring participation of mode I, nor the modal report involved in this criterion. In the same studies ^[12,13], an empirical criterion has also been proposed in which the variable is the modal ratio in terms of G_{II}/G_T with $G_T=G_I+G_{II}$

$$G_{TC} = G_{IC} + (G_{IIC} - G_{IC}) \left(\frac{G_{II}}{G_I + G_{II}} \right)^k \quad \text{Eq. 22}$$

, where the constant k must be determined empirically.

This test has been very successful and is currently implemented in much FEM software, as the criterion (B-K) ^[13], to simulate delamination behavior ^[13] in laminates or that of a glued or welded joint.

(3) Predict of the delamination criteria under mixed mode I+ II+III

In the work REEDER JR (2006) ^[14], a new framework for visualizing 3D fracture criteria is studied and new criteria are based on the following assumptions: the relationship between toughness in mode I and mode III is similar to the relationship between toughness under mode I and mode II and linear interpolation can be used between mode II and mode III. According to his study, 3D fracture criteria cannot be evaluated properly until that the data in mixed mode with a mode III component are possible to be obtained, but these assumptions appear reasonable.

This criterion is an extension of B-K criterion, which is an empirical criterion that works well with 2D data. ECT test provides mode III toughness which is generally higher than the mode II toughness. As there are no data available to describe the interactions between mode II and mode III, a reasonable assumption is that a linear interpolation governs the interaction. Combining these assumptions the proposed fracture criterion becomes Eq. 23:

$$\frac{G_T}{G_{IC} + (G_{IIC} - G_{IC}) \left(\frac{G_{II} + G_{III}}{G_T} \right)^\eta + (G_{IIIC} - G_{IIC}) \frac{G_{III}}{G_{II} + G_{III}} \left(\frac{G_{II} + G_{III}}{G_T} \right)^\eta} \geq 1 \quad \text{Eq. 23}$$

The criterion can be written as shown in Eq. 24 in order to show the symmetry between the mode II and mode III

$$\frac{G_T}{G_{IC} + [(G_{IIC} - G_{IC}) \frac{G_{II}}{G_T} + (G_{IIIC} - G_{IIC}) \frac{G_{III}}{G_T}] \left(\frac{G_{II} + G_{III}}{G_T} \right)^{\eta-1}} \geq 1 \quad \text{Eq. 24}$$

II.3. Delamination tests under pure mode I, II, III and mixed mode I+II+III

II.3.1. Introduction

In literature, pure mode I and pure mode II delamination tests have been well studied and even standardized. A brief introduction about pure mode I and pure mode II testing methods is presented in this section. On the contrary, pure mode III delamination test remains a complex issue. A large number of testing methods have been proposed in order to characterize mode III delamination behavior. The achievements and disadvantages of the testing methods are discussed in detail.

II.3.2. Pure mode I

Double Cantilever Beam (DCB) test ^[15] is the most widely used test in order to study mode I delamination behavior. This is a tensile test applied onto two arms of a symmetrical specimen including a pre-crack, which is normally realized via a non-adhesive thin insert ^[16]. A typical DCB test is shown in Figure II. 13. Beam theory and berry theory ^[17] can be applied in experimental compliance calibration for data reduction.

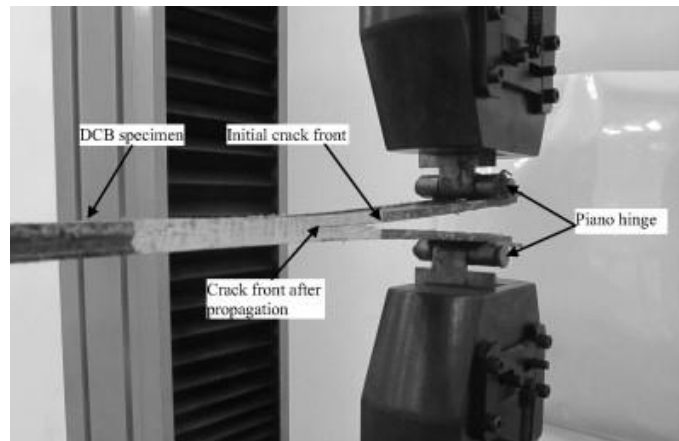


Figure II. 13. Typical set-up for DCB test ^[18]

II.3.3. Pure mode II

End notched flexure (ENF) test ^[19] has been widely used to study mode II delamination behavior. A typical ENF specimen is a three-point bending beam with a mid-plane pre-crack at one end of the beam as shown in Figure II. 14. The simplest analytical expression for the

mode II strain energy release rate, G_{II} , was developed by Russell and Street^[19] and improved using Timoshenko's beam theory by Carlsson et al.^[20].

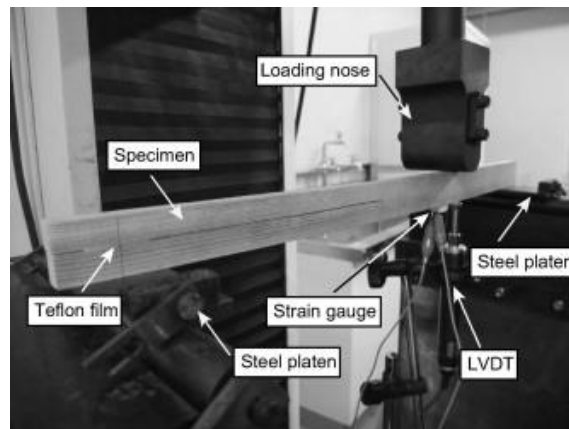


Figure II. 14. Typical set-up for ENF test^[21]

II.3.4. Pure mode III

II.3.4.1. Crack Rail Shear test

The Crack Rail Shear test (CRS)^[22] was proposed by Becht and Gillespie in 1988, shown in Figure II. 15. A plastic film is inserted between two sub-laminates of the specimen to create a precrack. The specimen is screwed to two rails. The configuration was identical to the ASTM standard guide D4255-83 for measuring the in plane shear properties of composite laminates. The initial delaminated portions were cut away from the inner plies after processing in order to accommodate the rail shear fixture. With the rails in place, the specimen is loaded in exactly the same manner as an ordinary two-rail shear test.

The restraint regarding this work is that mode II component at the extremities of the crack front cannot be eliminated. The test produced very low values of compliance, so the compliance calibration method cannot be applied for data reduction. In addition, the two pre-cracks do not propagate simultaneously.

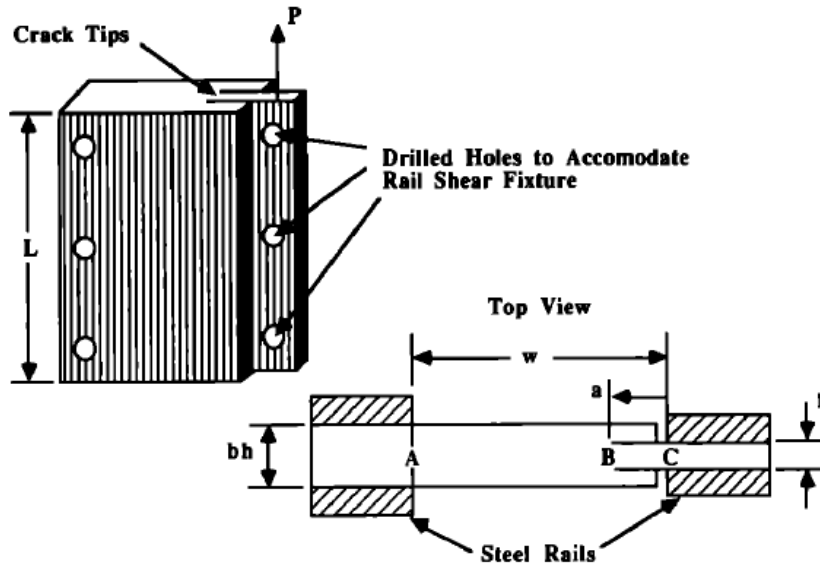
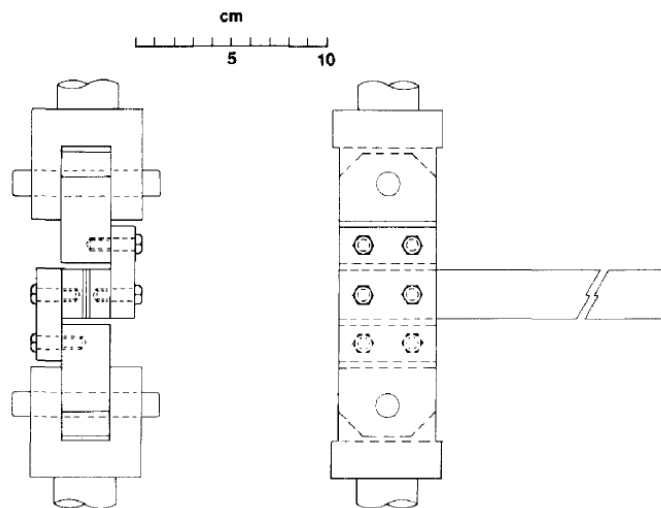


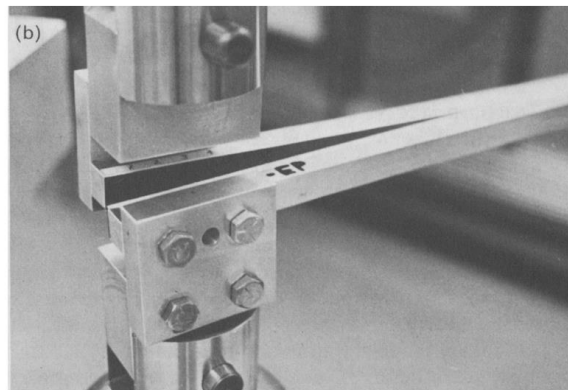
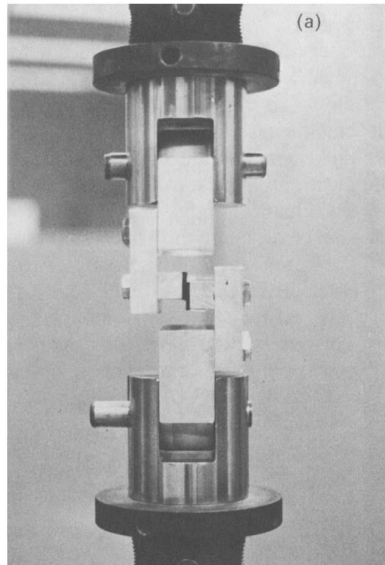
Figure II. 15. Crack Rail Shear specimen geometry^[22]

II.3.4.2. Split Cantilever Beam

Split Cantilever Beam test (SCB)^[23] was proposed by Donaldson in 1988. Each test required bonding a laminate between two aluminum bars, then loading the bars in opposite directions parallel to the crack plane as shown in Figure II. 16. As the crack extends, the aluminum bars act as cantilevers. The main drawback of these tests is the participation of mode I and mode II in the area adjacent to the ends of the crack front^[23,24].



(a) Schematic of split cantilever beam specimen and load fixture



(b) Views of split cantilever beam test in progress

Figure II. 16. Typical split cantilever beam test^[23]

The closed-form expression to determine G_{IIIc} from SCB test is based on the beam theory and classical unidirectional specimens can be used in this test. This configuration has been modified by different authors in order to cancel mode I and mode II and to obtain a more uniform value of G_{III} along the crack front. In general, most modified SCB tests can eliminate mode I component and reduce mode II component. Robinson and Song^[25] tried to limit the bending moment by introducing additional constraints as shown in Figure II. 17, but they concluded that the experimental Compliance Calibration (CC) method cannot be applied in the data reduction schema.

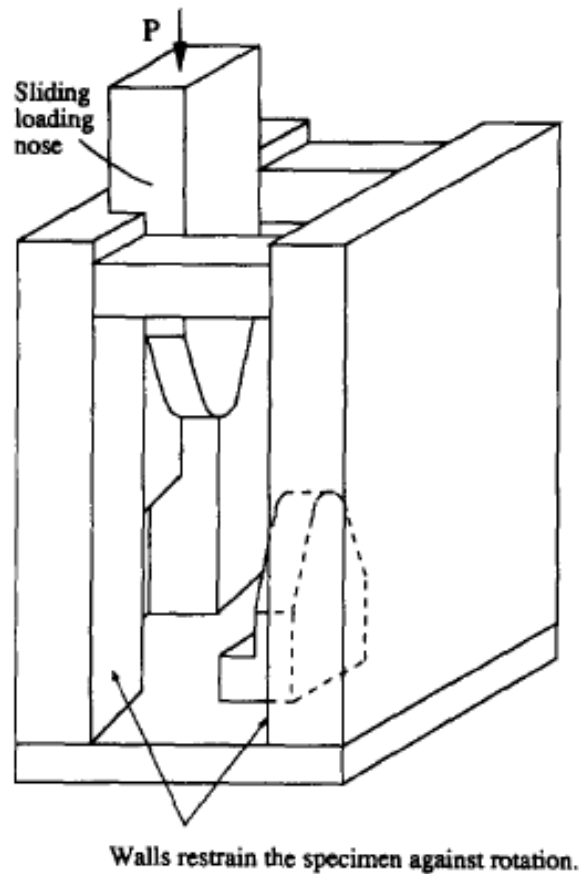


Figure II. 17. test jig used for modified SCB test^[25]

Another modified version of SCB device (MSCB) was then realized by Sharif et al.^[26] and this one is the most widely used SCB device^[27-29], whose specimen was loaded by special grips and the mode II component was significantly reduced according to their work. The data reduction method based on improved beam theory was found to be more reliable than CC method^[30]. However, the measurement of G_{III} is disturbed because the specimen is strongly constrained at its edges near the crack front, so the variation of G_{III} along the crack front becomes more important. As a result, it is not easy to see the crack onset on the load–displacement curve^[27; 28].

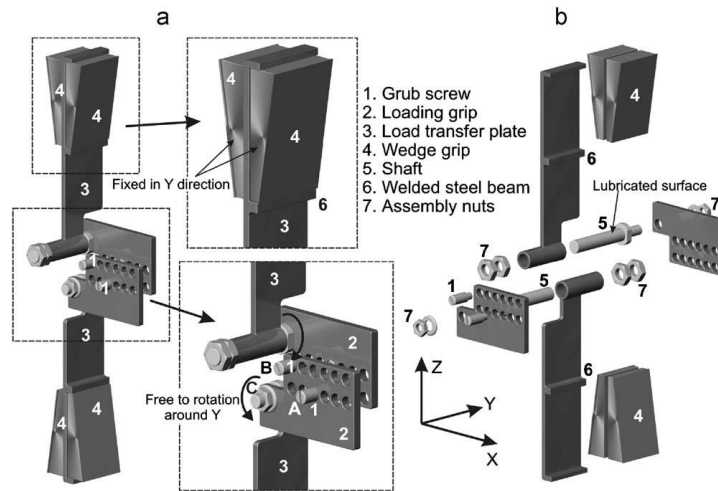


Figure II. 18. 3D view of the experimental equipment. Assembled state (a) and exploded view(b) ^[28]

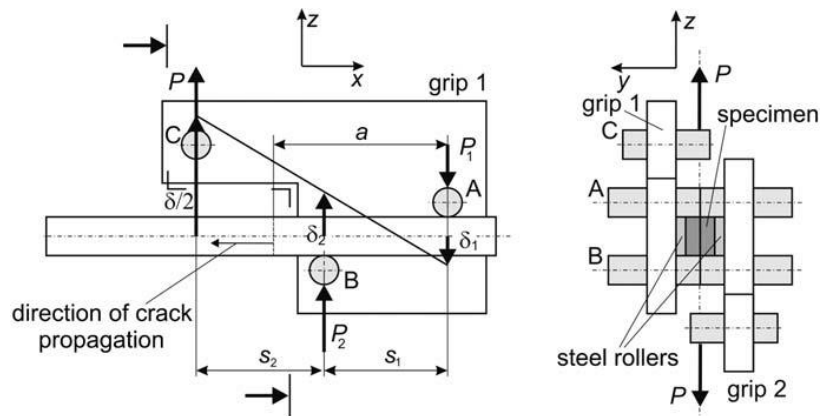


Figure II. 19. Schematic illustration of the MSCB specimen ^[28]

Later, small edge delamination in the MSCB specimen was introduced by Davidson and Sediles ^[31] in order to achieve more uniform evolution of G_{III} along the crack front. The results highlighted the fact that the evolution of G_{III} along the crack front was fairly small. Moreover the delamination onset seemed to correspond to a load drop even though a high level of non-linearity before the critical load was observed. However, the edge initial delamination penetrated a distance into the MSCB specimen from either free edge which was too small (1/16 of the width) to obtain so a number of specimens had to be rejected in their work ^[31].

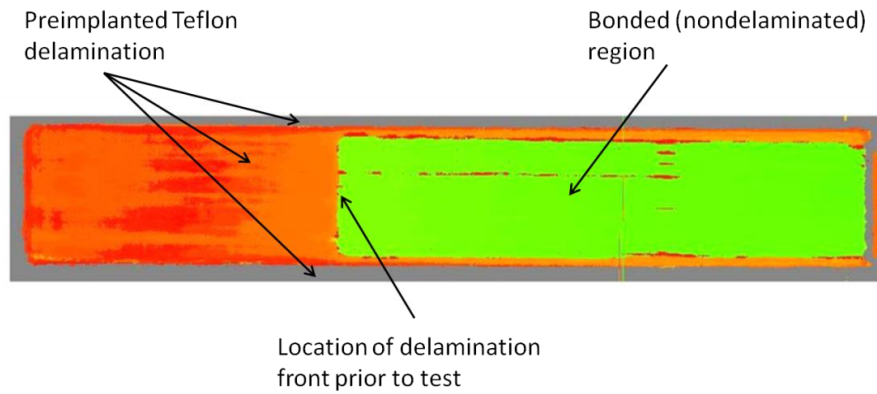


Figure II. 20. Geometry of the MSCB specimen with small edge delamination^[31]

II.3.4.3. Edge Crack Torsion

The Edge Crack Torsion (ECT) test was proposed by Lee^[32]. A tensile machine was used to load the specimen under torsion up to delamination growth from an edge crack. The closed-form expression to determine G_{IIIc} is based on the plate theory. Different from SCB, the specimens have to be multidirectional laminates whose twisting stiffness and strength must be strong enough to guarantee the crack propagation. Actually, the loading conditions in the first ECT tests^[32-37] cannot induce symmetrical distribution of G_{III} along the crack front. This test is called ECT-1 thereafter.

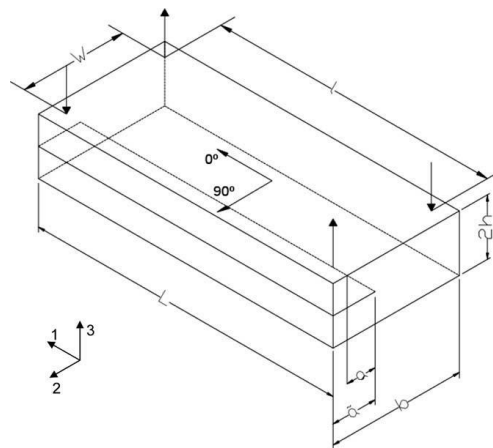


Figure II. 21. Schematic of ECT specimen^[38]

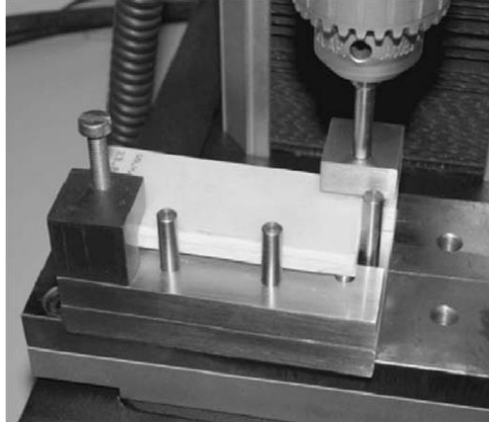


Figure II. 22. ECT-1 specimen and test fixture ^[38]

Recent studies ^[38-43] adopted a configuration with more symmetric loading conditions, named modified Edge Ring Crack Torsion test. This test is called MECT-1 thereafter. This modification allows decreasing the likelihood of geometric nonlinearity and improving the uniformity of G_{III} along the crack front.

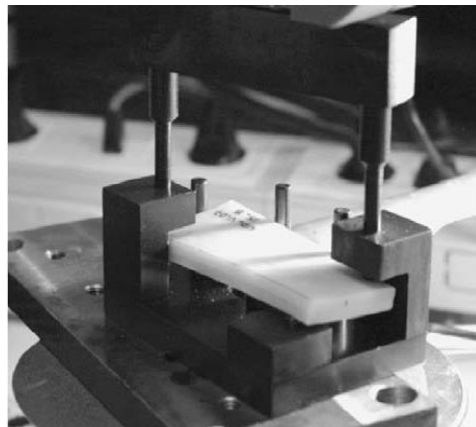


Figure II. 23. MECT-1 specimen and test fixture ^[38]

Another ECT configuration using a torsion machine was proposed by H. Suemasu ^[44] aiming at obtaining uniform distribution of G_{III} along the crack front. Both ends of the specimens in ECT-2 test were loosely fixed so that an axial slide was permitted during the application of the torque. This test is called ECT-2 thereafter.

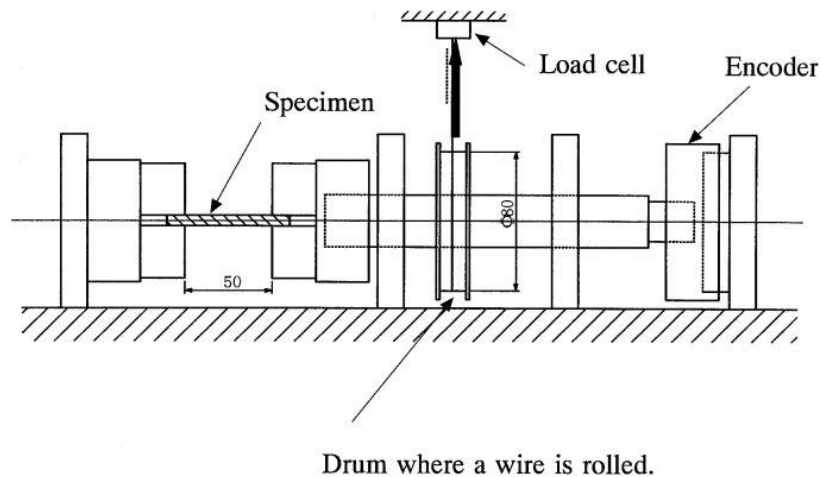
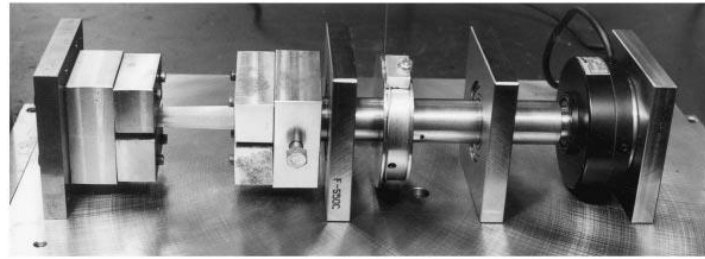


Figure II. 24. Photograph and schematic diagram of test fixture^[44]

In all ECT tests, pure mode III component is proved to be in the mid-region of the specimen, while mode II component appears near the edges. Mode II component can be reduced to a reasonable level with an appropriate choice of the specimen geometry^[39-41;42]. The closed-form expressions for determining G_{IIIc} for ECT tests are not perfect since the CC method widely used in data reduction schema is not satisfactory. It was found that G_{IIIc} increased along with the crack length^[42], but a large number of specimens with different crack lengths had to be used. Secondly, small initial crack lengths of ECT specimens should be set for measuring G_{IIIc} ^[45], but small initial crack lengths would decrease the test accuracy because of the uncertainty in the real crack length measurement. Furthermore, it is not easy to identify the crack onset in most ECT tests because there is a significant non-linearity before the peak load in the load-displacement curve associated with a R-curve effect^[39-42;46-48]. A Six-Point Edge Crack Torsion (6ECT) test was proposed by Pereira et al.^[49], whose work represents a contribution to a relatively clear identification of the critical load and evaluation of the mode III R-curve effect.

II.3.4.4. Torque Shell (TS) fixture

Recently, a novel fixture for measuring mode III toughness named Torque Shell (TS) fixture is proposed by Cricri et al.^[50]. The plates are bonded together to form an initial angle of 90° as shown in Figure II. 25. A crack starter is obtained by inserting between the two adhering surfaces a Teflon film. The specimen is placed between the shells as shown in Figure II. 26. The crack propagates when the shells are placed in a tensile machine as shown in Figure II. 27. The authors conclude that the test fixture and the approach that uses the direct identification to extract the traction-separation law are promising and it would be of interest to repeat the mode III test using a different method and also to validate results numerically. The distribution of G_{III} along the crack front and the participation of mode I and mode II components were not

presented in their work. In our opinion, there is no constraint in the z direction as mentioned in their work. So there is a possibility for the birth of mode I and mode II fracture modes.

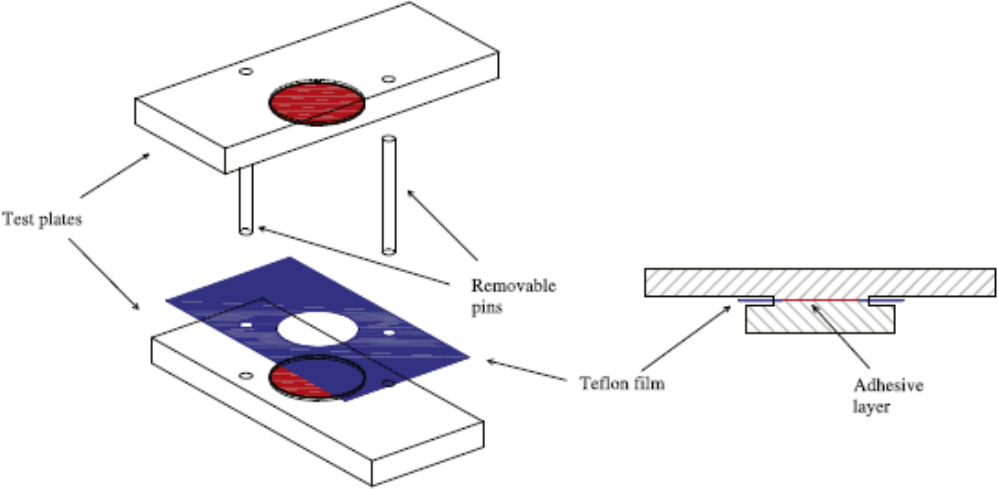


Figure II. 25. Exploded view of the test specimen obtained by bonding of two rectangular plates (left) and cross section of the circular-shaped adhesive joint (right) ^[50]

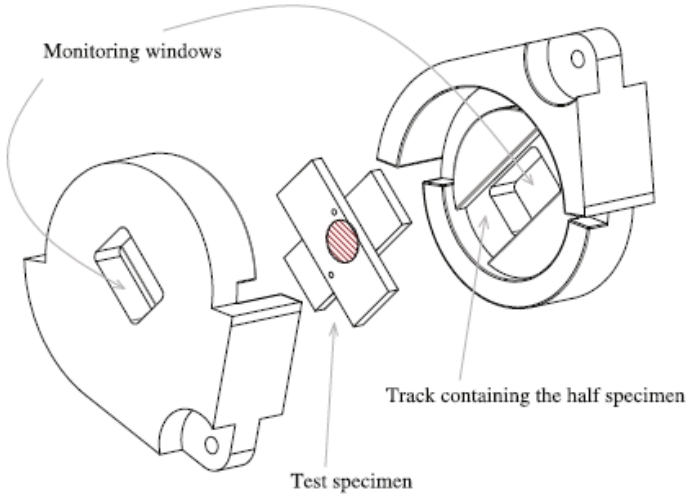


Figure II. 26. Exploded view of the shells and of the specimen being tested ^[50]

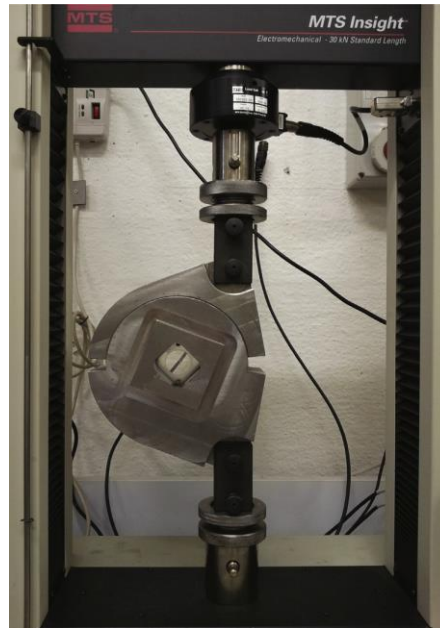


Figure II. 27. Layout of the testing apparatus ^[50]

II.3.4.5. Comparison and conclusions

A brief comparison of main pure mode III delamination tests is shown in Table. 2.

Test	Fracture modes	Uniformity of GIII along the crack front	Remarks
CRS(Simple)	III+ Δ II	ordinary	Tensile testing machine; Particular device; One crack in the thickness
CRS(Double)	III+ Δ II	ordinary	Tensile testing machine; Particular device; Two cracks in the thickness, difficult to obtain simultaneous crack onset
SCB	III+ Δ II+ Δ I	ordinary	Tensile testing machine;
MSCB	III+ Δ II	ordinary	Tensile testing machine; Complex device;
ECT-1	III+ Δ II	Dissymmetrical	Tensile testing machine; Multidirectional(MD) particular stacking sequence;
MECT-1	III+ Δ II	Good	Tensile testing machine; MD particular stacking sequence;
ECT-2	III+ Δ II	Good	Torsion testing machine ; MD particular stacking sequence;
TS	III+ Δ I+ Δ II	Unknown	Tensile testing machine; Particular device

Table. 2. Comparison of the main pure mode III tests

Unfortunately it can be seen that the participation of mode II in all these tests is never totally eliminated. The variation of G_{III} along the crack front is not negligible at all. Generally, this evolution is slighter in the central region of the crack front, but much more significant at the edges. G_{III} values can go to almost zero at the two edges of the specimen because of the edge effect. The longer the crack front, the better the G_{III} distribution. In SCB test the crack front is relatively small because beam geometry must be maintained. In ECT tests the crack front length is less limited, which represents a big advantage of these tests.

Recently, an original pure mode III test has been proposed, named Edge Ring Crack Torsion (ERCT) test ^[51]. This is a torsion test on a laminated composite plate with an edge ring delamination crack between two sub-laminates. The loading mode obtained is pure mode III, and no edge effect is introduced on the G_{III} distribution. Moreover the evolution of G_{III} along the crack front, depending on the stacking sequence of the laminates used, can be optimized in order to be more uniform.

II.3.5. Mixed mode I+II+III

In literature, some efforts have been also taken to realize mixed mode I+II+III delamination test. However, three pure mode delamination tests are the fundamental of a mixed mode delamination test. Mixed mode tests still have large room of improvement because a perfect pure mode III delamination test cannot be achieved as mentioned above.

In the work of A. Szekrényes ^[52], a double prestressed end-notched flexure (I/II/III) (PENF I/II/III) test was proposed and realized, whose approach is a superposition of the DCB (a), ENF (b) and MSCB(c), shown in Figure II. 28. Figure II. 29 shows the experimental equipment for the mixed mode I/II/III test. The mode-I component is fixed by the steel roller (7), while the mode-III component can be controlled by using the special grips of the MSCB test. The mode-III load is transferred to the specimen through four grub screws (8), the crack tearing displacement is controlled by a prestressing screw (3).

The author concluded that the main advantages of the prestressed specimens are that the material can be tested at any mode ratio and the complete fracture space can be covered. The drawbacks of the test are that the mode ratio cannot be designated before the testing process, because the mode ratio depends on the external load and also on the crack length.

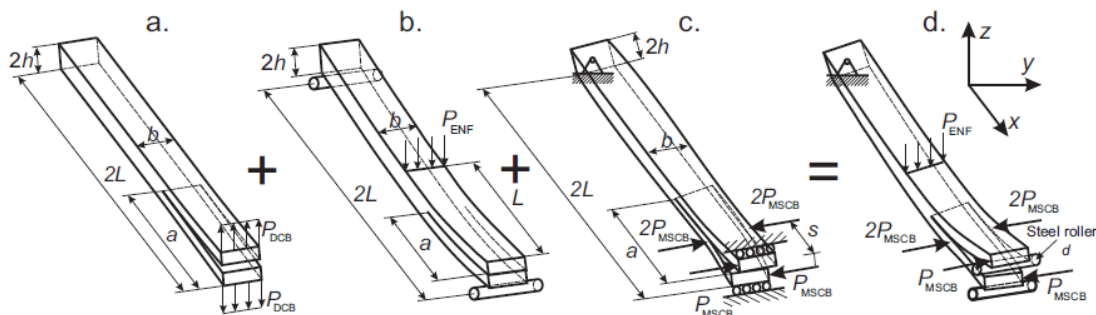


Figure II. 28. The mixed-mode I/II/III PENF specimen (d) as the superposition of the DCB (a), ENF (b) and MSCB (c) specimens

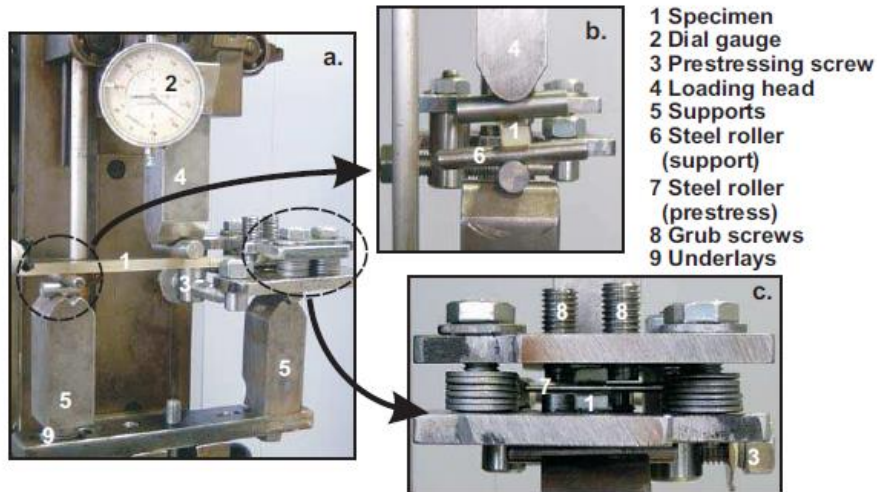


Figure II. 29. The mixed-mode I/II/III Double-Prestressed End-notched Flexure specimen

Another mixed mode I+II+III delamination test was proposed and realized by B. Davidson and F. Sediles^[31], whose approach is a superposition of a mixed-mode bending (MMB)⁵³ type arrangement for modes I and II with a modified version of the MSCB for mode III.

Figure II. 30 presents a schematic of the STB specimen and loading. In detail, P_I , P_{II} and P_{III} represent the mode I, mode II and mode III loadings respectively. T is a torque about the z axis imposed as a boundary condition. To reproduce the MSCB loading, one would choose $T = P_{III} \times a$, so that $M_Z = 0$ at the delamination front. Figure II. 31 shows the schematic of test set-up for the mixed mode I/II/III test.

The authors concluded that the STB is a promising method for evaluating mixed mode (including mode III component) toughness of a laminated composite.

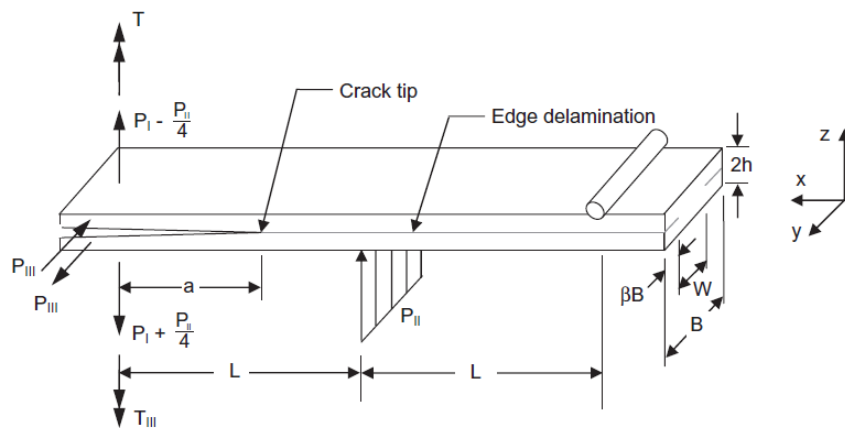


Figure II. 30 STB specimen and loading^[31]

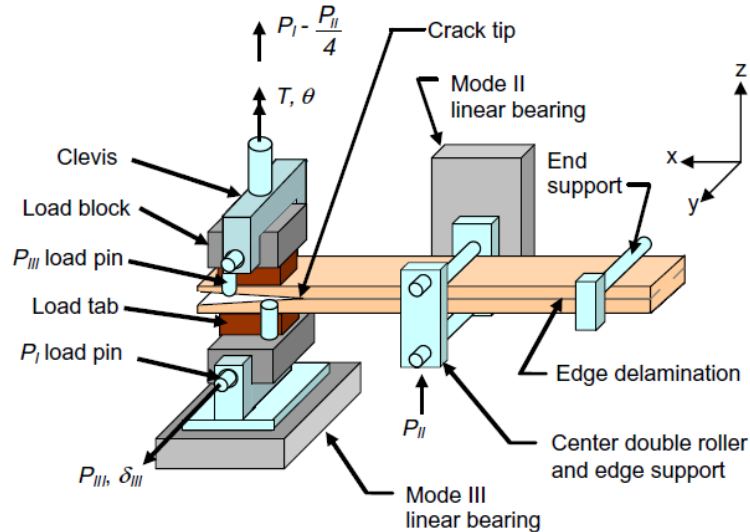


Figure II. 31 Schematic of test set-up ^[31]

II.3.6. Summary

A literature review of pure mode III delamination tests and mixed mode tests has been given. Different from standardization of mode I (DCB) and mode II (ENF) tests, the investigation of delamination behavior with the participation of mode III is quite limited. Even in the case of pure mode III loading, the determination of the toughness has been proven to be a complex issue for laminated polymeric matrix composites. In most cases, the evolution of G_{III} along the crack front is not uniform. Actually, the evolution of G_{III} along the crack front can be observed slight in the central region of the crack front, while it becomes more significant at the extremities of the crack front due to the free edge effects. Unfortunately, mode II component can never be totally eliminated in most cases. As a result, it is difficult to propose an exact closed-form expression for mode III tests because the average value of the G_{III} along the crack front is considered as the toughness G_{IIIc} . And it is not so meaningful if the distribution of G_{III} along the crack front has an important amplitude.

Determination of the critical load corresponding to a crack onset is problematic. There is always a nonlinear part before reaching to the critical load in a load/displacement curve.

Some efforts have also been taken for realizing mixed mode I+II+III delamination test. Generally, it is a superposition of three basic pure modes. Therefore, the success of mixed mode delamination tests is based on standardized pure mode delamination. However, characterization of pure mode III delamination behavior remains a complex issue. That's our motivation to focus on development of pure mode III delamination tests firstly.

II.4. Finite element analysis for simulation of delamination behavior

Finite element method is used for two purposes: evaluate the stress energy release rates in a given configuration or predict the crack propagation. Several widely used finite element methods are introduced in this section.

II.4.1. VCCT method to calculate strain energy release rate

Virtual crack closure technique (VCCT) ^[54-58] is a widely used method to determine strain energy release rate along a crack front, in which the nodal forces at the crack front and the displacements behind the crack front are used. The formulas (Eq. 25) for calculating G_I , G_{II} and G_{III} for three dimensional eight-nodded solid components were given by Rybicki and Kanninen ^[54].

$$G_I = \frac{F_{zj}\delta_{zj}}{2\Delta a\Delta y}, \quad G_{II} = \frac{F_{xj}\delta_{xj}}{2\Delta a\Delta y}, \quad G_{III} = \frac{F_{yj}\delta_{yj}}{2\Delta a\Delta y} \quad \text{Eq. 25}$$

, where Δy is the sum of the one-half the element lengths on either side in the y direction and Δa is the element length in x direction as shown in Figure II. 32. Note that the crack front forces required for holding together node pair B are the same as the forces that would be required to keep node pair A and A' closed if the mesh is sufficiently refined.

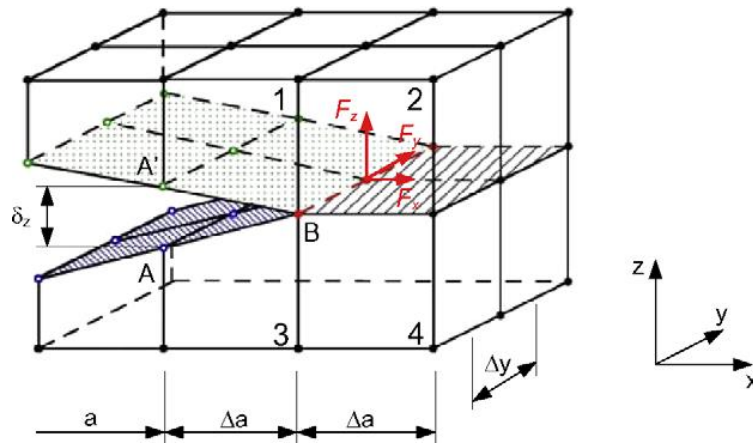


Figure II. 32 VCCT for three dimensional eight-nodded solid elements ^[55]

II.4.2. J-integral method

The concept of the integral J was introduced by RICE ^[59]. The method to calculate the stress-intensity factor was an interaction J-integral method conducted with ABAQUS, and is required to separate the components of the stress-intensity factors for a crack under mixed-mode loading. The method is applicable to cracks in isotropic and anisotropic materials. The interaction integrals J_{int}^α can be expressed ^[60] as:

$$J_{int}^\alpha = \lim_{\Gamma \rightarrow 0} \int_{\Gamma} \mathbf{n} \cdot (\boldsymbol{\sigma} : \boldsymbol{\varepsilon}_{aux}^\alpha \mathbf{I} - \boldsymbol{\sigma} \frac{\partial u}{\partial x}^\alpha - \boldsymbol{\sigma}_{aux}^\alpha \boldsymbol{\sigma} \frac{\partial u}{\partial x}) \mathbf{q} d\Gamma \quad \text{Eq. 26}$$

with

Γ : an arbitrary closed contour surrounding vanishing on the faces of the crack and surrounding the crack tip;

\mathbf{q} : unit vector in the virtual crack extension direction;

\mathbf{n} : the outward normal to Γ ;

$\boldsymbol{\sigma}$: the stress tensor;

u : the displacement vector (Figure II. 33).

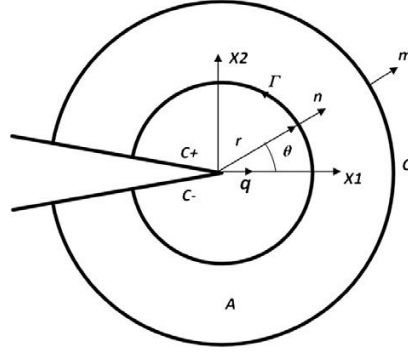


Figure II. 33 Contour for evaluation of J-integral

The subscript α represents three pure mode I, mode II, and mode III loading fields when α equals to I, II, and III, respectively. The domain form of the interaction J-integral is:

$$J_{int}^{\alpha} = \int_A \lambda(s) \mathbf{n}(\sigma: \varepsilon_{aux}^{\alpha} \mathbf{I} - \sigma \left(\frac{\partial \mathbf{u}}{\partial \mathbf{x}} \right)_{aux}^{\alpha} - \sigma_{aux}^{\alpha} \sigma \frac{\partial \mathbf{u}}{\partial \mathbf{x}}) \mathbf{q} dA \quad Eq. 27$$

, where $\lambda(s)$ is the virtual crack advance and dA the surface element. In the interaction J-integral method^[60] the two-dimensional auxiliary fields are introduced and superposed on the actual fields. By judicious choice of the auxiliary fields, the interaction J-integral can be directly related to the stress-intensity factors as:

$$\mathbf{K} = 4\pi \mathbf{B} \mathbf{J}_{int} \quad Eq. 28$$

where \mathbf{B} is called the pre-logarithmic energy factor matrix, $\mathbf{J}_{int} = [J_{int}^I, J_{int}^{II}, J_{int}^{III}]$ and $\mathbf{K} = [K_I, K_{II}, K_{III}]$. In linear elastic fracture mechanics, the J-integral coincides with total energy release rate, $J = G_T = G_I + G_{II} + G_{III}$ where G_I , G_{II} and G_{III} are associated with K_I , K_{II} and K_{III} , respectively^[61]. \mathbf{B} is diagonal for homogeneous and isotropic materials and the above equation is simplified to:

$$G_I = \frac{K_I^2}{E} \quad Eq. 29$$

$$G_{II} = \frac{K_{II}^2}{E} \quad Eq. 30$$

$$G_{III} = \frac{K_{III}^2}{2\mu} \quad Eq. 31$$

with

E : Young's modulus;

μ : Shear modulus;

$\bar{E} = E$ for plane stress, $\bar{E} = E / (1 - \nu^2)$ for plane strain conditions

This integral has interesting characteristics: firstly, it is independent of the selected contour, so it is possible to choose a distant contour from the crack front, thus avoiding the singularity zone; Then, this integral is not sensitive to elements size at the crack front; finally this integral is equal to the strain energy release rate if the material behavior is linear elastic.

II.4.3. Perturbation method

This technique allows calculating G_I , G_{II} and G_{III} quickly. It assumes that a virtual advance Δa of a crack causes only a variation in the stiffness matrix without any modification of the displacement field and the external forces. Note that the advance of crack Δa disrupts elements containing the nodes of the crack front and the variation of the stiffness matrix is carried out locally. The values determined by this method are not very sensitive to the size of elements in the vicinity of the crack if it is reasonably defined.

II.4.4. Cohesive Zone Model

The notion of cohesive force at crack front was introduced by Barenblatt ^[62]. Cohesive Zone Model (CZM) provides an effective methodology to study and simulate fracture in solids especially delamination in composite materials. Thus, it is widely used to characterize crack propagation behavior ^[63-66]. These finite elements are used to model the interface between surfaces which would be separated when the crack propagates.

In most formulations, the behavior consists of a reversible linear increase in the stress of “traction” with the relative displacement of “separation” of the nodes firstly. As the cohesive surfaces separate, traction first increases until a maximum is reached, and then subsequently reduces to zero which simulates a softening of damaged material and results in complete separation. The variation of traction in relation to displacement is plotted on a curve and is called Traction-Separation-Load-Curve (TSLC), shown in Figure II. 34, which plays a vital role in the quality of the results obtained by numerical simulation. The TSLC relates the traction between originally coincident nodes located on either side of the crack and their relative displacement (opening/sliding). The area under this curve represents the energy needed to break the element. CZM maintains continuity conditions mathematically despite physical separation. Thus, it eliminates singularity of stress and limits it to the cohesive strength of the material.

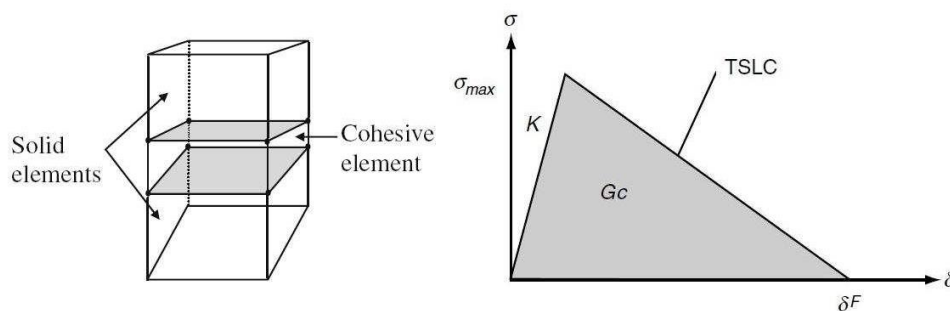


Figure II. 34. Cohesive Zone Model

There are many forms of TSLC laws in the literature (Figure II. 35): bilinear ^[67], multilinear, exponential ^[68], trapezoidal ^[69], polynomial ^[70]. Herein, we introduce a widely used bilinear form in details. The parameters describing that bi-linear form are:

- The area under the curve corresponding to the critical strain energy release rate G_C ;
- The slope of the first linear part of the curve K representing the stiffness of the cohesive area; The tensile strength σ_{max} corresponding to the element’s damage initiation;
- The ultimate displacement δ_f corresponding to the displacement of the nodes at fracture of the cohesive zone.

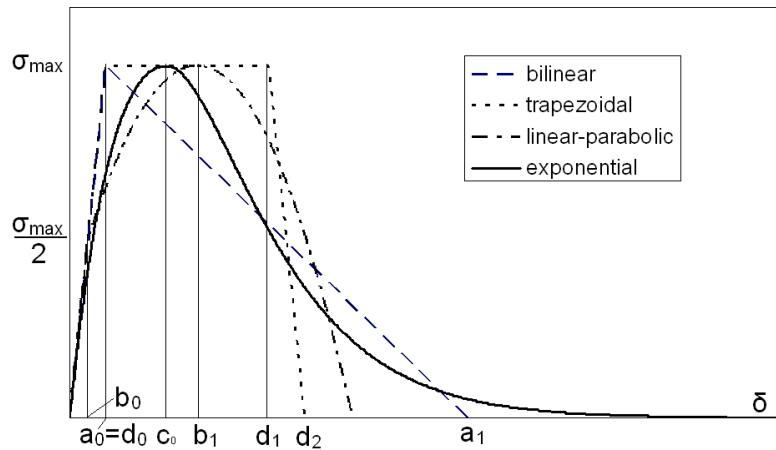


Figure II. 35. Various forms of TSLC laws

CZM have several main advantages:

- It can model the behavior of a sealing surface from its linear behavior, onset and propagation of crack to the final fracture in a single analysis, without the need for remeshing or treating the fields of global constraints in the system;
- However, the main inconvenient is that:
- The parameters characteristic of TSLC are neither clearly related to the mechanical properties of the substrates nor to those of the adhesive layer. The choice of these parameters is still very problematic in modeling by MZC.

II.4.5. Summary

Finite element methods to characterize delamination behavior are introduced. VCCT and CZM are discussed especially and chosen for our coming study. VCCT allows calculating strain energy release rates for each element of the crack front. It is widely used to predict crack onset and distribution of strain energy release rate along a crack front. CZM allows characterizing crack propagation by avoiding singularity of stress and limiting it to the cohesive strength of the material. However, the determination of the characteristic parameters of TSLC is still a complex issue, which are neither clearly related to the mechanical properties of the substrates nor to those of the adhesive.

II.5. Summary

In this chapter, mechanisms of damage and fracture of laminated composite, most existing fracture criteria, most delamination testing methods with the participation of mode III, finite element methods to characterize and predict delamination behavior are reviewed.

First of all, most damages modes in a laminated composite are discussed with a particular focus on delamination which is one of the most common and dangerous damage modes in a laminated composite under impact and fatigue loadings.

Then criteria for the prediction of composite damage and fracture are introduced. Fracture mechanics is preferred to characterize delamination behavior dues to the singularity at crack tip. Generally, delamination occurs in mixed mode I + II + III. In order to establish and identify a general criterion, one must firstly know how to measure the delamination toughness in each pure mode. Then mixed mode I+II and I+III delamination behaviors should be

characterized. Determination of the delamination toughness of laminated composites with the participation of mode III components remains a difficult task. Currently, delamination tests in pure mode I, pure mode II, as well as mixed mode I+II are widely studied. On the contrary, work regarding the participation of mode III is quite limited.

Most pure mode III and mixed mode delamination tests involving mode III in literature are reviewed. Pure mode III delamination test is not simple to achieve with uniform distribution of G_{III} along the crack front, which is required by an exact and meaningful closed-form expression and the achievement of pure mode III test is also the fundamental of a successful mixed mode delamination test.

In order to study delamination phenomenon in a laminated composite, finite element analysis is shown necessary. Some kinds of numerical simulation methods are summarized, among which VCCT and CZM are preferred in this study. VCCT can predict the crack onset and calculate strain energy release rates along a crack front while CZM allows characterizing crack propagation.

In the study, we focus on the delamination in pure mode III first of all, and then mixed mode delamination with participation of mode III. A dialogue between FEM and experiments is the basement of our approach.

CHAPTER III. PRELIMINARY STUDY

III.1. Materials and laminate manufacturing

In this research work, all specimens are obtained from a woven carbon/epoxy prepreg (ref: IMP503Z), which is a taffeta fabric.

All composite laminates are fabricated by hand lay-up technique and a polymer film of 13 μm thick is embedded in the midplan in order to create a pre-crack. For ECT specimens, the crack tip is straight and for ERCT the crack tip is circular. The composite laminates are cured in hot-press machine with a proper curing cycle of 30 minutes at 110 $^{\circ}\text{C}$ under 1 bar of pressure and then 1 hour at 125 $^{\circ}\text{C}$ under 2 bars of pressure.

III.2. Composite materials characterization

III.2.1. Characterization tests

In order to obtain the principal material constants, referenced to the standards for composite material ASTM Standard D3039M-00 and D3518M-94, some classical tests were carried out on the specimens of unidirectional laminates.

Firstly, tensile tests were performed on the specimens at 0 $^{\circ}$ (with fiber orientation 0/90) and also on those at 90 $^{\circ}$ (with fiber orientation 90/0), in order to verify the influence of chain/frame weaving on this balanced fabric. Tensile tests on the specimens of 0 $^{\circ}$ (with fiber orientation 0/90) allow to measure

- Longitudinal and transverse modulus: E_{11} , E_{22} ;
- Poisson's ratio ν_{12} ;
- Tensile strength in direction 1 and 2: X^+ , Y^+ ;

Tensile tests on the specimens at 45 $^{\circ}$ (with fiber orientation ± 45) provide

- Shear modulus in direction 12: G_{12} ;
- Shear strength in direction 12: S_{12} .

III.2.2. Experimental

An 8 prepreg plies plate with the stacking sequence $[0_8]$ was fabricated where 0 represents a taffeta balanced fabric ply with yarns oriented in 0 $^{\circ}$ and 90 $^{\circ}$. And then the plate was cut into 3 specimens for each tests along 0 $^{\circ}$, 90 $^{\circ}$ and 45 $^{\circ}$ relative to the fiber orientation, which were named 0 $^{\circ}$ -1~3, 90 $^{\circ}$ -1~3 and 45 $^{\circ}$ -1~3 respectively. Dimensions of the specimens are shown in Table. 3.

Specimens	h (mm)	b (mm)
0 °-1	1.68	23.13
0 °-2	1.76	22.90
0 °-3	1.66	22.71
90 °-1	1.76	23.36
90 °-2	1.75	23.20
90 °-3	1.75	22.84
45 °-1	1.71	23.26
45 °-2	1.73	23.08
45 °-3	1.72	23.28

Table. 3. Dimensions of the unidirectional specimens

The specimens were placed under axial tensile load until complete fracture. The longitudinal and transverse deformations were observed by an extensometer and a strain gauge during the tests.

III.2.3. Results and discussions

Figure III. 1 and Figure III. 2 give the linear part of tensile stress/strain curves for the specimens 0 °-1~3, 90 °-1~2 and 45 °-1~2 respectively. In order to protect the extensometer, tests were paused before the fracture and the extensometer was taken off, and then the specimen was reloaded until the fracture to measure the strength. As a result, we don't have a complete stress/strain curve. Note that the tests with specimens 90 °-3 and 45 °-3 didn't succeed. The curves for the specimens 0 ° and 90 ° are found in same figure where the slopes of their linear part are shown substantially the same for the taffetas prepreg tested. So the average value was calculated on all measured modulus from the specimens 0 ° and 90 ° with the consideration of $E_{11}=E_{22}$. Poisson's ratio ν_{12} is also determined as the ratio of the transverse strain over longitudinal strain for the specimens 0 ° and 90 ° specimens. The in-plane shear modulus G_{12} is calculated according to the slope of the linear part of the curves in Figure III. 2.

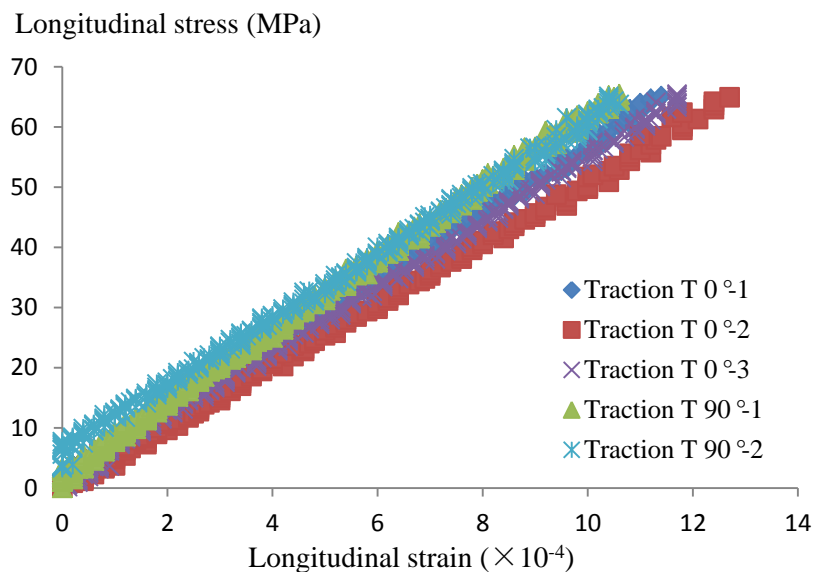


Figure III. 1. Experimental stress/strain curves for the specimens 0° and 90°

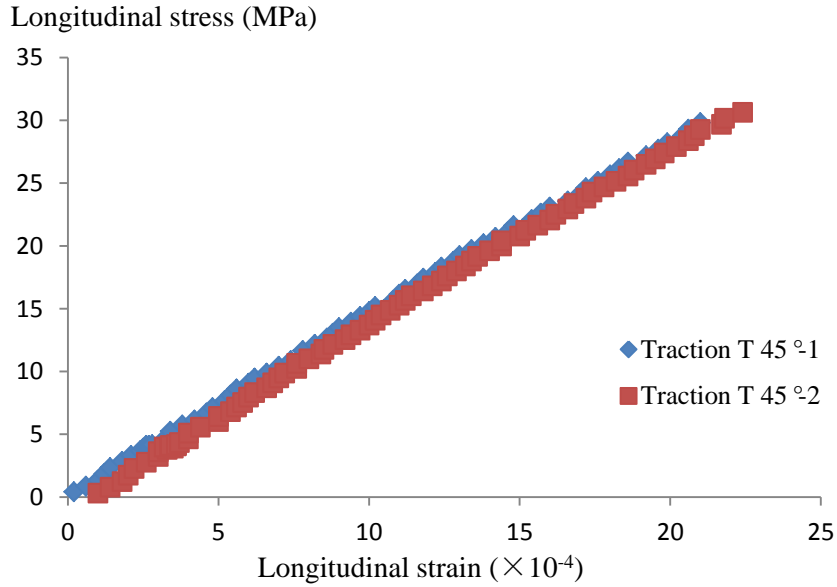


Figure III. 2. Experimental stress/strain curves for the specimen 45°

The maximum tensile strengths were also obtained for all the specimens 0° and 90°, the average values of which are considered as X^+ and Y^+ . The inplane shear strength, S_{12} , can be also obtained from the tensile tests on 45° specimens Figure III. 2. All the results are listed in Table. 4.

Name of the specimen	T0-1	T0-2	T0-3	T90-1	T90-2	T90-3	Average value
Longitudinal and transverse modulus: $E_{11}=E_{22}$ (MPa)	55152	51107	54379	60028	55581	-	55250±3197
Tensile strength in direction 1 and 2: $X^+=Y^+$ (MPa)	782.8	773.2	738.6	569.7	524.7	625.5	669±111
Name of the specimen	T45-1	T45-2	T45-3				
Shear modulus 12 (MPa)	4036	4089					4062±37
Shear strength in direction 12: S_{12} (MPa)	124	113	115				117±6
Poisson's ratio 12: ν_{12} (MPa)							0.044

Table. 4. Mechanical properties of the tested laminates

III.3. Establishment of the finite element models

Finite element analysis was carried out using LS-dyna in order to characterize the delamination behaviors of laminated composites. The fixtures and specimens were modeled with 3D solid elements. Spring elements were arranged along the crack front in order to obtain loads at the crack front. Then VCCT was performed to determine the evolution of G_I , G_{II} and G_{III} along the crack front.

Every ply was set up according to the stacking sequence independently and then merged together. In the pre-crack plane, only the non-delaminated area is merged. A surface contact, named Contact_automatic_surface_to surface, was applied in most finite element models on the two delamination surfaces to prevent interpenetration during the analysis. Relative sliding between points within the delamination plane was assumed to be frictionless.

(1) material model for laminate

MAT 22 was chosen to simulate the composite laminates due to its better performance, where geometry nonlinear shear behavior and Changchang fracture criterion for orthotropic materials have been adopted. In fact, both of MAT22 and MAT59 were employed in same models firstly. In our context, finite element models with these two kinds of material models give similar results. The variation curve of strain energy release rate obtained is smoother from models with MAT59. However, the mechanical criterion for MAT59 is Maximum Stress Failure Criterion, which cannot fit for our situation very well. The principal mechanical properties of material were set according to Table. 1.

(2) material model for steel device

In most finite element models, an elastic material model is employed for simulate devices. The material parameters are shown in Table. 5.

Young's modulus E	2.1×10^5 (MPa)
Poisson's ratio ν	0.3

Table. 5. Mechanic properties of steel devices

(3) material model for spring element

The material parameters of spring element are shown in Table. 6.

Translational stiffness about local r-axis	1×10^8 (N/mm)
Translational stiffness about local s-axis	1×10^8 (N/mm)
TKT: Translational stiffness about local t-axis	1×10^8 (N/mm)

Table. 6. Mechanic properties of steel devices

(4) material model for glue

Bondline of glue is used in some finite element models. An elastic material model was employed to simulate the bondline. The parameters are set as Table. 7.

Young's modulus E	1800 (MPa)
Poisson's ratio ν	0.3

Table. 7. Mechanic properties of bondline

Finally, the boundary conditions should be well considered. Generally, the boundary conditions are set according to the corresponding experiments. A displacement/time curve is set in tensile or compression tests while rotation/time curve is set in torsion tests.

III.4. Tests of delamination under pure mode I (DCB) and pure mode II (ENF)

In order to compare with mode III delamination toughness and new proposed mode I and mode II delamination tests, widely used pure mode I test Double Cantilever Beam (DCB) and mode II test End Notched Flexion (ENF) were carried out on the same composite.

III.4.1. Experimental

The composite laminate was manufactured by hand lay-up technique according to the stacking sequence highlighted in chapter I and a 13 μm thick polyester film was inserted in the midplane in order to create a pre-crack. Specimens with different initial crack lengths, a (defined in Figure III. 3) were employed in order to apply experimental compliance calibration method. At least 3 specimens were tested for each specimens configuration.

As mentioned in chapter II, Irwin-Kies equation Eq. 1 is applied to evaluate delamination toughness with different compliance calibration method. Finite element analysis by VCCT was also carried out to determine the mode I delamination toughness.

(1) Double Cantilever Beam (DCB) pure mode I test

Firstly, two steel parts were pasted on the head of DCB specimen. Then the specimen was placed under pure tensile load in the way shown in Figure III. 3 and Figure III. 4. An axial displacement speed of 2mm/min was imposed until the crack onset.

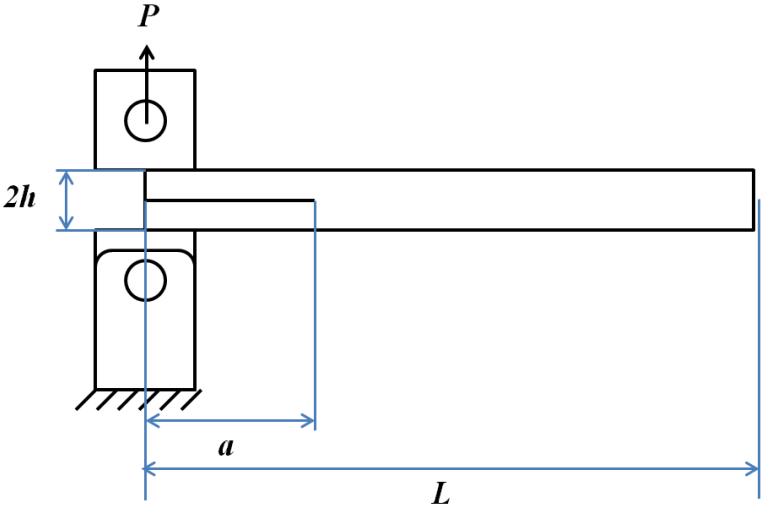


Figure III. 3. Schema of Double Cantilever Beam test



Figure III. 4. A picture of DCB specimen and test

A theoretical model based on the beam theory was used to determine the mode I toughness. The classic beam theory without the shearing effect allows expressing compliance along with crack length and material parameters.

$$C = \frac{2a^3}{3EJ} = \frac{\delta}{P} \quad \text{Eq. 32}$$

, where a is the crack length; E is the longitudinal Young modulus; δ is the opening between the two sub-laminates; J the moment of inertia of a sub-laminate given by:

$$J = \frac{bh^3}{12} \quad \text{Eq. 33}$$

So the G_{IC} is expressed as

$$G_{IC} = \frac{3\delta_c P_c}{2ba} \quad \text{Eq. 34}$$

, where δ_c is the opening between the two sub-laminates corresponding to the critical load P_c . And b is the width of the specimen.

The compliance calibration (CC) method with two compliance laws was also used in the DCB test. The compliance law proposed by Berry (Berry's Law), which is widely used in literature, is expressed by Eq. 35.

$$C = \alpha a^u \quad \text{Eq. 35}$$

where α and u are parameters intrinsic to material, determined by interpolation of the experimental compliance as a function of the initial crack length: C/a .

By applying Berry's law, the Irwin-Kies' formula is expressed as Eq. 36.

$$G_{IC} = \frac{P_c^2}{2b} \alpha u a^{u-1} \quad \text{Eq. 36}$$

Another compliance law inspired by the beam theory (Beam Law) is also common in literature as shown in Eq. 37

$$C = Aa^3 + B \quad \text{Eq. 37}$$

where A and B are determined by interpolation of the experimental compliance C versus a^3 .

By applying Beam law, the formula Irwin-Kies is expressed as Eq. 38.

$$G_{IC} = \frac{3P_c^2}{2b} Aa^2 \quad \text{Eq. 38}$$

The dimensions of specimens are listed in Table. 8. Every dimension is measured 3 times at least and the average value is presented in the table. b is the width of DCB specimen.

Test	b (mm)	$2h$ (mm)	a (mm)
DCB1-1	21.07	3.55	41.81
DCB1-2	21.07	3.55	46.31
DCB1-3	21.07	3.55	54.71
DCB1-4	21.07	3.55	67.11
DCB1-5	21.07	3.55	77.81
DCB1-6	21.07	3.55	83.81
DCB2-1	20.52	3.48	41.43
DCB2-2	20.52	3.48	46.43
DCB2-3	20.52	3.48	57.43
DCB2-4	20.52	3.48	68.93
DCB2-5	20.52	3.48	78.93
DCB2-6	20.52	3.48	84.93
DCB3-1	20.62	3.47	41.89
DCB3-2	20.62	3.47	43.97
DCB3-3	20.62	3.47	54.97
DCB3-4	20.62	3.47	64.37
DCB3-5	20.62	3.47	76.17
DCB3-6	20.62	3.47	81.67

Table. 8. Dimension of DCB specimens

(2) End Notched Flexion (ENF) pure mode II test

The specimen was placed under 3 points bending load as shown in Figure III. 5 and Figure III. 6. An axial displacement speed of 2mm/min was imposed until the crack onset. Remarks on the surface of the specimen and the device help ensure the specimen location.

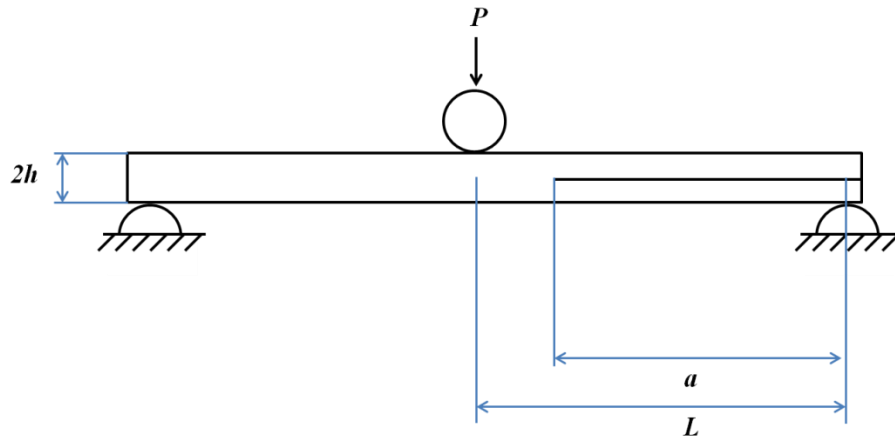


Figure III. 5. Schema of End Notched Flexion test



Figure III. 6. A picture of ENF test

Theoretical model based on the beam theory was used to determine the mode II toughness. And G_{IIC} is expressed as Eq. 39.

$$G_{IIC} = \frac{9\delta_c P_c a^2}{2b(2L^3 + 3a^3)} \quad \text{Eq. 39}$$

, where δ_c is the opening between the two sub-laminates corresponding to the critical load P_c . And a , b and L are the crack length, the width and length of the specimen.

Irwin-Kies' formula (Eq. 39) with beam theory compliance law (Eq. 37) is applied in ENF test. The dimensions of ENF specimens are listed in Table. 9. Every dimension is measured 3 times at least and the average value is presented in the table.

Test	b	$2h$	L (mm)	a (mm)
ENF1-1	20.7	3.55	50	15
ENF1-2	20.7	3.55	50	20
ENF1-3	20.7	3.55	50	25
ENF1-4	20.7	3.55	50	30
ENF1-5	20.7	3.55	50	35
ENF1-6	20.7	3.55	50	40
ENF2	20.8	3.58	50	40
ENF3	20.2	3.62	50	40
ENF4	20.4	3.70	50	40

Table. 9. Dimensions of ENF specimens

III.4.2. Finite element analysis

16 plies were set up for DCB and ENF tests according to the stacking sequence highlighted in chapter I and were separated symmetrically into two sub-laminates by the crack plane. In DCB model, the crack length $a=40\text{mm}$ while the rest specimen dimensions are the same as in Table. 8. In ENF test, $a=40\text{mm}$ as well while the other dimensions are the same as in Table. 9.

The boundary conditions were carefully set in order to simulate real experimental loading conditions. In the DCB model, as shown in Figure III. 7, the tensile load was imposed by a displacement curve 7.5mm in the thickness direction on the edge of one arm while the symmetrical edge was fixed. Besides, the degree of freedom in the thickness direction at the free edge was restricted by the point A (defined in Figure III. 7). In the ENF model, as shown in Figure III. 8, the compression loaded in the middle was imposed in the manner of a displacement curve 8mm using a cylinder. Two supporting cylinder were fixed. A surface to surface contact was set between the specimen surface and the cylinders, as well as between the two arms of the specimen.

The mesh close to the crack front was locally refined according to literature ^[71-74] to guarantee a good accuracy of the results.

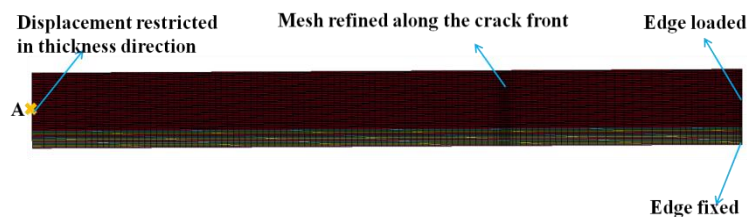


Figure III. 7. Mesh for DCB test

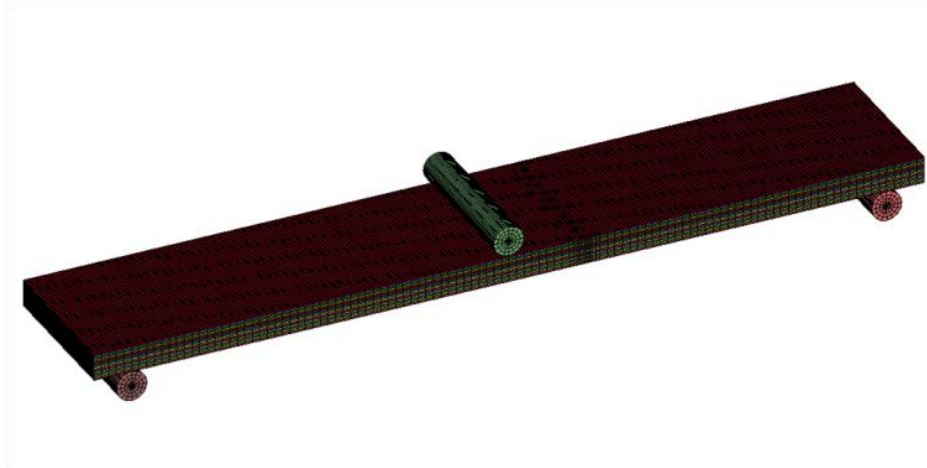


Figure III. 8. Mesh for ENF test

III.4.3. Results and discussions

(1) DCB pure mode I test

According to experimental load/displacement curves, no non-linear part appeared before the onset of the crack propagation (Figure III. 9). So the critical load, P_C , can be determined easily. Actually, in order to apply compliance calibration methods, a series of compliances corresponding to different initial crack lengths were obtained experimentally. Figure III. 10 and Figure III. 11 show the interpolations of C/a^3 in Beam law (Eq. 37) and C/a in Berry's law (Eq. 35). The interpolation is precise with a correlation coefficient larger than 0.99.

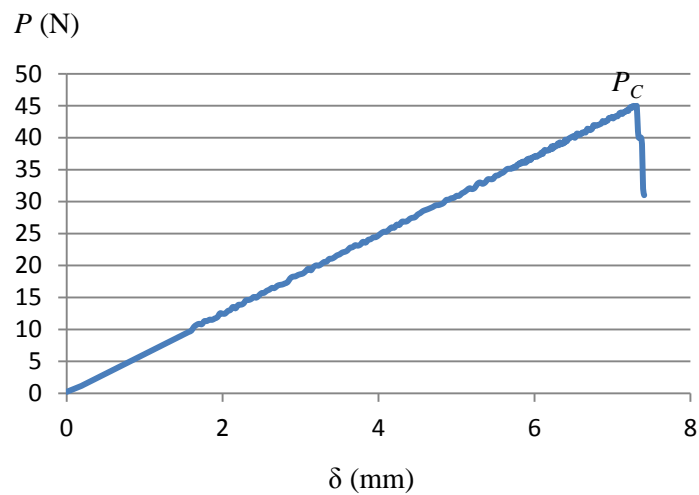


Figure III. 9. An experimental load-displacement curve in DCB test

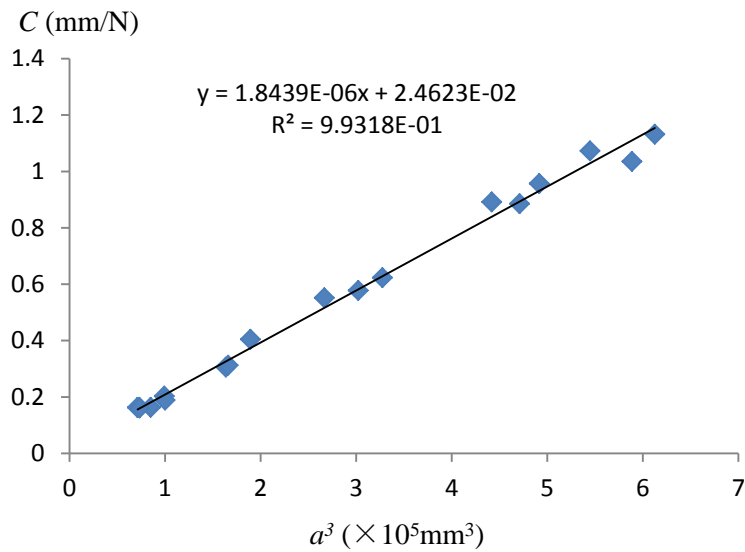


Figure III. 10. Interpolation of C/a^3 for Beam compliance law (Eq. 37)

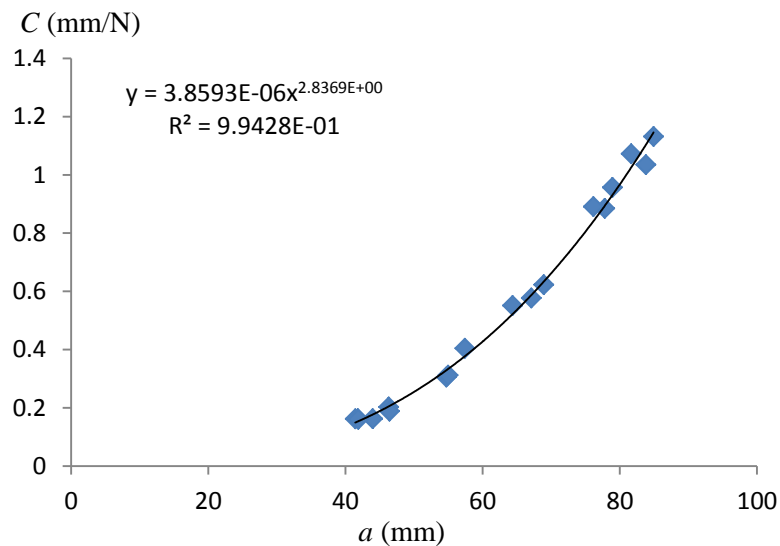


Figure III. 11. Interpolation of C/a for Berry compliance law (Eq. 35)

In DCB test, P_C is determined as the loading value at the end of the linear part of the load/displacement experimental curve. The results of G_{IC} from different methods are listed in Table. 10. It is shown that the value from the beam theory is 21.1% bigger than the one from compliance calibration using the Beam law, and 12.5% bigger than that of from compliance calibration using Berry's law.

G_{IC} (N/m)	$G_{IC-Theory}$	$G_{IC-Beam\ law}$	$G_{IC-Berry's\ law}$
Test 1	587.5	485.6	522.7
Test 2	550.6	444.1	478.8
Test 3	533.0	449.2	483.5
Average	557	460	495
Standard deviation	28	24	23

Table. 10. Results of G_{IC} from different methods for DCB test

Figure III. 12 illustrates the evolution of G_I , G_{II} and G_{III} along the crack front computed at P_C obtained by VCCT on the finite element DCB model. It demonstrates that a pure mode I delamination is obtained. The values of G_I vary along the crack front and drop to 0 at the two extremities of the crack front while the maximum value appears in the middle domain. If we define a relative variation parameter as following: $\Delta = (|G_{I-max} - G_{I-av}|) / G_{I-av}$, then Δ is 29.1% in DCB test.

Finally, the values of G_{IC} in Table. 10 are also presented in Figure III. 12, where $G_{IC-Theory}$, $G_{IC-Beam\ law}$ and $G_{IC-Berry's\ law}$ are bigger than G_{IC-FEM} , the average value of G_I computed at P_C using VCCT, by 60%, 32.3% and 42.3% respectively. It is interesting to note that G_{I-max} obtained by FEA agrees well with that from the beam theory, so closer to those from compliance calibration methods. Actually, when the G_{I-max} value attains the toughness of the material, the onset of the crack propagation occurs. Herein the average value has less physical sense. As in literature, $G_{IC-Beam\ law}$ and $G_{IC-Berry's\ law}$ are usually considered as a precise mode I delamination toughness. It is decided that only $G_{IC-Beam\ law}$ will be compared with other delamination test thereafter.

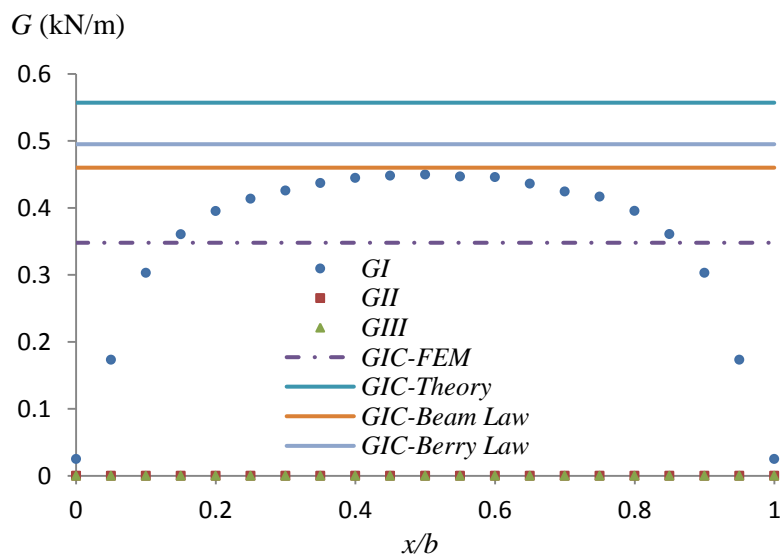


Figure III. 12. Evolution of G_I , G_{II} and G_{III} along the crack front of DCB specimen and comparison of the average value of G_{IC} from different methods

(2) ENF pure mode II test

Figure III. 13 gives a typical experimental load/displacement curve obtained from ENF pure mode II tests. After a linear behavior, the load shows a small drop and then, the slope of the

curve goes down progressively. The onset of the crack growth has been observed after the linear part, so the critical load corresponding to the end of the linear part is defined. In order to apply the compliance calibration method, a series of compliances have been measured on the linear part of each tested specimen having different initial crack lengths. Figure III. 14 shows the interpolation of C/a^3 with the Beam Law (Eq. 37). The interpolation is precise with a correlation coefficient larger than 0.96.

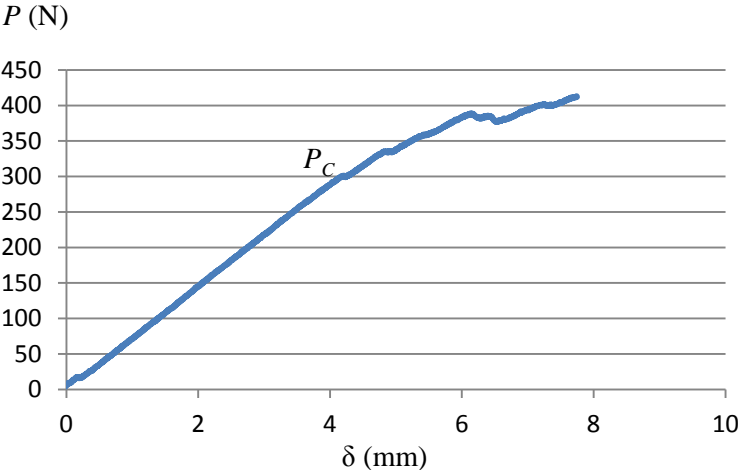


Figure III. 13. An experimental load-displacement curve in ENF test

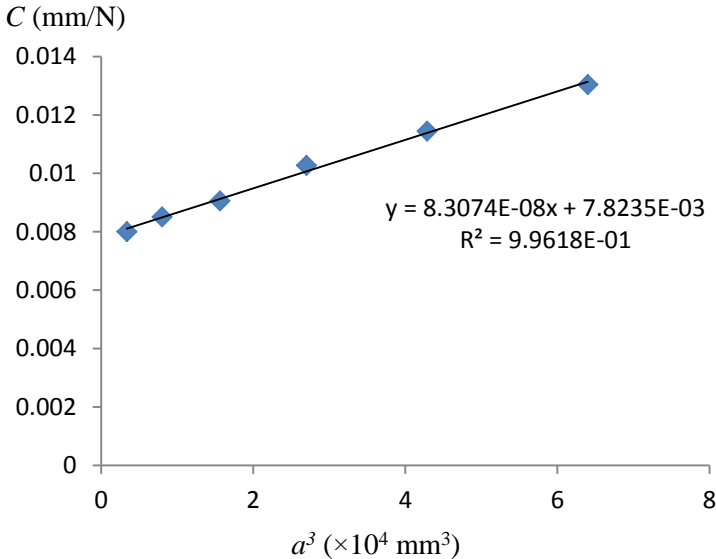


Figure III. 14. Interpolation of C/a^3 for Beam model compliance law (Eq. 37)

In ENF test, the critical load P_C is determined at the end of the linear part of the experimental load/displacement curve mentioned above. The results of G_{IIc} from two methods are listed in Table. 11. The test reproducibility is good with a standard deviation around 5%. The theoretical value of G_{IIc} is 11.1% larger than that the one from the compliance calibration method. As in literature, the value from the beam law is usually used as the mode II delamination toughness.

G_{IIC} (N/m)	$G_{IIC-Theory}$	$G_{IIC-Beam\ law}$
Test 1	970	911
Test 2	1123	982
Test 3	934	830
Test 4	1032	932
Average	1015	914
Standard deviation	83	63

Table. 11. Results of G_{IIC} from different methods

Figure III. 15 shows the evolution of G_I , G_{II} and G_{III} along the crack front computed at P_C obtained by VCCT using the finite element ENF model. It demonstrates that a main mode II delamination is obtained. The values of G_{II} are nearly uniform in the middle domain while they have a relatively big variation near the extremities of the crack front, where a small participation of mode III appears. The relative variation parameter Δ is approximately 7.2%. Finally, the values of $G_{IIC-Theory}$ and $G_{IIC-Beam\ law}$ in Table. 11 are also presented in the same figure, which are bigger than $G_{IIC-FEM}$ by 37.7% and 24.0%, respectively.

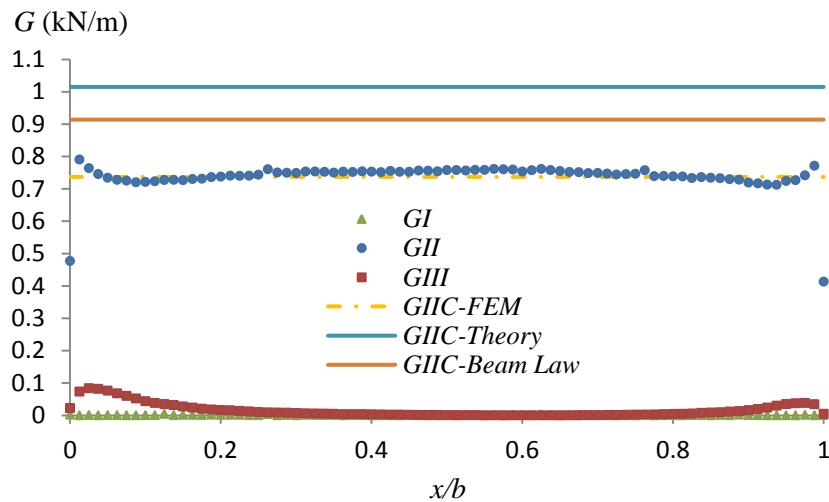


Figure III. 15. Evolution of G_I , G_{II} and G_{III} along the crack front of ENF specimen and comparison of the average value of G_{IIC} from different methods

III.4.4. Conclusions

DCB and ENF tests were performed for characterizing the delamination behavior under pure mode I and mode II loadings. The results were listed in Table. 12, where G_{CC} represents the G_{IC} or G_{IIC} obtained by compliance calibration (CC) methods using Beam law. In our opinion, the results from the FE method are more reliable if all constants of the material used are correct. However, the average value doesn't really have a physical sense if the variation of the strain energy release rate along the crack front is too big. If the relative variation parameter defined above as following: $\Delta = (|G_{i-max} - G_{i-av}|) / G_{i-av}$ with $i=I$ or II , Δ is not small enough in our DCB tests. As a result, it is better to consider the maximum value of the strain energy release rate as the fracture toughness in the DCB test. The toughness obtained by experimental CC method is considered as a practical approach. In general, the characterization of mode I and mode II delamination behavior has been well studied, whereas only DCB on unidirectional

specimens is standardized. In this study, the DCB and ENF specimens are obtained from a multidirectional laminate. The variation of G_I in DCB test is quite big as discussed above. As shown in Table. 12, if we compare the maximum value of G_I obtained by the FE method with the toughness obtained by CC method using Beam compliance law, G_{IC-CC} is 2.2% bigger than $G_{IC-FEM-max}$ and G_{IIC-CC} is 15.7% bigger than $G_{IIC-FEM-max}$, respectively. The difference between $G_{C-FEM-max}$ and $G_{C-FEM-av}$ is small.

In general, the values evaluated by VCCT in DCB and ENF tests are smaller than those evaluated by CC method. If the G_{C-FEM} represents the delamination toughness, CC method cannot be accepted strictly because a crack has already propagated before reaching G_{C-CC} .

Mode	Test	$G_{C-FEM-max}$ (N/m)	$G_{C-FEM-av}$ (N/m)	G_{C-CC} (N/m)
I	DCB	450	348	460
II	ENF	790	776	914

Table. 12. Toughness of pure mode I, pure mode II

CHAPTER IV. STUDY OF DELAMINATION UNDER PURE MODE III

IV.1. Pure mode III delamination tests proposed in literature

As mentioned above, in the characterization of the delamination behavior, the participation of mode III remains a complex issue because even the measurement of the toughness under pure mode III is problematic. Before the establishment of a general criterion with the participation of the three modes, this scientific obstacle must be overcome. This is why in this study firstly we have paid our attention on the testing method to evaluate the delamination toughness under pure mode III. At the beginning, some testing methods proposed in the literature have been studied.

IV.1.1. Edge Crack Torsion-1 (ECT-1) test

IV.1.1.1. Experimental

The Edge Crack Torsion-1 (ECT-1) test proposed in literature is schematized by Figure IV. 1 and Figure IV. 2. The specimen is locked at one corner without precrack and loaded on the diagonal corner using a tensile/compression machine while the specimen is supported by other two corners; the crack front is actually loaded under torsion which generates mode III. In this study, the laminate is a multidirectional ones with the stacking sequence described in chapter I (45/0/0/45/0/45/45/0)//crack//(0/45/45/0/45/0/0/45). An axial displacement speed of 2mm/min was imposed until the crack onset.

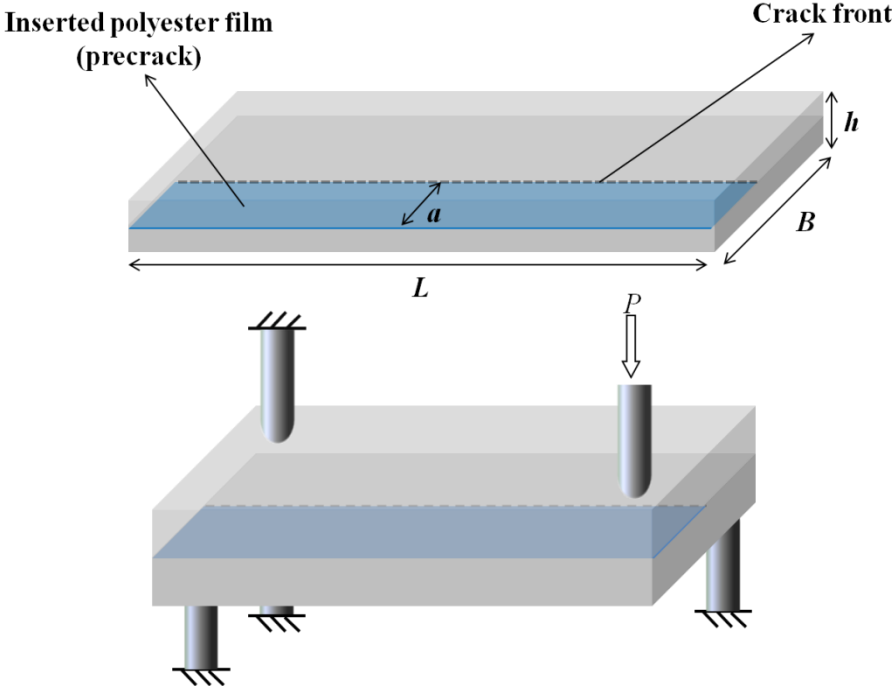


Figure IV. 1. Schematic of ECT-1 test



Figure IV. 2. A picture of ECT-1 test

Eq. 40 ^[38] was applied to calculate G_{IIIc} , where the critical load P_C is corresponding to the load at the end of the linear domain in the load-displacement curve.

$$G_{IIIc} = \frac{mCP_c^2}{2BL\left(1 - m\left(\frac{a}{B}\right)\right)} \quad \text{Eq. 40}$$

, where a , B and L are the specimen dimensions shown in Figure IV. 1. C is the compliance corresponding to a . m and A is obtained by the interpolation method Eq. 41. ^[38]

$$\frac{1}{C} = A\left[1 - m\left(\frac{a}{B}\right)\right] \quad \text{Eq. 41}$$

The dimensions of ECT-1 specimen are listed in Table. 13. Every dimension is measured 3 times at least and the average value is presented in the table.

ECT-1 Test	B (mm)	L (mm)	a (mm)
1-1	44.00	87.00	15
1-2	44.00	87.00	20
1-3	44.00	87.00	25
2-1	44.00	87.00	15
2-2	44.00	87.00	20
2-3	44.00	87.00	25
3-1	44.00	87.00	15
3-2	44.00	87.00	20
3-3	44.00	87.00	25

Table. 13. Dimensions of ECT-1 specimen

IV.1.1.2. Finite element analysis

16 plies were set up for ECT-1 test according to the stacking sequence and were separated symmetrically into two sub-laminates by the crack plane.

The boundary conditions were set according to the real experimental conditions. As shown in Figure IV. 3, the displacement loading curve 4.5mm was imposed at the corner using a ball. The only degree of freedom allowed is in thickness direction. The other balls were all fixed. A surface to surface contact was set between the specimen surface and the balls, as well as between the two sub-laminates of the specimen. There was no other restriction on the specimen plate.

In the model, $a = 20\text{mm}$, $B = 40\text{mm}$ and $L = 90\text{mm}$. The mesh close to the crack front was locally refined according to literature ^[38; 44] to guarantee a good accuracy of the results. The mesh for ECT-1 test is shown in Figure IV. 3.

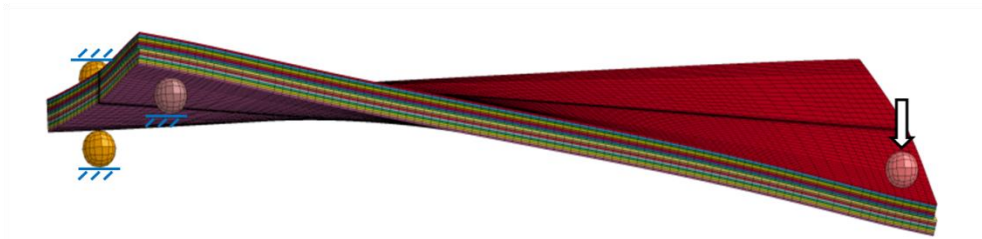


Figure IV. 3. Finite element model of ECT-1 test

IV.1.1.3. Results and discussions

(1) ECT-1

In order to localize experimentally the onset of the crack propagation, ECT-1 tests were stopped right after the first drop of the load value. The value of this load is defined as the critical load, P_C , corresponding to the onset of delamination (Figure IV. 4 (a)). If we define two areas around the crack front: the area a is near the loaded corner and the area b is in the middle (Figure IV. 4 (b)). The image obtained by Omniscan shows that the propagation of the crack began in area a , namely near the loaded corner.

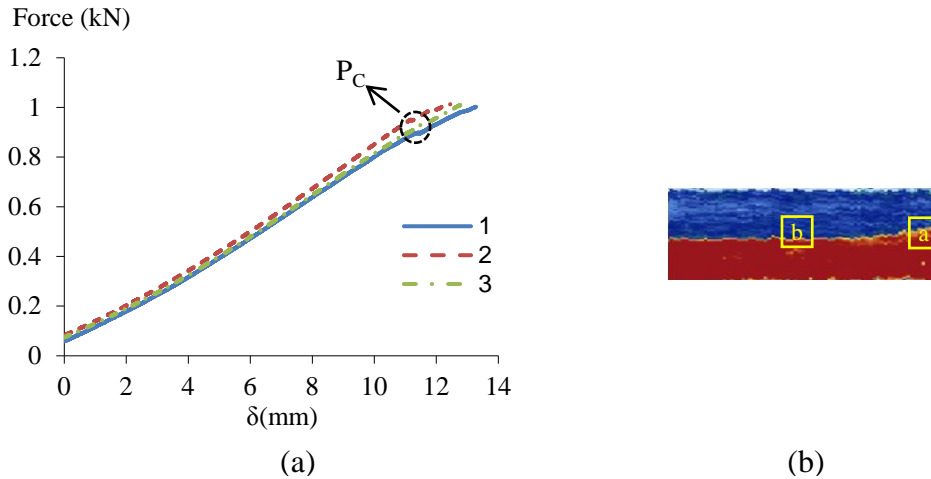


Figure IV. 4. (a) Experimental load-displacement curves; (b) Omniscan image of ECT-I specimen

In order to apply Eq. 40 for the determination of mode III toughness, the compliance calibration (CC) method has to be realized to determine the constant m . A series of tests on the specimens with different initial crack length (Table. 13) were performed to measure their compliances. According to the compliance law (Eq. 42) the interpolation between $1/C$ and a/B is shown in Figure IV. 5, so the constant $m=0.5392$ is obtained.

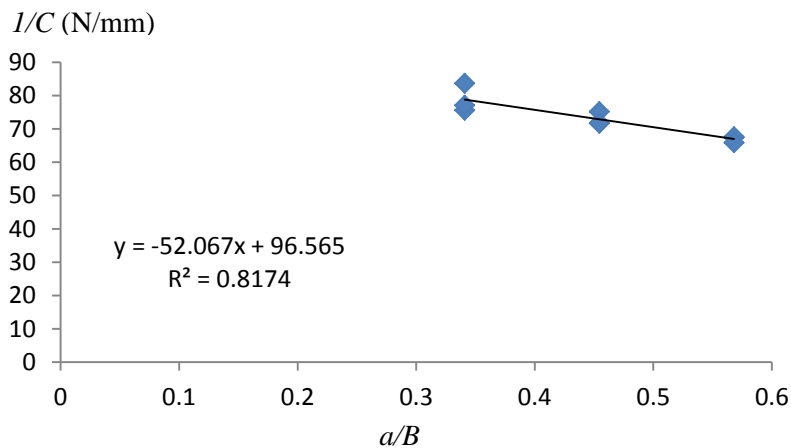


Figure IV. 5. Interpolation between $1/C$ and a/B

The mode III toughness for each specimen determined by Eq. 40 is shown in Table. 14. The standard deviation of the results is small.

Test	G_{III-CC} (N/m)
1	1218
2	1351
3	1362
Average value	1310
Standard deviation	80

Table. 14. G_{III} measured by ECT-I tests

Figure IV. 6 shows the evolution of G_I , G_{II} and G_{III} along the crack front computed at P_C obtained by VCCT from the finite element model. Besides, the average value of G_{III} in Table. 14 is also presented in the same figure, named as G_{III-CC} .

Firstly, G_{III-CC} is about 38.6% higher than the average numerical value $G_{III-FEM}$. Secondly, the evolution of G_{III} is not uniform at all, and the value drops to zero at the extremities ($x/l=0$ and 1), Δ of G_{III} is 38.4%. Herein, the average value is actually not meaningful. However, the maximum value of G_{III} from the finite element model is very close to the one from compliance calibration method. Thirdly, at the extremities of the crack front ($x/l=0$ and 1), mode II component becomes predominant. Moreover at one edge, the mode I component becomes more than 76.7% of G_{IC} measured by DCB test. According to the Omniscan image (Figure IV. 4(b)), the onset of crack growth occurs in the area a ($x/L=1$) where G_{II} becomes important but G_{III} very small, moreover it seems that crack onset occurs under pure mode II or under mixed mode I+II+III instead of pure mode III.

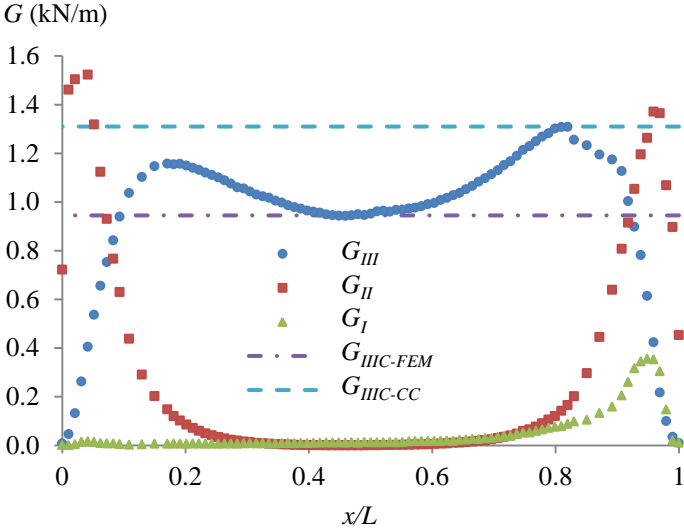
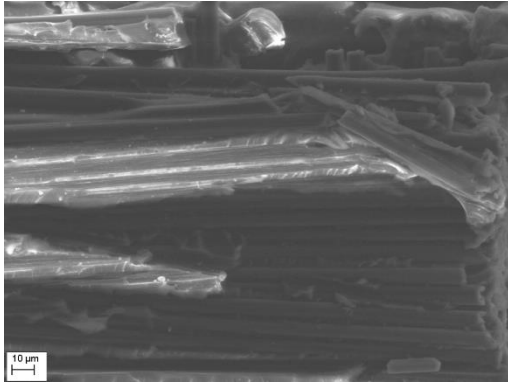
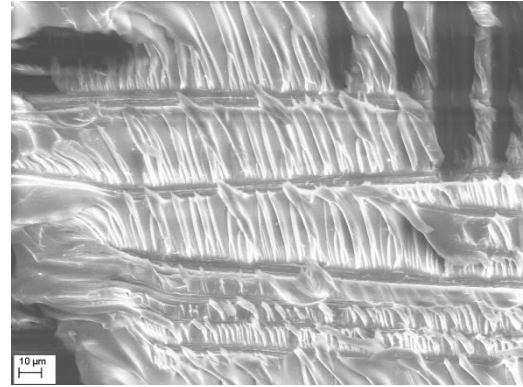


Figure IV. 6. Evolution of G_I , G_{II} and G_{III} along the crack front of ECT-1 test

Observation on fracture surface of ECT-1 specimen by Scanner Electronic Microscope (SEM) is shown in Figure IV. 7. According to the definition of the special areas along the crack front in Figure IV. 4(b), it can be seen that the morphology of the fracture surface in the area a is quite different from the one observed in the area b . It is believed that the former mode must be under mode II or mixed mode II+III while the later one under mode III. That means the measurement of G_{III} with this test is problematic.



(a). Fracture surface in the area a



(b). Fracture surface in the area b

Figure IV. 7. SEM observations in ECT-1 specimen

(2) MECT-1

In literature, the modified Edge Crack torsion (MECT-1) test has proven to have more uniform distribution of G_{III} along the crack front, which is discussed in Chapter II.

A finite element model was established to verify the ability of MECT-1 test, in which the single loading at the corner of the specimen (in Figure IV. 3) is replaced by a pair of loading at two diagonal corners evenly (shown in Figure IV. 8) while all the other parameters were maintained as in ECT-1 test.

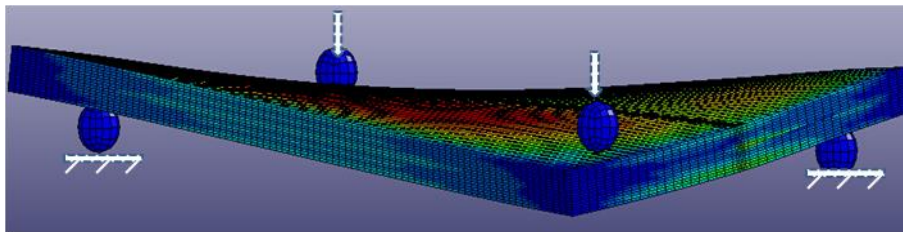


Figure IV. 8. Model of MECT-1 test

Figure IV. 9 shows that the evolution along the crack front of G_I , G_{II} and G_{III} normalized by G_T , where $G_T = G_I + G_{II} + G_{III}$. A significant improvement can be observed in the distribution of the strain energy release rates along the crack front due to the symmetry of the loading conditions. The participation of mode I component is negligible and mode III is nearly constant in the central domain while mode II is the main mode at the two extremities of the crack front. The maximum of G_{III} in the middle area of the crack front is practically the same as the maximum of G_{II} at the two extremities of the crack front. The interest of this test can be described as following:

If $G_{II} < G_{III}$, the onset of delamination should be at the two extremities of the crack front;

If $G_{II} > G_{III}$, the onset of delamination should be at the center area of the crack front;

If $G_{II} = G_{III}$, the onset of delamination should be simultaneous along all crack front.

Unfortunately, we have no enough time to realize this test.

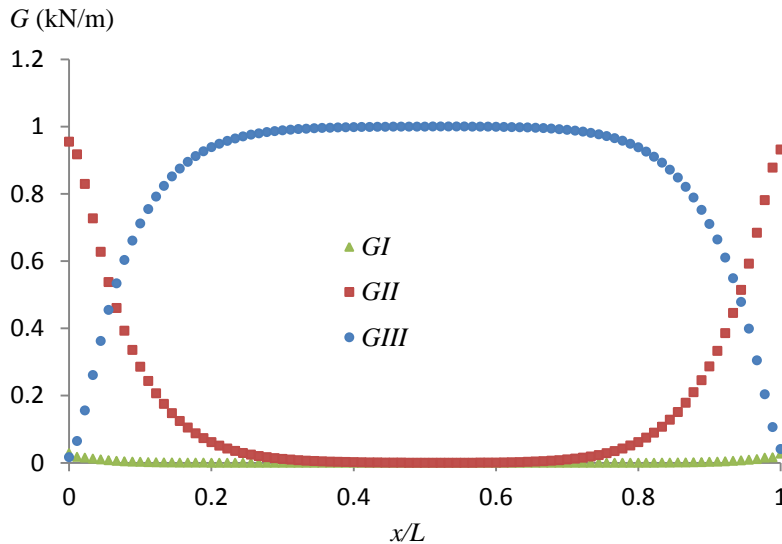


Figure IV. 9. Evolution of G_I , G_{II} and G_{III} normalized by G_T along the crack front in the MECT-1 test

IV.1.1.4. Conclusions

ECT-1 test proposed in literature was performed on a multidirectional composite obtained from a taffetas balanced fabric prepreg. The finite element analysis using VCCT was also carried out in order to investigate the distribution of G_I , G_{II} and G_{III} along the crack front.

For ECT-1 test in this study, the critical strain energy release rate evaluated is probably G_{IIC} instead of G_{IIIc} . That shows the concern regarding ECT-1 test that may identify G_{IIC} instead of G_{IIIc} if the material and the geometry of specimen are not properly chosen. Some care must be taken to avoid errors in mode III delamination tests. Moreover the distribution of G_{III} along the crack front is far from being uniform, which decrease the precision of determination of the delamination toughness if the average value is considered.

MECT-1 was also analyzed by finite element method. This test has a better performance than ECT-1 test in improving the uniformity of G_{III} along the crack front. The evolution of G_{III} is fairly uniform in the middle domain of the crack front while the values of G_{III} approach 0 at the extremities. Moreover, mode II becomes also the principal mode at two extremities, where the maximum of G_{II} is very close to the one of G_{III} in the middle domain. Therefore, this test presents a big advantage: we can not only compare the value of G_{IIC} and G_{IIIc} , but also measure one of them by identifying the area where the delamination initiates.

IV.1.2. Edge Crack Torsion -2 (ECT-2) test

IV.1.2.1. Experimental

The Edge Crack Torsion-2 (ECT-2) test proposed in literature is a real torsion test. So a torsional machine is necessary. In this study, both ends of the ECT-2 specimens were clamped in the jaws of the MTS torsional machine. An axial sliding is permitted during the application of a torque (Figure IV. 10). An axial rotation speed of 0.5 %/min was imposed.

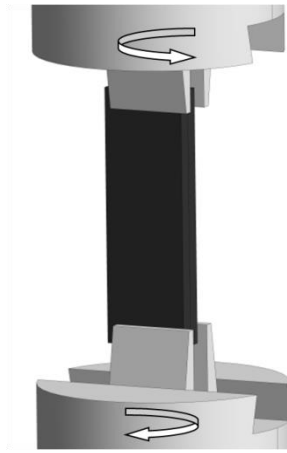


Figure IV. 10. Schema of Edge Crack Torsion-2 test (ECT-2)

An estimation method of the delamination toughness was provided in the work of H. Suemasu^[44], which doesn't perform well for multidirectional laminates. Inspired by the work of R Marat-Mendes and M. de Freitas^[38], we proposed a method with compliance calibration (CC). The critical strain energy release rate was evaluated according to Eq. 42, which is a modified form of Eq. 40^[38]. The compliance law remained the same as Eq. 41. The interpolation of the experimental data between $1/C$ and a/B gives the constant m .

$$G_{IIIc} = \frac{mCT^2}{2BL \left(1 - m \left(\frac{a}{B}\right)\right)} \quad \text{Eq. 42}$$

, where a , B and L are the specimen dimensions shown in Table. 15. C is the compliance corresponding to the crack length a . Note that C in this test is obtained on the experimental torque/rotation angle curve.

ECT-2 test	h (mm)	B (mm)	L (mm)	a (mm)
T10-2	7.00	40.57	145	10
T10-3	7.16	39.99	145.5	10
T15-1	7.05	39.84	144.3	15
T15-3	6.96	40.26	145.7	15
T20-1	7.07	40.66	145.5	20
T20-2	7.02	40.77	146.9	20
T20-3	7.13	40.05	144	20
T25-1	6.94	40.91	143.5	25
T25-2	7.05	40.46	145	25
T25-3	6.94	39.83	146	25

Table. 15. Dimensions of ECT-2 specimens

IV.1.2.2. Finite element analysis

32 plies were set up for ECT-2 test according to the stacking sequence highlighted in Chapter I and they were separated symmetrically into two sub-laminates by the crack plane.

The finite element model for ECT-2 test is shown in Figure IV. 11. The simulation allows optimizing the position of the sample in the jaws in order to obtain the propagation from the pre-crack without propagation at the opposite edge. The crack was actually located close to the rotation axis as shown in Figure IV. 12. In order to impose the torsion, a rotation curve 0.44rad was employed on the outermost face of one jaw while the other one was fixed. A surface to surface contact was set between the specimen surface and the jaws, as well as between the two sub-laminates of the specimen. There was no prestressing force between the jaws and the specimen. Moreover, the two points at the edge of the specimen along the loading axis were restricted. At the loading side, an axial displacement is permitted. In the fixed jaw, the point is fixed as well.

The mesh close to the crack front was locally refined according to literature [38; 44] to guarantee a good accuracy of the results.

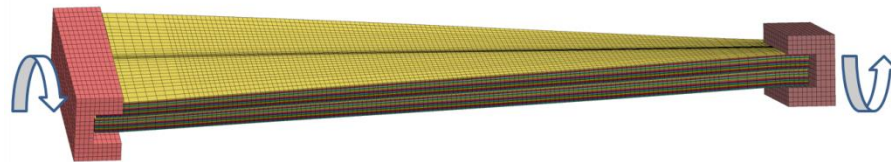


Figure IV. 11. Model of ECT-2 test

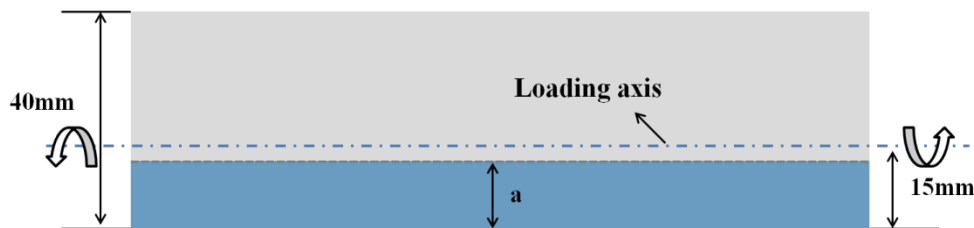


Figure IV. 12. Schematic of ECT-2 test

IV.1.2.3. Results and discussions

Figure IV. 13(a) gives experimental curves of the ECT-2 test. Herein, the repeatability with three specimens is relatively good, but the critical load corresponding to the onset of crack growth is not easy to define. We try to define an appropriate critical torque T_C in different ways. Three values of G_{IIIc} were calculated according to different definitions of T_C (Figure IV. 13(b)): T_{C-1} is the torque at the end of the linear domain; T_{C-2} the torque at the intersection of the curve and a line at 90% of initial slope of the linear domain; T_{C-3} the torque at first visible drop of the torque value.

Firstly, one of the three tests was stopped and scanned right after the first drop of torque (T_{C-3}), shown in Figure IV. 13(c). Not only the propagation at the pre-crack was observed, but also a little propagation at the opposite edge, where the expression proposed for the determination of G_{IIIc} is no longer available. It seems that the onset of crack happens before reaching T_{C-3} . The critical torque is believed to be between T_{C-1} and T_{C-2} . Similar conclusions were gained in the work of Marat-Mendes R. [38].

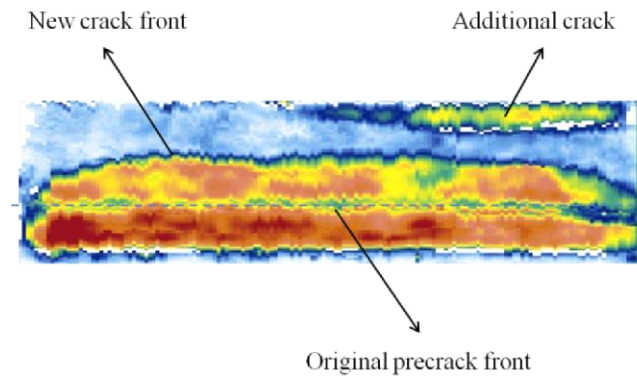
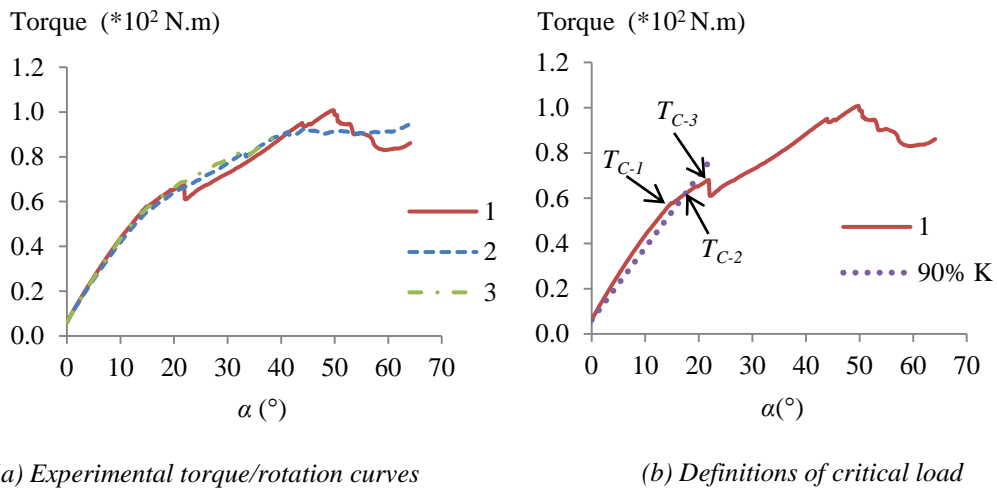


Figure IV. 13. Experimental torque/rotation curves and Omniscan image of ECT-2 test

A series of tests on the specimens with different initial crack length (Table. 15) were performed to measure the compliance. According to the compliance law (Eq. 41) the interpolation between $1/C$ and a/B is shown in Figure IV. 14, so the constant $m=0.5430$ is obtained.

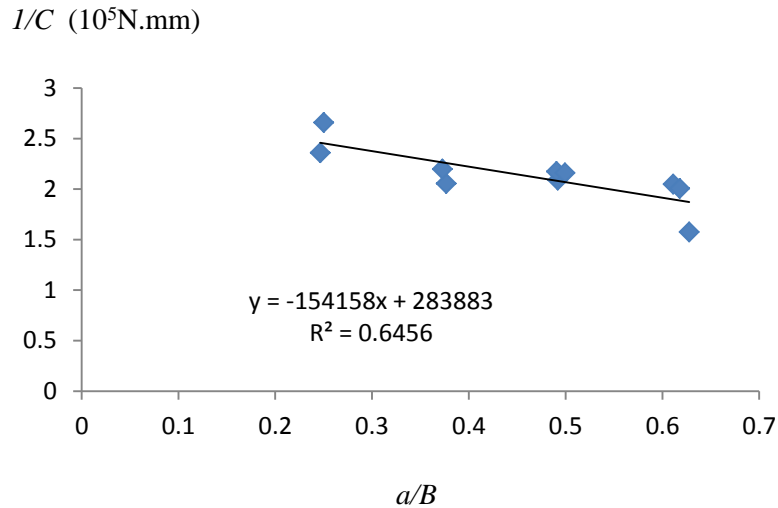


Figure IV. 14. Interpolation of $(1/C)$ vs (a/B) (Eq. 41)

The results calculated by Eq. 42 are compared in the Figure IV. 15. It is seen that the values of G_{III} measured on the specimens with different initial crack lengths (10 mm, 15 mm, 20 mm, 25 mm) are very close to each other if T_{C-1} or T_{C-2} are considered as the critical load while the difference becomes too large if T_{C-3} is used. Actually, these G_{III} do not correspond to the onset of crack growth, but to first instable crack propagation. In summary, it is more possible to consider T_{C-1} or T_{C-2} as critical load. In the next part, only T_{C-2} is used to determine G_{III} , also because it is easier to measure experimentally.

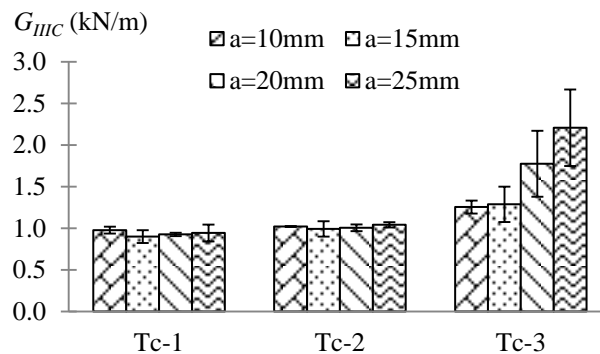


Figure IV. 15. Comparison of G_{III} results from ECT-2 test

The simulation of ECT-2 test was performed on the specimen with initial crack length 20mm. The evolution of G_I , G_{II} and G_{III} along the crack front computed at T_{C-2} is illustrated in Figure IV. 16. The average value of G_{III} from all the tests with specimen $a=20$ mm obtained by Eq. 42, named G_{III-CC} , are also presented in the Figure IV. 16.

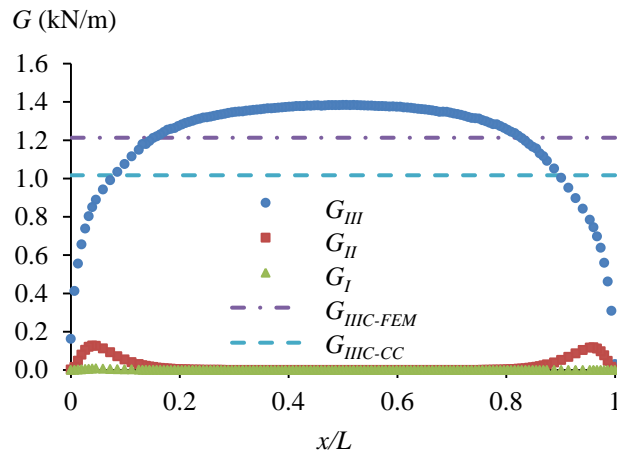


Figure IV. 16. Evolution of G_I , G_{II} and G_{III} along the crack front of ECT-2 specimen

It is shown firstly that the uniformity of G_{III} is better in ECT-2 test than in ECT-1 test, but the values of G_{III} also drop to almost zero at the extremities of the crack front while the variation of G_{III} in the middle domain along the crack front is much less significant. Δ is approximately 14.0%. Secondly, G_I is negligible and G_{II} is much smaller than in ECT-1 and MECT-1 tests. Thirdly, the G_{III-CC} calculated according to Eq. 42 is 16.2% smaller than $G_{III-FEM}$. Recall that in the ECT-1 tests, the G_{III-CC} calculated according to Eq. 42 is always higher than $G_{III-FEM}$, no explanation can be given for this inverted result.

IV.1.2.4. Conclusions

In ECT-2 test, there is much less participation of G_I and G_{II} components than in ECT-1 test. Δ is big when the whole crack front is taken into consideration because the values of G_{III} drop dramatically at the edges. However, the critical load corresponding to the onset of crack growth is not easy to define. The values of G_{III} drop to almost zero at the extremities of the crack front. In addition, the $G_{III-FEM}$ becomes 16.2% higher than the G_{III-CC} . If the maximum of G_{III} is considered, the difference between $G_{III-FEM-max}$ and G_{III-CC} is more important, the former is about 26.5% higher than the later. Besides, the loading condition has to be optimized to ensure crack propagation in the desired area.

IV.2. Edge Ring Crack Torsion (ERCT or ERC-III) test

IV.2.1. Introduction

It is seen that the participation of mode II component in all the ECT tests can never be totally eliminated. The variation of G_{III} along the crack front is too big to be negligible. Generally, this variation is slighter in the central domain of the crack front, but much more significant at the extremities of the crack front. Values of G_{III} can go to almost zero at the extremities.

An original pure mode III test was proposed in previous work in our laboratory, named Edge Ring Crack Torsion (ERCT or ERC-III) test. This is a torsion test on a composite plate including an edge ring delamination crack between two sub-laminates. The loading mode obtained is pure mode III, and the crack front is circular, so closed without edges (that means without the extremities of the crack front). The edge effect in ECT specimens mentioned

above is therefore eliminated. Moreover the variation of G_{III} along the crack front can be reduced by optimizing different parameters of the specimen and the testing device.

IV.2.2. Experimental

Figure IV. 17 shows the schema of ERCT specimen. A pre-crack with a central circular front is created between two sub-laminates by inserting a 13 μm thick polyester film. A central disc is cut out of the inserted polyester film with the help of a circle cutter. So the circular hole is non-delaminated area while the blue film presents an Edge Notched Crack.

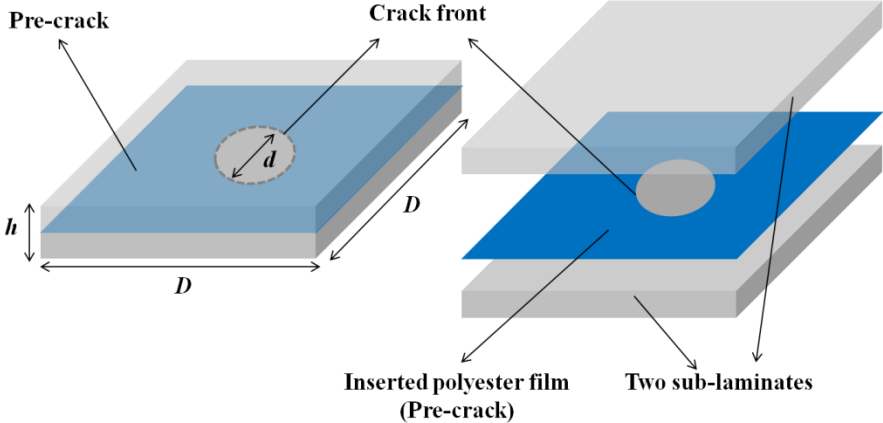


Figure IV. 17. Schema of ERCT specimen

Even though the shape of the specimen and the insert film is square, the rotational displacement is imposed through a ring glued onto the surfaces of the laminate (Figure IV. 18 and Figure IV. 19), so “edge ring crack” is named.

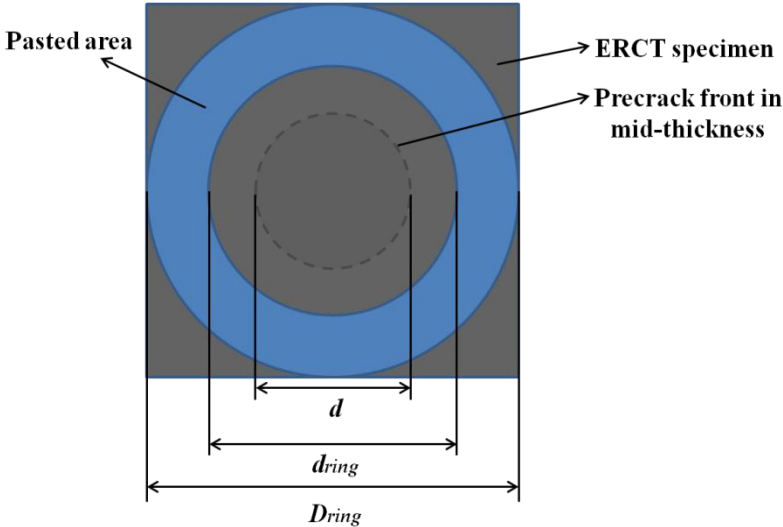


Figure IV. 18. Definition of d , d_{ring} and D_{ring}

Firstly, the composite specimen was pasted to the ring protruding from two rigid plates shown in Figure IV. 19. The inner d_{ring} and outer diameter D_{ring} of the ring are 80mm and 120mm respectively, shown in Figure IV. 18 and Figure IV. 19. Two diameters d (30mm and 50 mm)

of the central circle (non-delaminated area) were used while D (120mm), h (7mm) was kept the same. At least 3 specimens were tested for each kind.

The rigid plates were designed with a hole shown in Figure IV. 19. This design allows observing the effect of fiber orientation on the delamination resistance in pure mode III.

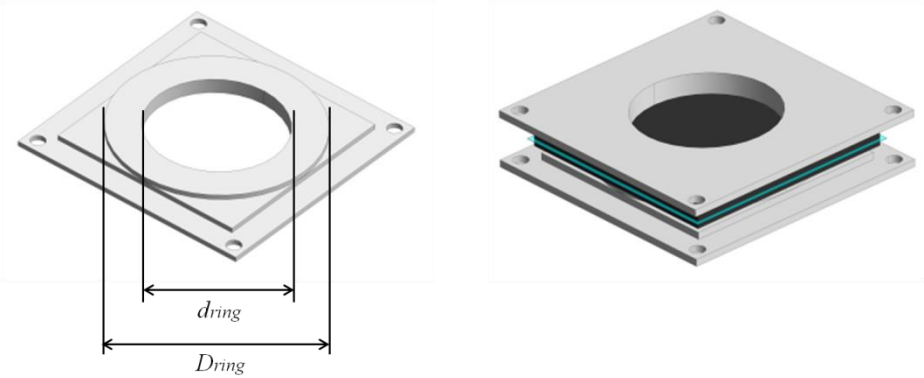


Figure IV. 19. Rigid plates in the device of ERCT

Figure IV. 20 shows the ERCT device and Figure IV. 21 gives a picture of ERCT test. Great care was taken in order to locate the center of the sample on the axes of the rigid plates during the pasting process. And then the rigid plates were screwed to the torsion device. Finally, the torsion device was submitted to an imposed rotation up to the crack propagation. Thanks to the d_{ring} diameter holes in the rigid plates, it's also possible to observe the crack propagation by Ultrasonic C-scan.

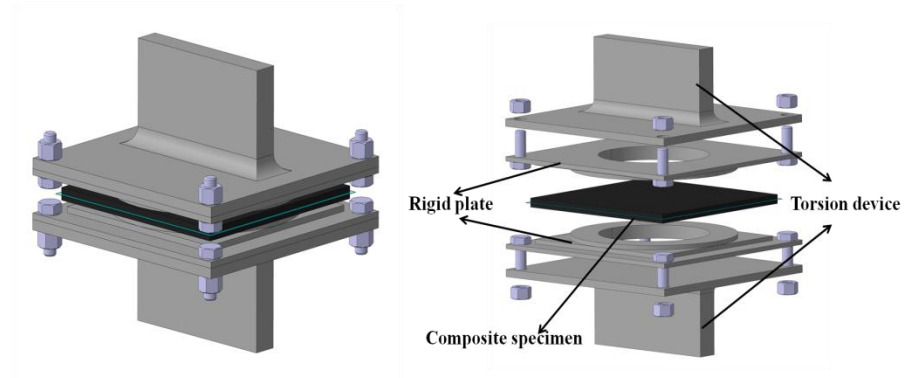


Figure IV. 20. Schema of ERCT device



Figure IV. 21. A picture of ERCT test

In order to propose a closed-form expression for determining G_{IIIc} , we started from the case of a cylinder of diameter D with an external crack of diameter d submitted to a torque T . The stress intensity factor K_{III} is given by a semi analytical expression Eq. 43 from Tada Handbook ^[75] developed for a metal cylinder with an external circular notch, shown in Figure IV. 22.

$$K_{III} = \frac{16T}{\pi d^3} \sqrt{\pi \frac{(D-d)}{2}} \cdot f\left(\frac{d}{D}\right) \quad \text{Eq. 43}$$

$$\text{with } f\left(\frac{d}{D}\right) = \frac{3}{8} \sqrt{\frac{d}{D}} \cdot \left[1 + \frac{1}{2} \frac{d}{D} + \frac{3}{8} \left(\frac{d}{D}\right)^2 + \frac{5}{16} \left(\frac{d}{D}\right)^3 + \frac{35}{128} \left(\frac{d}{D}\right)^4 + 0,208 \left(\frac{d}{D}\right)^5 \right]$$

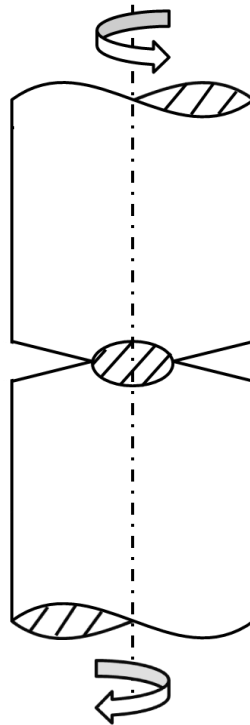


Figure IV. 22. Cylindrical beam with a ring crack

In fracture mechanics, K_{III} is related to strain energy release rate G_{III} by Eq. 44 for isotropic materials if the crack growth is in its initial plane (self-similar manner), where G is the shear modulus of the isotropic material.

$$G_{III} = \frac{1}{2G} K_{III}^2 \tag{Eq. 44}$$

Even though the crack in ERCT specimens is embedded into two plates in laminated composite instead of an isotropic cylinder, we want to know whether this closed-form formula can be applied for determining G_{III} in the case of ERCT test and whether the function f needs to be adapted to the ERCT test.

IV.2.3. Finite element analysis

32 plies were set up for ERCT test according to the stacking sequence highlighted in Chapter I and they were separated symmetrically into two sub-laminates by the crack plane. The steel device and bondline were also simulated. Then two kinds of model were established. For the first model, spring elements were arranged along the crack front in order to obtain loads at the crack front and then to determine the evolution of G_I , G_{II} and G_{III} along the crack front using VCCT.

For the second model, cohesive elements were arranged at the non-delaminated area and there was no spring element along the crack front. The model aims at verifying the onset of crack growth. A bilinear Traction-Separation-Load-Curve (TSLC) was applied according to literature [17]. The parameters of the cohesive element material model are shown in Table. 16.

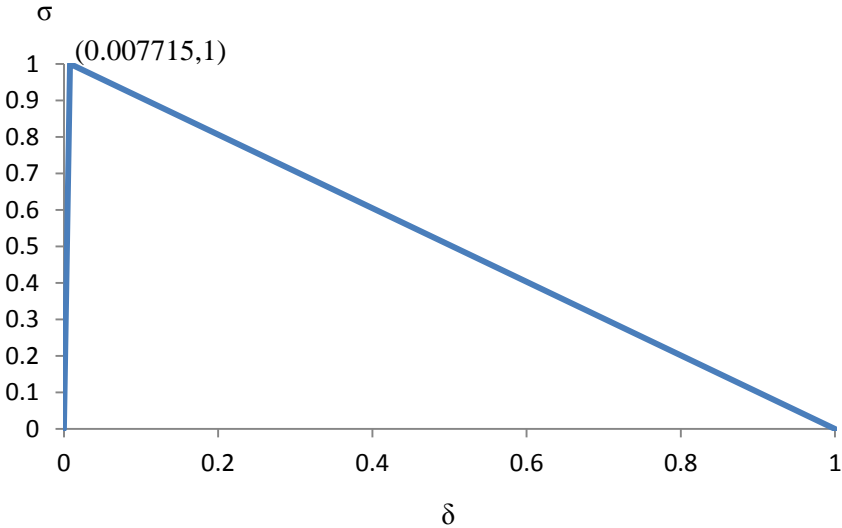


Figure IV. 23. Bilinear TSLC law used in cohesive element model

G_{IC}	460 (N/m)
G_{IIC}	980 (N/m)
Peak traction in normal direction	45 N
Peak traction in tangential direction	65 N

Table. 16. Parameters of cohesive element material model

The mesh close to the crack front was locally refined (Figure IV. 24) to guarantee a good accuracy of the results. Mesh refinement has been studied. It demonstrates that the difference on G_i ($i=I, II, III$) calculated by VCCT between the model with the current mesh and that with twice elements in the plate plane (r, θ) near the crack front is about 1%. Concerning the thickness direction z , a model with two elements in the thickness of each ply of the plate has been tested on a simplified model loaded in torsion and leads to 2.7% of variation. But the quality of the finite element is degraded by refining the mesh in the z direction, because its dimension in z is too small compared to those in r and θ directions.

Actually, the finite element model was also validated by comparison of the calculated G_{III} using VCCT and Tada formula, which are obtained from an isotropic cylinder model. The difference is less than 2%. Herein, the isotropic cylinder is in steel with length of 2x50 mm and diameter of 120 mm. An edge ring crack is located at the mid-length, whose non cracked area has diameter of 30 mm. It is interesting to note that the cylinder simulated here is not really an infinite cylinder, but Tada’s formula seems to be a good approach for an isotropic material.

The FE model of ERCT test is shown in Figure IV. 25, θ where is defined in a polar coordinate. In order to impose a torque on the specimen, a rotation curve 0.005 was employed on both of the loading heads as shown in Figure IV. 25. The central point of the specimen was fixed while the loading axis was permitted to move only in the axis direction.

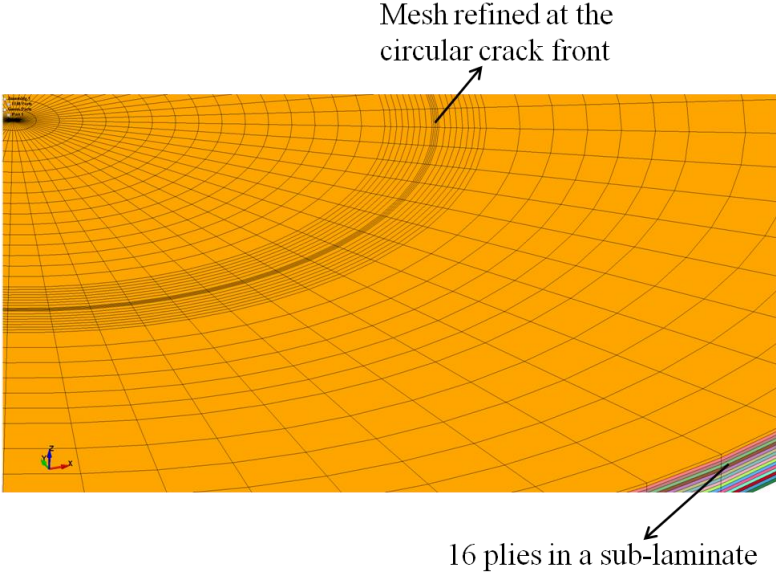


Figure IV. 24. Mesh of ERCT specimen

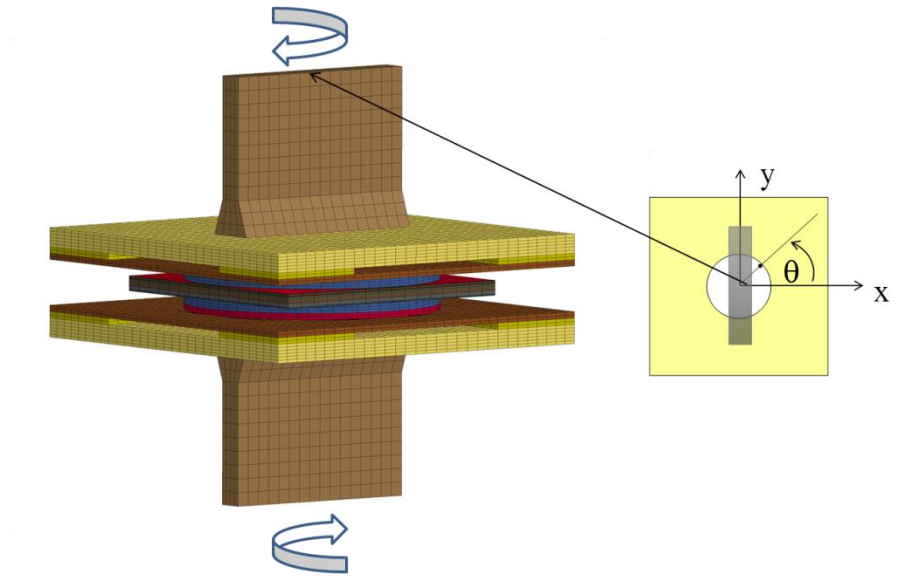


Figure IV. 25. Model of ERCT test

IV.2.4. Results and discussions

In ERCT test, the crack growth occurs always in an unstable manner towards the center (non-delaminated area). Figure IV. 26 shows the experimental torque/rotation curves, where a sudden drop in the torque is observed. The peak of the load is almost at the end of the linear part. That results in an easy definition of the critical load corresponding to the crack growth onset. At that moment, the test was stopped and then the specimen was scanned by Ultrasonic C-scan in order to verify the crack propagation. Figure IV. 27 shows the images obtained by Ultrasonic C-scan on the three tested specimens with $d=30$ mm before and after crack growth, where the white zone presents non-delaminated area. It demonstrates that the crack propagated indeed. Moreover, it seems that the crack propagated much more along an angle θ_C close to $(\pm 45^\circ)$. One explanation may be that the crack resistance varies as a function of the adjacent fiber orientations, and the resistance of the crack tips at θ_C is smaller under shear mode. We can also imagine that the penetration of air or/and water into the delaminated areas after the test depends on their fracture modes and damage level. In any case, the interpretation of the images obtained from Ultrasonic C-scan requires further study.

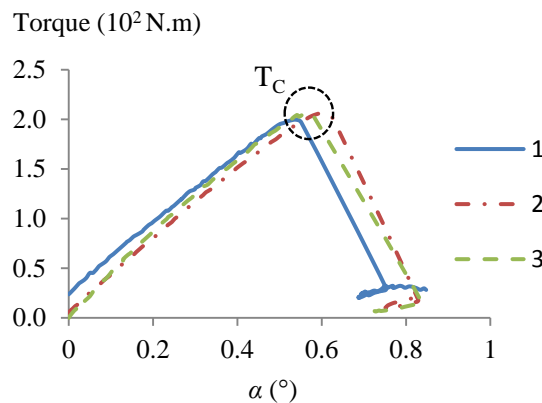


Figure IV. 26. Experimental torque-rotation curves of ERCT specimen with $d=30$ mm

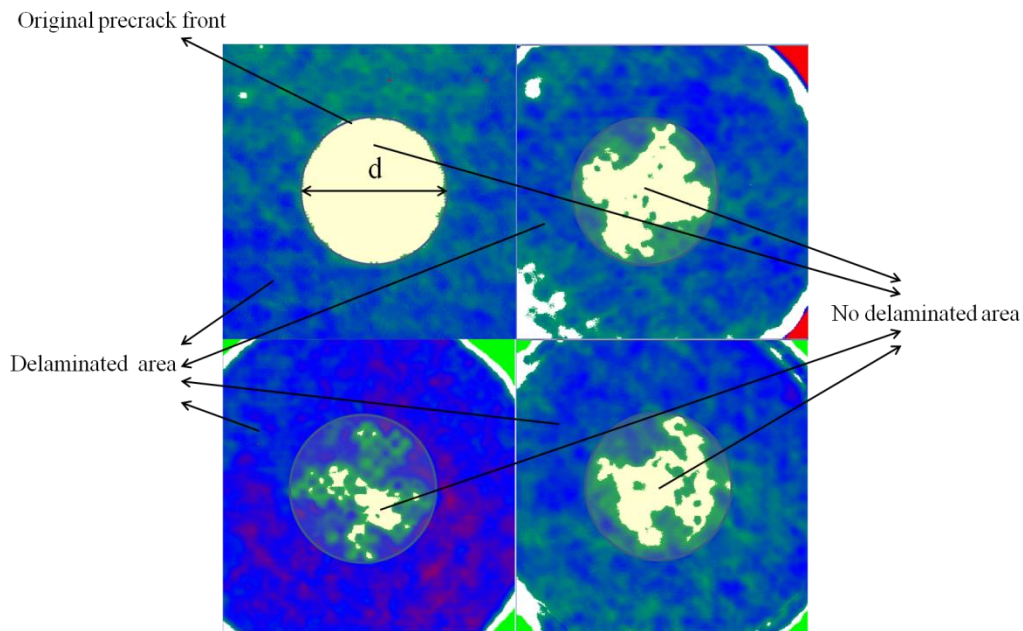


Figure IV. 27. Ultrasonic C-scan image before and after propagation on the three ERCT specimens with $d=30\text{mm}$

The results of G_{IIIc} according to Eq. 43 and Eq. 44 are listed in Table. 17. Note that G in the Table. 17 should be $G_{z\theta}$ for a laminate, which generally vary as a function of θ . In order to make it clearer, a schematic of fiber orientation and crack front is shown in Figure IV. 28. However, the tested laminates are quasi-isotropic in our case. So $G_{z\theta}$ is constant and $G_{z\theta} = G_{I3}$ according to the analysis by J.M. Berthelot^[76].

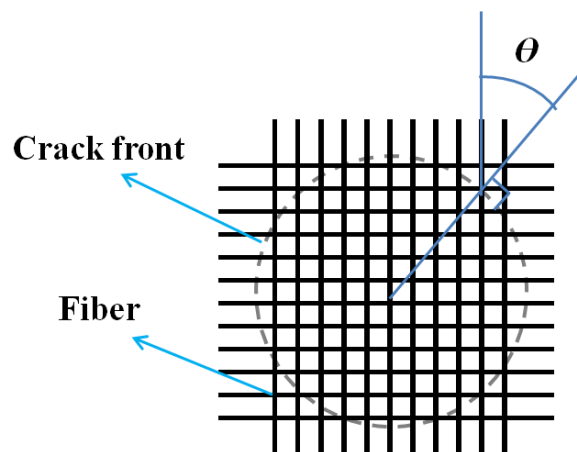


Figure IV. 28. Definition of angle θ between fiber orientation and crack front

The repeatability of ERCT in term of critical load is good compared to the ECT tests. The deviation of G_{IIIc} is small. It also shows little influence of the crack diameter on G_{IIIc} . Additionally, the values of G_{IIIc} obtained by Tada formula (Eq. 43), named $G_{IIIc-Tada}$, were in a reasonable range, which are compared with $G_{IIIc-FEM}$ also in Figure IV. 29 and Figure IV. 30.

d (mm)	T_{C-av} (N.m)	G (MPa)	K_{III} (MPa.m ^{1/2})	$G_{III-C-Tada}$ (N/m)
30	204±4	5400	3.13±0.06	910±34
50	742±3	5400	3.17±0.02	932±11

Table. 17. G_{III} obtained from Tada's formula for ERCT tests

The curves presented in Figure IV. 29 and Figure IV. 30 illustrate the evolution of G_I , G_{II} and G_{III} along the crack front obtained by finite element method at the critical torque T_C . It is interesting to note that the participations of mode I and mode II are almost zero, which demonstrates that the crack is loaded in pure mode III indeed. The values of G_{III} show a periodic variation instead of being constant, which can be minimized by optimization, however. In fact, the evolution of G_{III} along the crack front results from different influence factors. Actually it depends not only on the geometry of the device used for applying the torque, which is not strictly axisymmetrical, but also on the composite specimens, especially on the adjacent fiber orientation relative to local crack front. The ratio of d/D_{ring} is also a parameter that determines the importance of the effects mentioned above. Δ is about 7.5% for the specimens with $d=30$ mm and 17.4% for those with $d=50$ mm. Moreover, the maximum G_{III} is localized at $\theta=0^\circ$ and 180° , so the propagation of the crack should initiate at these angles if the toughness in pure mode III was independent of adjacent fiber orientation.

It is shown also that for the specimen with $d = 30$ mm, the $G_{III-C-Tada}$ value agrees well with $G_{III-FEM}$. The difference between $G_{III-C-Tada}$ and $G_{III-FEM}$ measured on the specimens with $d=30$ mm is only approximately 2.2%; this difference is more significant measured on those with $d=50$ mm, which is approximately 20.5%. It seems that if the variation of G_{III} along the crack front is large, the closed-form proposed by Tada would no longer be applicable.

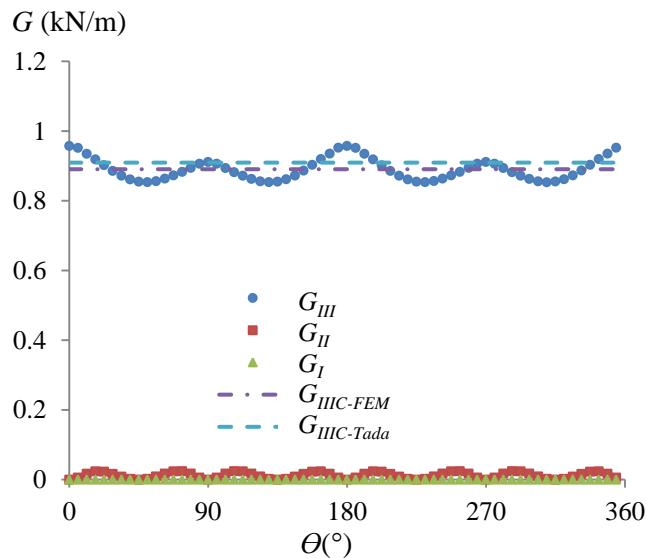


Figure IV. 29. Evolution of G_I , G_{II} and G_{III} along the circular crack front of ERCT specimen with $d=30$ mm

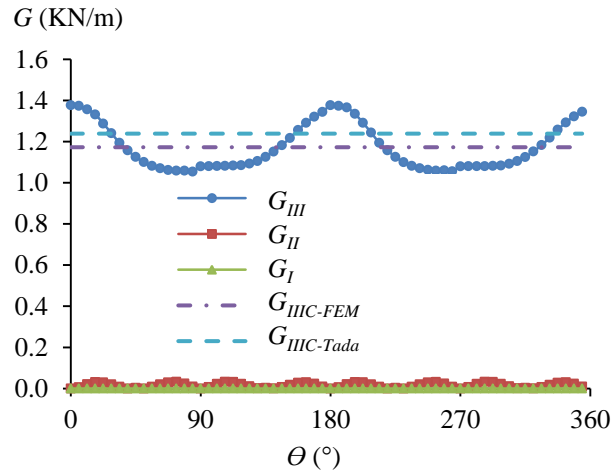


Figure IV. 30. Evolution of G_I , G_{II} and G_{III} along the circular crack front of ERCT specimen with $d=50\text{mm}$

Moreover, the results of cohesive element model of ERCT test show that the onset of damage will occur for $\theta=0^\circ$ or 180° (Figure IV. 31), where the cohesive element are damaged and removed. It corresponds to the fact that G_{III} reaches the maximum value at $\theta=0^\circ$ or 180° shown in Figure IV. 29 and Figure IV. 30. It confirms the conclusion that the propagation of the crack should initiate at 0° and 180° if the toughness of the composite is not influenced by the fiber orientation.

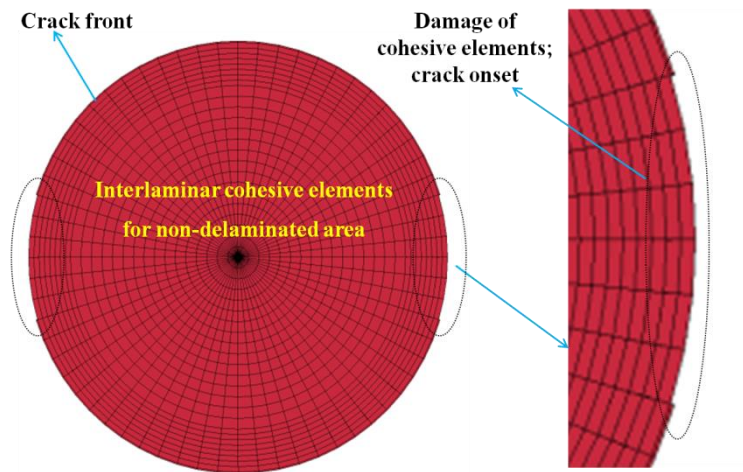


Figure IV. 31: Cohesive element model for ERCT specimen

IV.2.5. Conclusions

After the review of the development of pure mode III testing methods, it is found that most of the tests proposed in the literature cannot eliminate totally the participation of mode II, and the distribution of G_{III} along the crack front is not uniform. As a result, the determination of G_{IIIc} should be improved.

In this section, the novel test ERCT was performed on a quasi-homogeneous and quasi-isotropic multidirectional laminate obtained from a woven balanced carbon/epoxy taffeta

pregreg. These tests were also simulated by the finite element method to investigate the evolution of G_I , G_{II} and G_{III} along the crack front.

The most significant advantages of ERCT test are:

- the fracture mode is pure mode III without the participation of mode I or mode II components;
- Δ along the crack front is much smaller than ECT tests; it can be less than 7.6% by optimizing the geometry of the specimen. So it's acceptable to consider the average value as the material toughness;
- the critical load corresponding to the crack onset is easy to define;
- the agreement between $G_{III-C-Tada}$ and $G_{III-C-FEM}$ is good for a specimen with a small diameter d .

Some inconveniences should be discussed:

- the coincidence of axes and the relative position between the crack front and the axis are significant. The gluing process and installation of the devices may introduce errors.
- Preparing the specimen and curing the glue may take about 1 hour.
- The rigid plates are recycled in this test and the bondlines have to be cleaned by acetone every time.

It is interesting to note that the angle Θ between the crack front and the fiber orientation, as shown in Figure IV. 28, varies regularly, which is different from all the traditional pure mode tests. The delamination resistance may also vary along with Θ . In this case, the delamination toughness evaluated by Tada formula presents the smallest value, which is also meaningful.

Moreover, it is better to propose new testing methods by using Edge Ring Crack specimen in order to compare three pure mode delamination tests without interference caused by Θ .

In conclusion, ERCT test is a promising pure mode III testing method for measuring G_{III-C} . It maybe presents better results than most tests in the literature in terms of two aspects: the elimination of mode I and II components and the reduction of G_{III} variation along the crack front. However, further improvement of the ERCT test is still possible based on: the study of the factors affecting the evolution of G_{III} along the crack front; the sensitivity study to experimental defaults; the development of a closed-form expression more adequate for determining G_{III-C} and the improvement of the testing device.

IV.3. Factors affecting the evolution of G_{III} along the crack front of ERCT test

In this section, the factors affecting the evolution of strain energy release rate is analyzed and discussed. A polar coordinate system (r, Θ) is employed in order to show evolution of G_{III} normalized by average value. Mode I and mode II components are always shown to be negligible with all the models so that they are not presented. Three influence factors are discussed in terms of device geometry, laminate geometry and relative ratio d/D_{ring} . Moreover, an ERCT model with steel specimen is established by replacing composite material model by steel material model and keeping all the other parameters.

IV.3.1. Influence factor from the device

First of all, the original ERCT (device A) and a modified version device C are established (shown in Figure IV. 32) in order to study the influence of device geometry on the evolution of G_{III} , which is called as device factor for short. For the device C, the loading head is replaced by a cylinder of the same height and the square steel plate is replaced by a round one with a diameter 120mm, equal to the side length of the square plate. Note that the pasted ring still remains the same in the device C with inner and outer diameters 80mm and 120mm respectively. Device A has two planes of symmetry: XOZ and YOZ while device C is totally axisymmetrical. The specimens for A and C are set as same isotropic steel in order to avoid disturbing from the material of specimen.

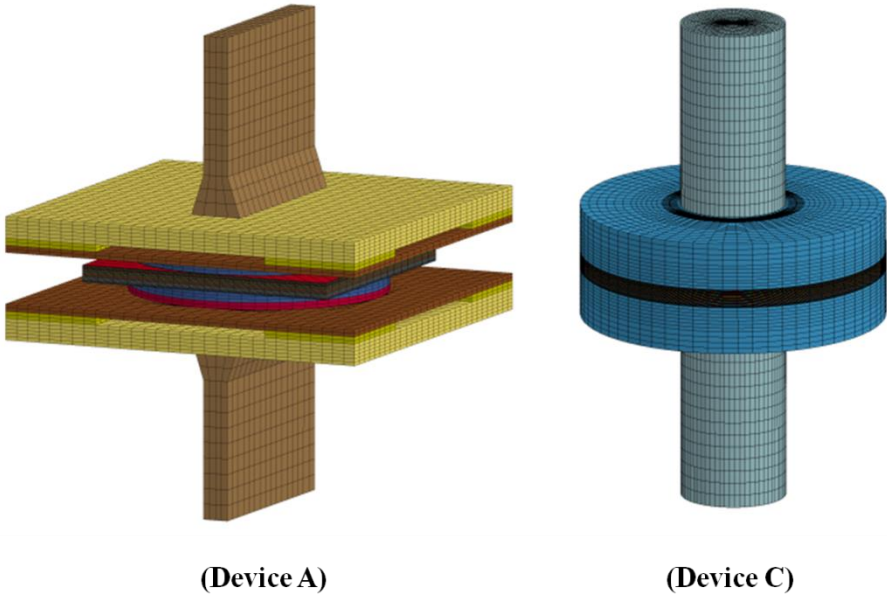


Figure IV. 32. Finite element models of device A and C

Figure IV. 33 shows the evolution of normalized G_{III} along the circular crack front for test A and C. The values of G_{III} are constant for test C, shown as the curve C_steel_d50. For test A, the evolution has two symmetry planes at 0° and 90° . And the values of G_{III} in curve A_steel_d50 increase approaching 0° and decrease approaching 90° . In general, the evolution corresponds to the change of the position of the loading head, namely the change of the angle between loading head and local crack front, shown in Figure IV. 34. It demonstrates that the evolution is caused by the shape of the loading head and the angle between the loading head and local crack front.

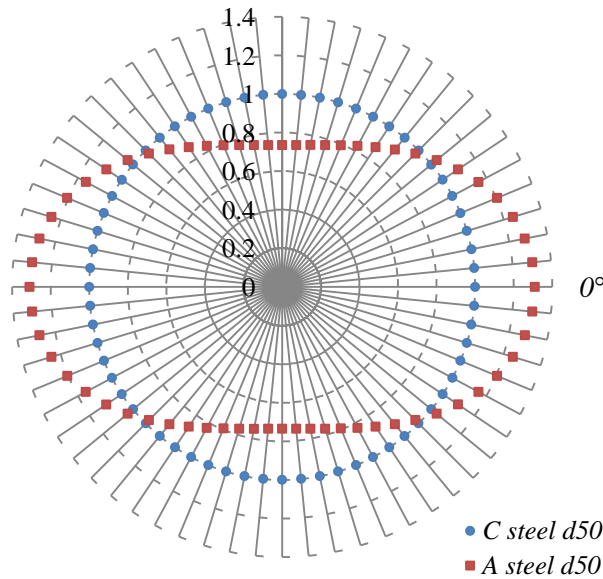


Figure IV. 33. Evolution of normalized G_{III} along the circular crack front with device A and C

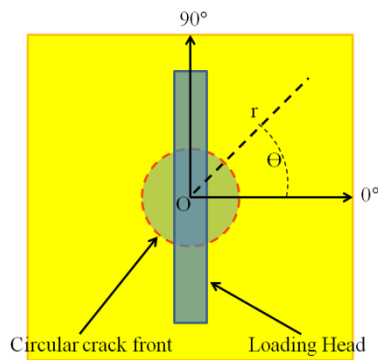


Figure IV. 34. Top view of ERCT device

IV.3.2. Influence factor due to the nature of the laminate

All the influence from the composite material is named laminate factor for short. Firstly, a model of device C with composite specimen is established. In this specimen, the laminate stiffness matrix A, B, D maintain the same in all directions because the specimen is quasi-isotropic; the laminate tested is also quasi-homogeneous, which means the same elastic stiffness properties in tension and in bending in all direction.

The evolution of G_{III} along the circular crack front with steel and composite specimens using device C is shown in Figure IV. 35. The laminate factor has a small influence on the evolution, with Δ less than 3%. The values of G_{III} increase approaching 0° and 90° while they decrease approaching $\pm 45^\circ$. It is believed that the tiny variation results from the influence of the fiber orientations adjacent to the precrack plane.

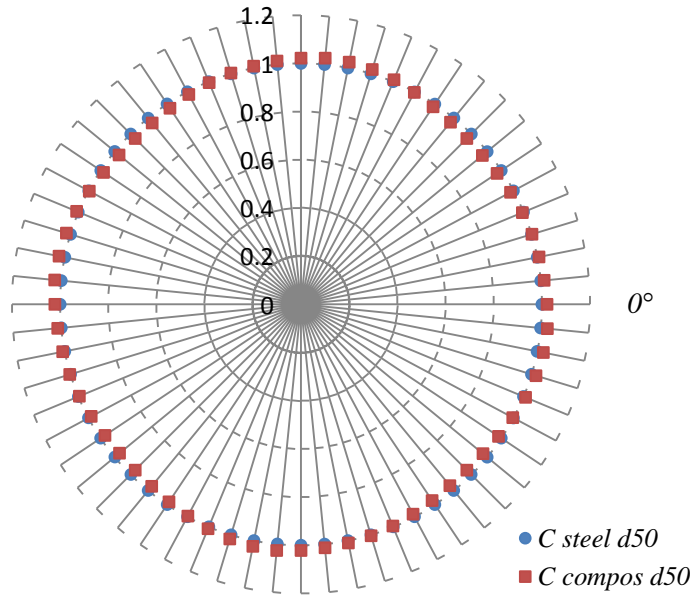


Figure IV. 35. Evolution of normalized G_{III} along the circular crack front with device C and steel and composite specimens

IV.3.3. Influence factor due to ratio d/D_{ring}

Influence factor of ratio between the non-delaminated area diameter and delaminated area diameter is characterized by a ratio d/D_{ring} . d is the diameter of non-delaminated area, namely the diameter of circular crack front and D_{ring} is the outer diameter of the bondline (corresponding to the pasted ring), as shown in Figure IV. 18. The torsional load is transferred by the bondline so that D_{ring} is considered as the edge of the crack.

Firstly, two specimens in steel using device A were analyzed numerically which are distinguished only by changing d . “A-steel-d30” and “A-steel-d50” denote the results for the specimen with $d=30\text{mm}$ and for that $d=50\text{mm}$, respectively. As shown in Figure IV. 36, the value of G_{III} from the results A-steel-d50 increases significantly approaching 0° and decrease approaching 90° . The same tendency on the variation of G_{III} is also observed on the results from A-steel-d30, but the amplitude of this variation is smaller than that from A-steel-d50. It demonstrates that ratio d/D_{ring} has an important influence on the distribution of G_{III} along the crack front. Moreover, the ratio d/D_{ring} has an influence on the device factor. A positive correlation is found between the device factor and ratio d/D_{ring} in a certain range.

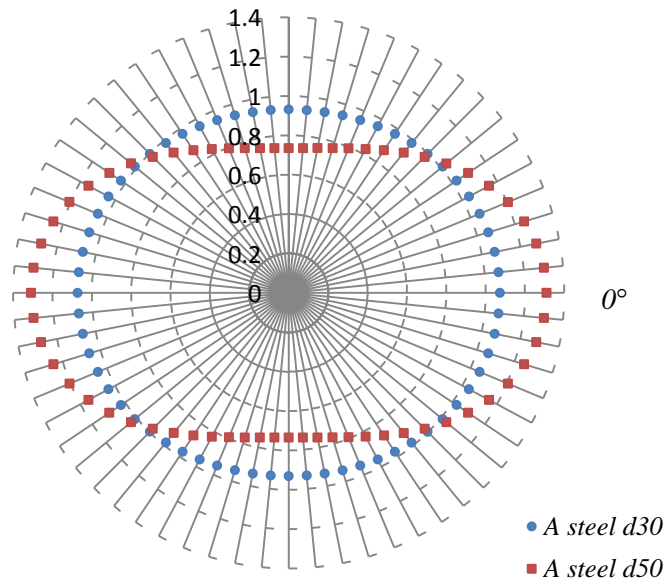


Figure IV. 36. Evolution of normalized G_{III} along the circular crack front with device A and different diameters of steel specimens

And then numerical model for five composite specimens using device C are established, each specimen has different d (30, 40, 50, 60 and 75mm). All results, named by “C-compos-d30”~“C-compos-d75”, are presented in Figure IV. 37. A negative correlation is found between the laminate factor and ratio d/D_{ring} in a certain range.

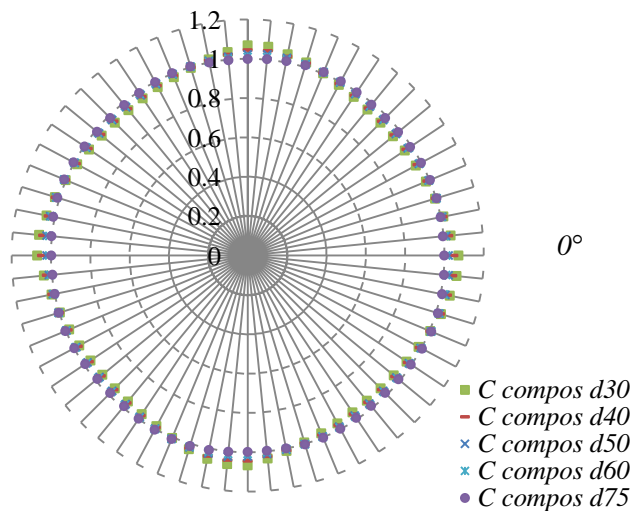


Figure IV. 37. Evolution of normalized G_{III} along the circular crack front with device C and different diameters of composite specimens

It is seen that the level of the variation of G_{III} in term of $\Delta = (|G_{III-max} - G_{III-av}|) / G_{III-av}$, varies from 1% to 7% (Figure IV. 38). The bigger the diameter d is, the smaller the value of Δ is. The specimen with $d=50\text{mm}$ is chosen for the coming experimental tests, where Δ is approximately 2.7%. It is recommended that d/D_{ring} equals to approximately 0.5 because the values of G_{III} are nearly uniform and the non-delaminated area is big enough for observation of crack propagation.

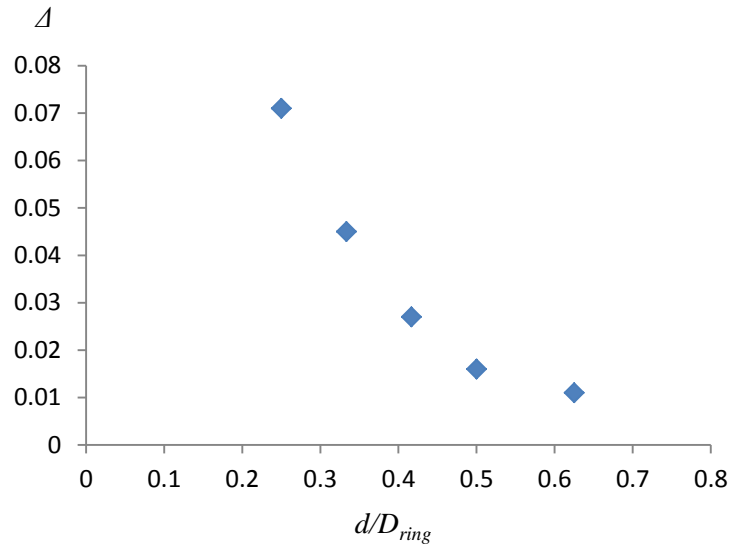


Figure IV. 38. Δ vs d/D_{ring}

IV.3.4. Combination of influence factors

The original ERCT test on composite specimens is in the case of the test with device A, whose geometry was chosen to adapt the jaws of the testing machine. The distribution of G_{III} is influenced by all the three factors discussed above. If there is a parameter f responsible for the evolution of G_{III} , it should depend on the superposition of the influence of the device factor, of the ratio d/D_{ring} and of the laminate factor. Actually, the effect of the device factor on the variation level Δ becomes smaller with a decrease of the ratio d/D_{ring} . In this case, f should be dominated by the laminate factor; in the other case, where device factor is big when d/D_{ring} is big, f should be controlled by the device factor. The idea is that the parameter f is maybe a useful tool for optimizing ERCT tests.

In order to understand the role of the superposition of different factors in the optimization of ERCT tests, we have studied an example. If we consider the curve of the results “C-compos-d50” resulting from laminate factor and that of “A-steel-d50” resulting from device factor, the curve of the results “A-compos-d50” should be the result of the superposition of above two factors: the laminate factor and that of device factor. The average of the curve of the results “C-compos-d50” and that of “A-steel-d50” looks similar to the curve of the results “A-compos-d50” shown also in Figure IV. 39. The definition of a parameter f seems useful to predict the evolution of G_{III} along the crack front. However, the results presented here are not rich enough to conclude on the definition and on the use of the parameter f . It is valuable to study this parameter with much more cases in the future.

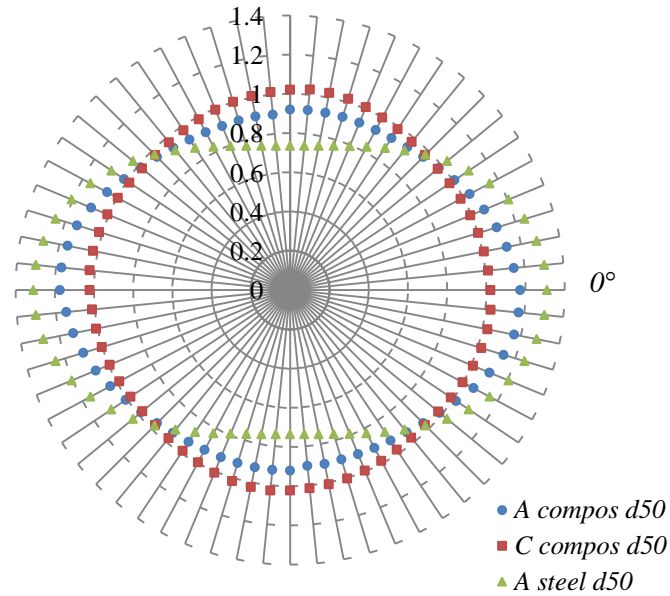


Figure IV. 39. Evolution of normalized G_{III} along the circular crack front with device C and A

IV.3.5. Optimization of the device

Device B is another modified version of device A, in which only the loading head is replaced by a cylinder. The specimen is installed as shown in Figure IV. 40 (a). If the specimen is turned 45° relative to the rigid plates (Figure IV. 40 (b)), it is named as B45. B45 has a better performance in reducing the variation of G_{III} , namely with 2.9% of improvement. Even though the improvement is negligible for our composite, the idea of the study is meaningful, which aims at optimizing the influence of the laminate factor combined with the device factor on the distribution of G_{III} . The former may become significant when some architectures of composite are used. In these cases, the laminate factor can be neutralized by the device factor in applying this kind of installation of the specimen relative to the device.

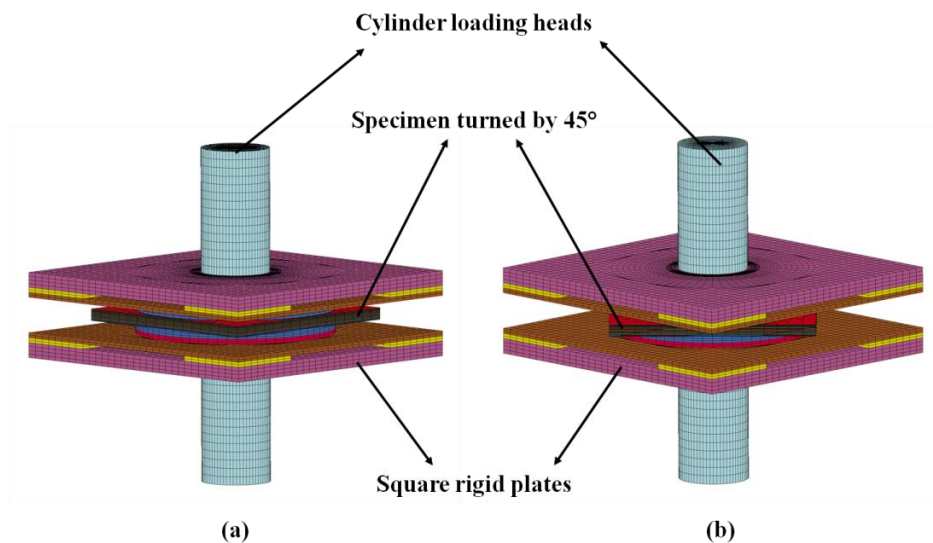


Figure IV. 40. Models for device B and B45

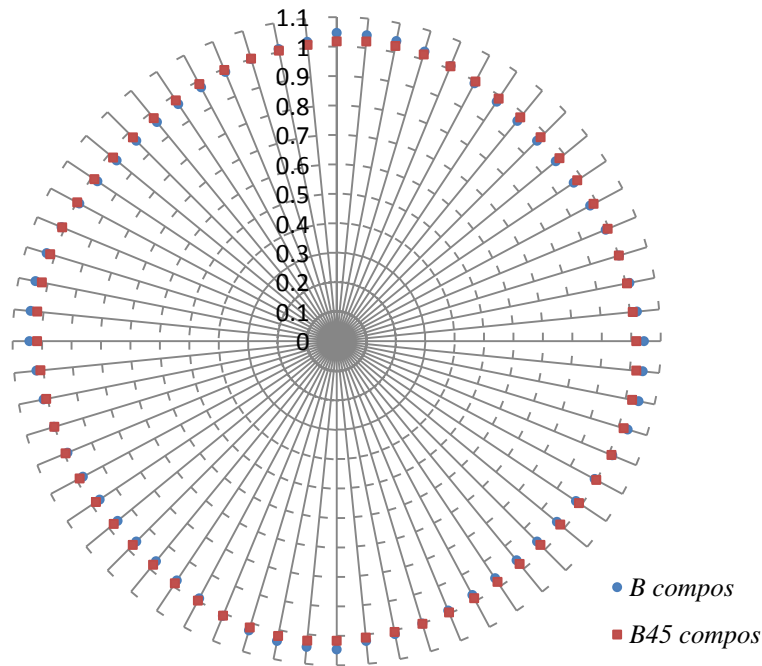


Figure IV. 41. Evolution of normalized G_{III} along the circular crack front with device

IV.3.6. Conclusions

Finite element analysis was performed in order to analyze the factors affecting the evolution of G_{III} along the circular crack front in ERCT test. It demonstrates that the distribution of G_{III} depends on the superposition of all influence factors, in particular the device factor and the laminate factor. Moreover, the device factor is in a positive correlation with the ratio d/D_{ring} while laminate factor is in a negative correlation with d/D_{ring} . For ERCT test the main influential factor is the device factor. Optimization of the device is effective but it is only meaningful when the laminate factor is big. The device C can realize a pure mode III delamination test and gives a uniform distribution of G_{III} along the crack front. The advice about the crack dimension is given. The optimal ratio d/D_{ring} equal to approximately 0.5 is recommended because the values of G_{III} are nearly uniform and the non-delaminated area is big enough for observation of the crack propagation.

IV.4. Modified Edge Ring Crack Torsion tests

Updated ERCT tests were proposed based on the finite element analysis above, aiming at achieving a pure mode III delamination test with uniform distribution of G_{III} along the circular crack front. The sensitivity study of the loading position, the shape of the crack front and the shape of the specimen to modified ERCT test were also carried out.

IV.4.1. Experimental

Firstly, two kinds of Modified ERCT devices were designed and fabricated. The tests were realized under the same conditions as those in the original ERCT test. In fact, the loading transfer conditions of the two tests are different. For ERC-III-1 tests, the applied load is

transferred on the specimen through the adhesive joint at the specimen's surfaces, while it is on the edge of the specimen through the screws in ERC-III-2 tests.

IV.4.1.1. ERC-III-1 test

The first one is shown in Figure IV. 42 and Figure IV. 43, named ERC-III-1 thereafter. The modification is only about the rigid plates and loading axes. Firstly, the loading head is changed into a cylinder loading axis of the same height ($\Phi=30\text{mm}$ and $h=72\text{mm}$). Moreover, the rigid plates are changed into circular ones. Note that d_{ring} and D_{ring} are always 80mm and 120mm respectively. In ERC-III-1 test, the same square ERCT specimens were used, because no influence of the geometry of the composite plate has been observed numerically. ERC-III-1 test is shown in Figure IV. 44. The dimensions of the specimen are $d = 50 \text{ mm}$, the side length of the square $D=120\text{mm}$, the total thickness of the specimen $h = 7\text{mm}$. 3 specimens were tested.

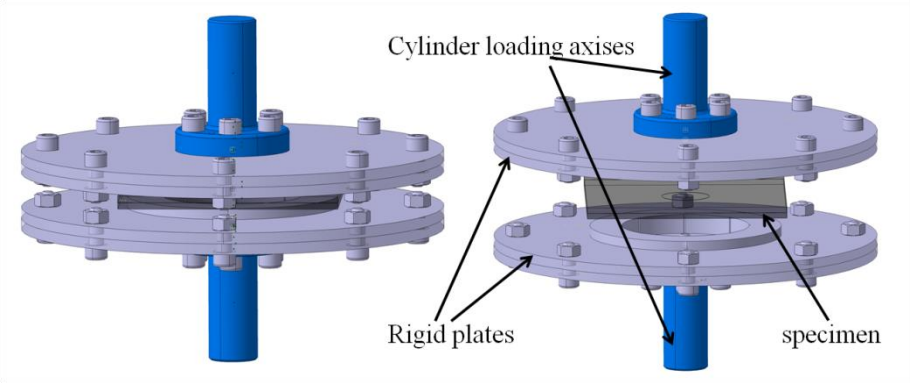


Figure IV. 42. Schema of MERCT test

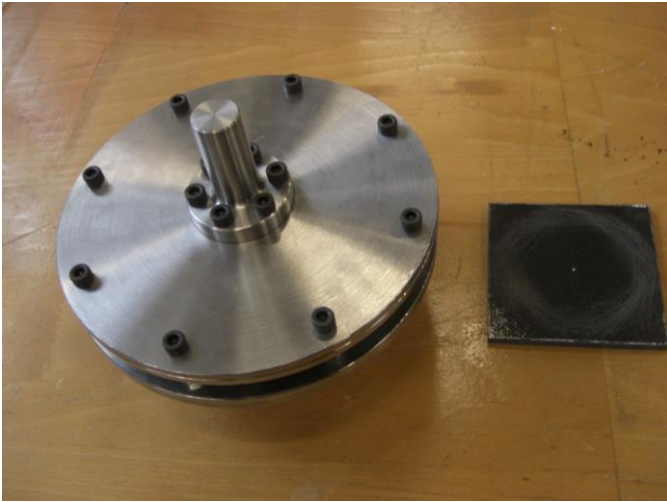


Figure IV. 43. A picture of ERC-III-1 device and specimen



Figure IV. 44. A picture of ERC-III-1 test

IV.4.1.2. ERC-III-2 test

The second modified ERCT test, named ERC-III-2, is schematized by Figure IV. 46. In this test, the specimen is no more pasted to the rigid plates. Instead, the heads of 12 screws are inserted into each sub-laminate and then these screws were fixed in the rigid plates and located in a circle. In this manner, the load is transmitted to the specimen essentially by barrier and friction (Figure IV. 47). The diameter of the loading circle can vary from 90mm to 140mm. The loading axis is the same as the one in ERC-III-1. In ERC-III-2 specimen nicks needed have been made by Water Jet Flow. The damage caused by this process is considered to have no effect on the crack tip, because it is far enough from the nick's zone. The diameter of the end of the nick in the specimen is semicircular with a diameter 4mm which is just a little bigger than the diameter of the screw head. Figure IV. 45 shows the specimen dimensions. d is equal to 50mm and the outer diameter of the specimens, D , is 110mm. So the nicks allow loading the specimen around a circular line of the diameter from 90mm to 110mm according the position of the screws. The diameter of the circular line is chosen as 90mm in our ERC-III-2 test. 3 specimens were tested. A picture of this ERC-III-2 test is given in Figure IV. 48.

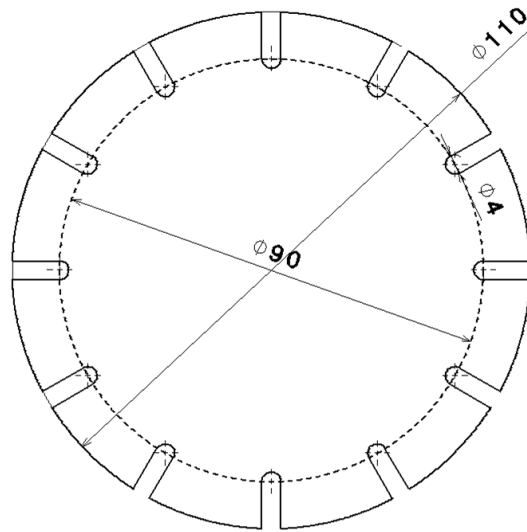


Figure IV. 45. Dimensions of ERC-III-2 specimen

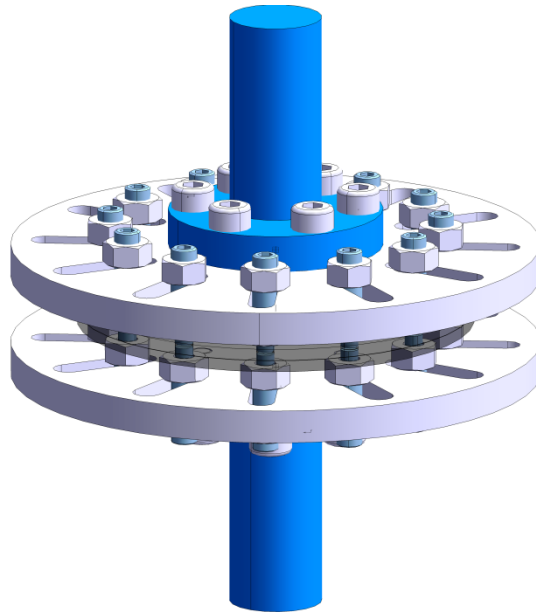


Figure IV. 46. Schematic of ERC-III-2 test

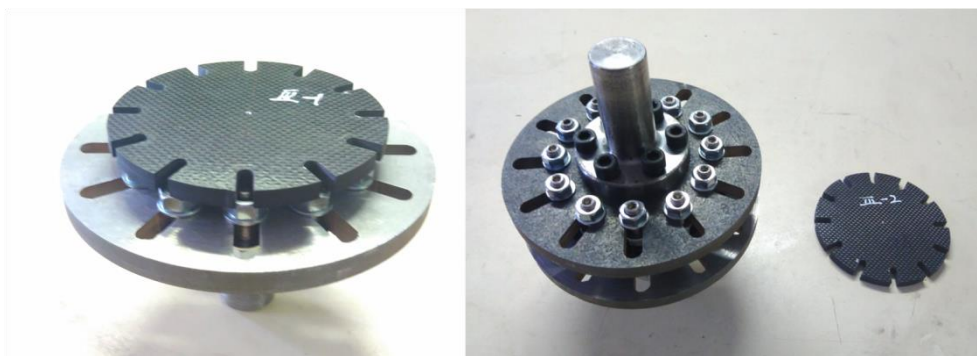


Figure IV. 47. Specimen and device of ERC-III-2 test

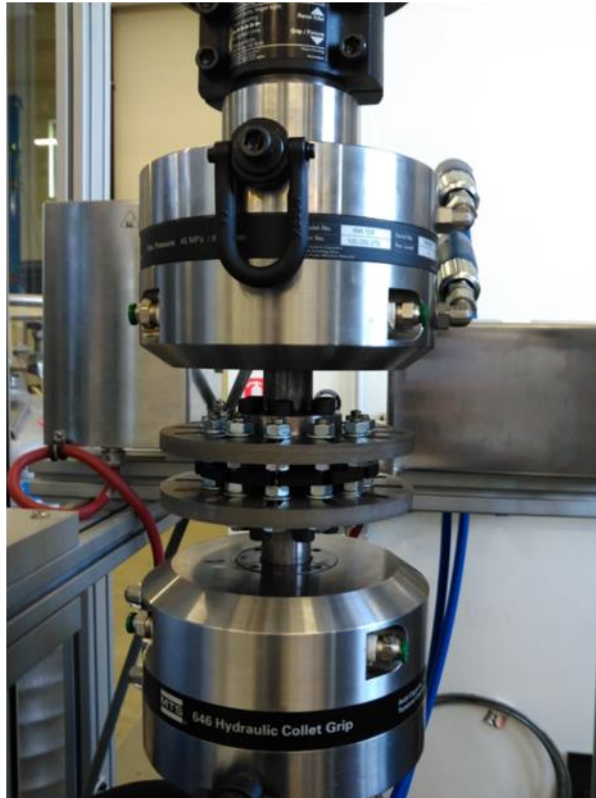


Figure IV. 48. A picture of ERC-III-2 test

IV.4.2. Sensitivity to the defaults of the geometry of the specimen and the device

Sensitivity study was done in order to detect the reproducibility of MERCT test by finite element analysis. The finite element model of MERCT test is device C with a square specimen, shown in Figure IV. 49. All the parameters of the material as well as the boundary conditions were set the same as those in ERCT model. VCCT was used to calculate the strain energy release rate of each mode at crack front. A polar coordinate (r, θ) is employed in order to show the evolution of G_{III} normalized by its average value or the evolution of G_I , G_{II} and G_{III} normalized by $G_T = G_I + G_{II} + G_{III}$ along the crack front.

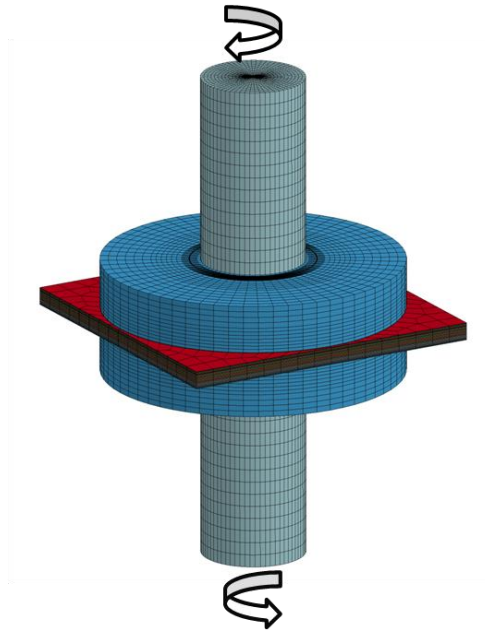


Figure IV. 49. Model of MERCT test

IV.4.2.1. Outer shape of the specimen

For the purpose to observe the influence of the outer geometrical shape of composite specimens on the distribution of G_I , G_{II} and G_{III} along the crack front, the numerical model of MERCT using the device C with a square composite specimen is established. The results are compared to those obtained on a circular one, and little difference was noted when the side length of a square specimen is equal to the diameter of a circular one, as shown in Figure IV. 50. Actually in experimental tests, any shape of specimen can be chosen. In this study the square one was chosen for practical reasons.

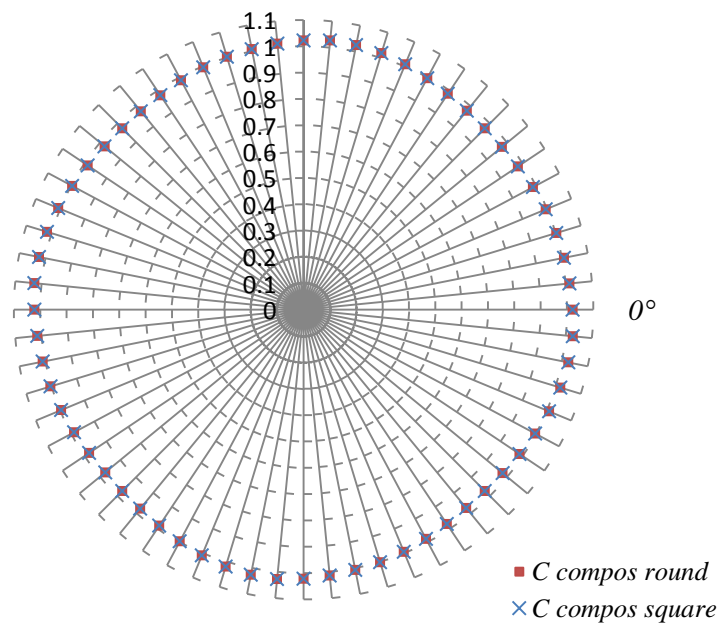


Figure IV. 50. Evolution along the crack front of G_{III} normalized by the average value with round specimen and square specimen

IV.4.2.2. Circularity of the crack front

A shape default of the crack front may be introduced during the cutting of the polymer film. Thus, a finite element analysis about the shape of the crack front was carried out. In the test with device C, an oval crack front ($2b=48\text{mm}$ at 90° , $2a=50\text{mm}$ at 0°) is set instead of the circular one with $d=50\text{mm}$. The result presented in Figure IV. 51 shows that little increase of mode I and II components are found so that it's still in pure mode III delamination. Moreover it is shown in Figure IV. 52 that the variation of G_{III} along the oval crack front is more important than that of a circular one. Note that $\Delta = 9\%$ for the former while $\Delta=2.7\%$ for the later.

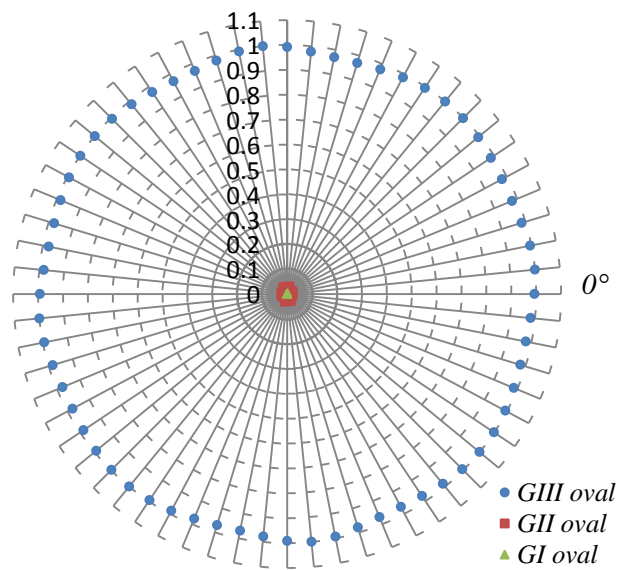


Figure IV. 51. Evolution along the crack front of G_b , G_{II} and G_{III} normalized by G_T with oval crack front

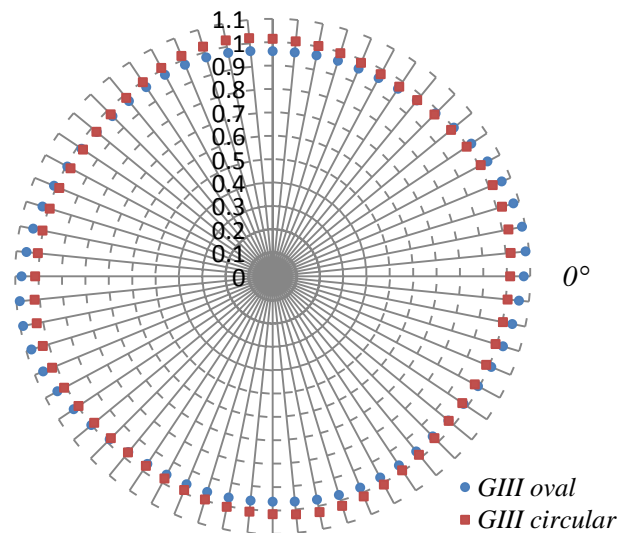


Figure IV. 52. Evolution along the crack front of G_{III} normalized by the average value with oval and circular crack front

IV.4.2.3. Relative position of the crack front

(1) Default of parallelism

The loading axis is perpendicular to the rigid plate so that the two rigid plates are always parallel when the loading axes are blocked in the jaws of a torsional machine. However, the specimen can be inclined if the thickness of the bondline is not uniform. In this situation, the torsional loading axis is not perpendicular to the crack front. In order to study the error caused by this situation, a FE model is established where the thickness of bondline varies from 0.2 mm to approximately 2.2 mm. An angle 1° is formed between the specimen surface and the rigid plate. The results presented in Figure IV. 53 show that little increase of mode I and II components is found so that it's still a pure mode III delamination. Figure IV. 54 shows that there is practically no effect of the default of parallelism, because the distribution of G_{III} normalized by its average value from two cases coincide.

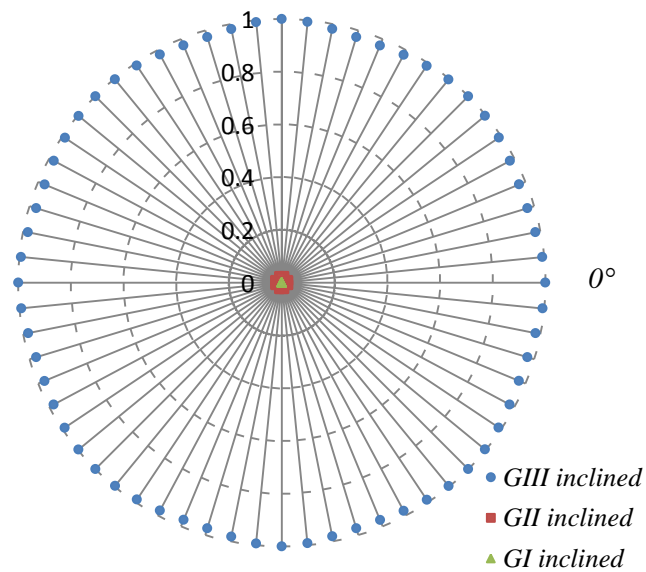


Figure IV. 53. Evolution along the crack front of G_I , G_{II} and G_{III} normalized by G_T with inclined crack front

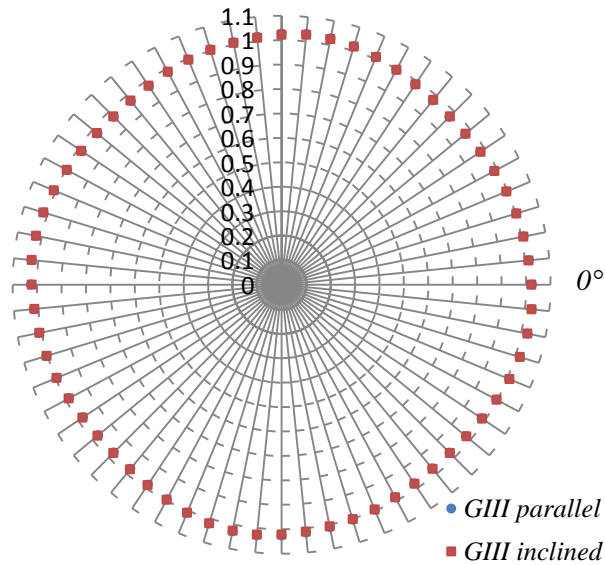


Figure IV. 54. Evolution along the crack front of G_{III} normalized by the average value with parallel and inclined crack front

(2) Default of the alignment between the loading shafts and the center of the crack

Theoretically, mode II component will be introduced if the center of the crack in specimen and the axis of loading shafts are not aligned. This is a main concern about the feasibility and practicality of MERCT. A finite element analysis was carried out to observe the effect of the alignment on the distribution of G_I , G_{II} and G_{III} along the crack front. A specimen with $d=50\text{mm}$ was modeled by introducing 2mm of deviation (4% of d) between the crack center of the specimen and the axis of the loading shafts. Note that relative to the crack center of the specimen the axis of the loading shafts was simply displaced of 2mm to the positive direction of r at 0° . The results are shown in Figure IV. 55. It is shown that the increase of mode I and II components is so small that pure mode III delamination can be always considered. Figure IV. 56 compares the results obtained from MERCT with and without the default of the alignment. It is seen that the distribution of G_{III} along the circular crack front is displaced towards the same direction of r at 0° in general. $\Delta=10\%$ is found at the positive direction of r at 0° relative to the crack center of the specimen.

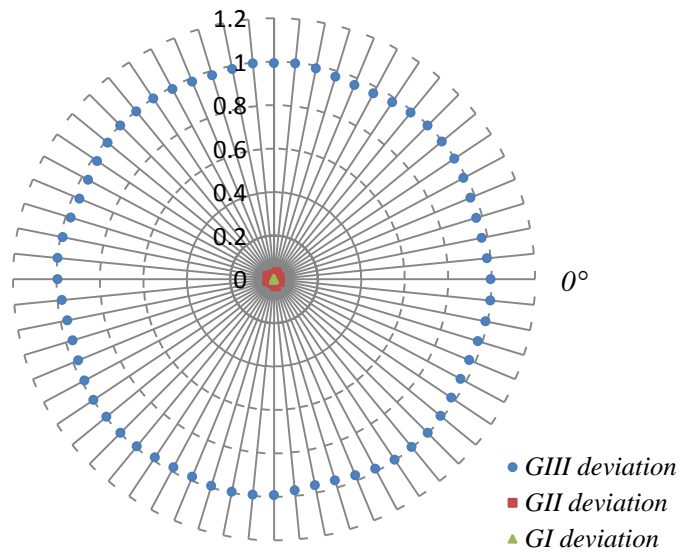


Figure IV. 55. Evolution along the crack front of G_I , G_{II} and G_{III} normalized by G_T with loading axis deviation

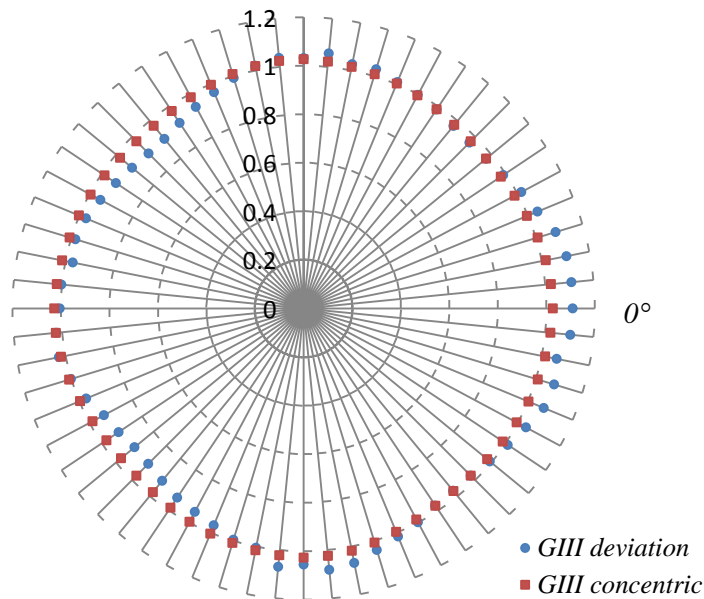


Figure IV. 56. Evolution along the crack front of G_{III} normalized by its average value with and without the default of the alignment

IV.4.3. Data reduction methods

Tada formula expressed by Eq. 43 for ERCT test is more suitable in MERCT test because the loading condition is completely axisymmetrical and so similar to the original situation. Herein, the pure mode III toughness can be determined by Tada's formula Eq. 43 and Eq. 44, denoted $G_{III\text{-Tada}}$ or by finite element analysis, named $G_{III\text{-FEM}}$ that presents an average value of G_{III} at the critical load. This average is physically meaningful because the variation of G_{III} along the crack front is limited.

IV.4.4. Results and discussions

IV.4.4.1. Modified Edge Ring Crack Torsion-1 (ERC-III-1) test

In the ERC-III-1 test, the crack propagates towards the centre in an unstable manner. Figure IV. 57 shows a typical experimental torque/rotation angle curve, where a sudden drop in the torque corresponding to the crack propagation is observed. Note that the experimental curve is not really linear up to the peak load, but the repeatability of the test is relatively good.

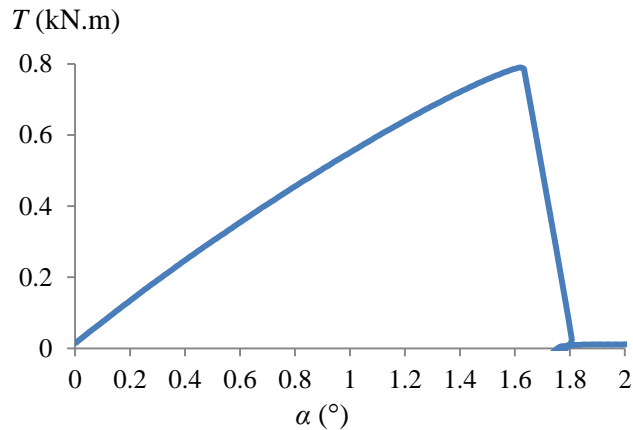


Figure IV. 57. Typical experimental torque/rotation angle curve of ERC-III-1 test

IV.4.4.2. Modified Edge Ring Crack Torsion-2 (ERC-III-2) test

In the ERC-III-2 test, the crack propagates towards the centre in a stable manner. Figure IV. 58 shows a typical experimental torque/rotation angle curve, where a sudden drop in the torque is observed. This point should be corresponding to the crack onset, where a local unstable crack growth occurs. And then the torque kept on increasing with a stable propagation of the crack until a total fracture of the specimen. Note that the experimental curve is not really linear up to the first peak load. And the first peak torque is considered as the critical load.

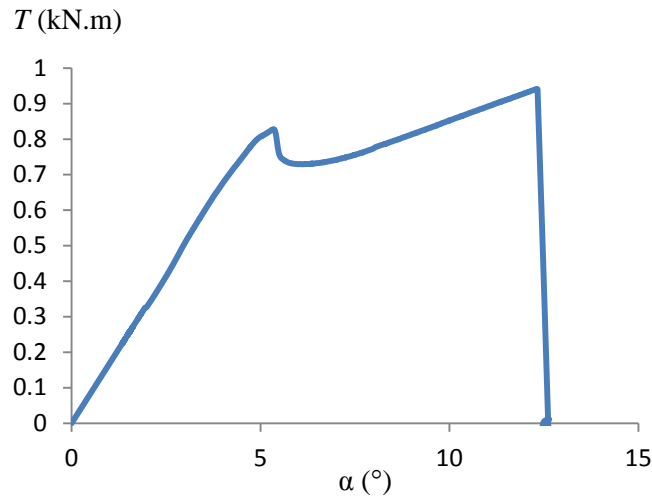


Figure IV. 58. Typical experimental torque/rotation angle curve of ERC-III-2 test

MERCT test (ERC-III-1) has been simulated by a finite element model to obtain the distribution of the strain energy release rates. Figure IV. 59 shows the evolution of normalized G_{III} along the crack front using the ERCT and MERCT devices. The modification of the mode III device conduces to more uniform distribution of G_{III} in the ERC-III-1 specimen with $d=50\text{mm}$, where Δ is less than 2.8%. As a comparison, Δ from an original ERCT test is approximately 17.4% for a specimen with $d=50\text{mm}$, and Δ is approximately 14.0% from ECT-2 test. The improvement on the distribution of G_{III} seems effective by using axisymmetrical device. Moreover, mode I and mode II components over the total strain energy release rate stay below 1.4% as shown in Figure IV. 60, so can be considered as negligible. As a comparison, mode II component from ECT-2 test becomes significant at the sides of the crack front. Therefore, the interest of this pure mode III test is evident. In conclusion, MERCT test can be considered as a pure mode III delamination testing method and with uniform distribution of G_{III} along the crack front.

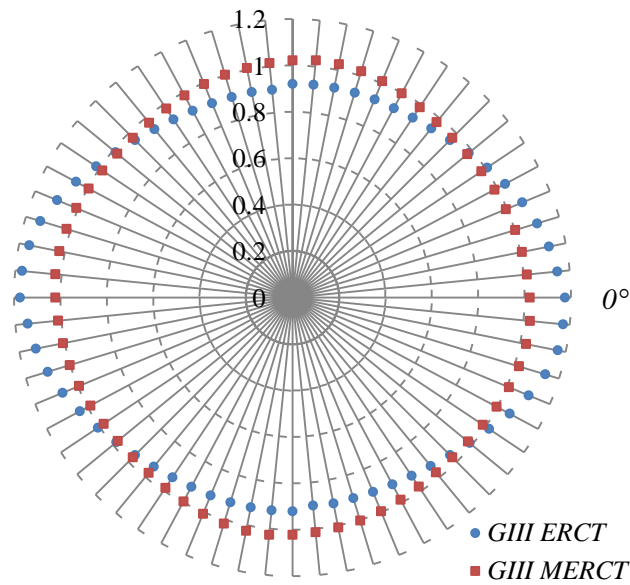


Figure IV. 59. Evolution along the crack front of G_{III} normalized by the average value obtained from ERCT test and from ERC-III-1 test

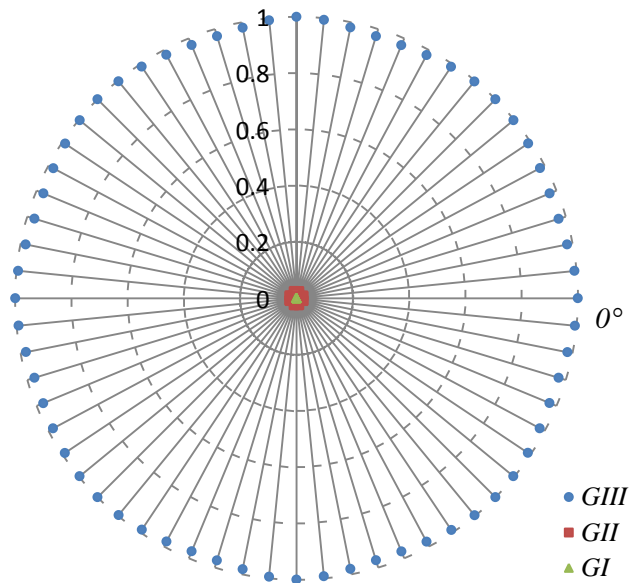


Figure IV. 60. Evolution along the crack front of G_I , G_{II} and G_{III} normalized by G_T obtained from ERC-III-1 test

Concerning the measurement of the pure mode III toughness, by introducing the average critical load obtained from a series of ERC-III-1 tests, the peak load considered, pure mode III toughness was obtained for the tested composite: $G_{III-C-FEM}=1049$ (N/m). By introducing the average critical load obtained from ERC-III-2 tests, $G_{III-C-FEM}=1254$ (N/m) was obtained. The $G_{III-C-FEM}$ from ERC-III-1 test is 16% smaller than that from ERC-III-2 test. Furthermore, taking Δ into consideration, these values are quite close to that measured by the Edge Crack-torsion test (ECT), valued at 1213 (N/m).

The results of G_{III} from two MERCT tests according to Eq. 43 and Eq. 44 are listed in Table. 18. It also shows that the value from ERC-III-1 test is about 17% smaller than the one from ERC-III-2 test. Additionally, values of $G_{III-Tada}$ agree well with $G_{III-FEM}$. For these two tests, $G_{III-Tada}$ is about 8% bigger than $G_{III-FEM}$.

Test	T_{C-av} (N.m)	G (MPa)	K_{III} (MPa.m ^{1/2})	$G_{III-Tada}$ (N/m)
ERC-III-1	754 ±31	5400	3.22	961 ±81
ERC-III-2	829 ±21	5400	3.54	1159 ±59

Table. 18. G_{III} obtained from Tada's formula for MERCT tests

IV.4.5. Conclusions

In this section, two novel pure mode III testing methods were developed and evaluated including modified ERCT-1 (ERC-III-1) test and modified ERCT-2 (ERC-III-2). The modification on the original ERCT test concerns in particular the geometry of the parts for transmitting the applied torque to the specimens. These modified parts in both of two versions are cylindrical so as to assure axisymmetrical loading. But the loading transfer for the two tests is realized in a different manner. For ERC-III-1 tests, the load is applied on the surfaces of the specimen through a ring adhesive joint; while in ERC-III-2 tests it is applied at the circular edge of the specimen through the contact between the screws and nicks machined in the specimen.

The tests developed here were performed on a multi-directional quasi-isotropic and quasi-homogeneous laminate. Finite element analysis (FEA) was used to evaluate the quality and the robustness of the tests.

The most significant advantages of MERCT tests are shown including:

- the fracture mode is pure mode III without the participation of mode I or mode II components indeed;
- good distribution of G_{III} along the crack front. Δ is much smaller than ECT tests and original ERCT test. In fact, a nearly constant value of G_{III} along the crack front is obtained in the MERCT tests. So it's more acceptable to consider the average value, $G_{III-FEM}$, as the material toughness;
- the agreement between $G_{III-Tada}$ and $G_{III-FEM}$ is good with a difference approximately 8% for both MERCT tests. $G_{III-Tada}$ is smaller than $G_{III-FEM}$, which guarantees the security to consider $G_{III-Tada}$ as the delamination toughness.

Some drawbacks of MERCT tests exist in the manufacture process and installation of the testing devices. The parallelism of the rigid plates and the alignment between the crack center of the specimen and the axis of loading shafts should be checked carefully. For ERC-III-1 tests, it is time consuming to clean the glue on the surface of the rigid plates before sticking the specimen for each test. For ERC-III-2 tests, some care must be taken in order to reduce the assembly stress because a lot of screws are employed.

In conclusion, both of the two MERCT tests are able to achieve a pure mode III delamination and give nearly uniform distribution of G_{III} along the circular crack front. It maybe presents the best result so far in terms of two aspects: the elimination of mode I and II components and

the reduction of G_{III} variation along the crack front. The robustness of MERCT tests is well confirmed. Some defaults come from the manufacturing process and the testing process are generally inevitable. Unwanted fracture mode introduced by different defaults seems not significant. But the variation of G_{III} along the crack front is more sensitive to certain defaults, such as the circular shape of the crack front and the alignment between the crack center and the axis of loading shafts.

Above all, ERC-III tests are promising testing methods to characterize mode III delamination behavior. In ERC-III-1 test, an unstable crack growth was observed. And in ERC-III-2 test, at onset of delamination the crack propagated a step suddenly, following by a stable crack growth. This phenomenon makes it possible to stop the test before the final fracture of the specimen to observe the onset of crack growth.

IV.5. Conclusions

IV.5.1. Comparison of pure mode III toughness G_{IIIc} obtained by different methods

The average values of G_{IIIc} measured by different tests are compared in Table. 19. Theoretically, the toughness under pure delamination mode in terms of the critical strain energy release rate is believed intrinsic to the material but the measured values are influenced not only by the testing and calculating methods but also by the geometry of the tested specimens. This means that the measurement of G_{IIIc} is problematic.

Type of test	$G_{IIIc-FEM}$ (N/m)	$G_{IIIc-CC}$ or $G_{IIIc-Tada}$ (N/m)	Difference
ECT-1 (a=20mm)	945	1310±80	39%
ECT-2 (a=20mm)	1213	1017±44	16%
ERCT (d=30mm)	890	910±34	2%
ERCT (d=50mm)	1173	932±11	21%
ERC-III-1 (d=50mm)	1049	961±80	8%
ERC-III-2 (d=50mm)	1254	1159±59	8%

Table. 19. Comparison of G_{IIIc} obtained from different methods

For ECT-1 test, the critical strain energy release rate measured is probably under mixed mode instead of pure mode III. Moreover, the use of an average value of G_{III} determined by finite element analysis, $G_{IIIc-FEM}$, as the toughness is not really meaningful, because the variation of G_{III} along the crack front is too important. As a result, the results coming from this test are not reliable, they should be out of the comparison of G_{IIIc} . Optimization on specimen geometry and the stacking sequence may reduce errors in tests. However, we didn't optimize them in order to compare with the following tests with the specimens of the same stacking sequence.

Modified ECT-1 (MECT-1) test provides a better performance than ECT-1 test by improving the uniformity of G_{III} along the crack front. The evolution of G_{III} is fairly uniform in the middle domain along the crack front while the values of G_{III} approach 0 at the extremities, where mode II component increases and becomes the principal mode. Even though the delamination mode around the edges of the crack front should be under mixed mode II+III, the maximum of G_{III} at the middle area of the crack front is practically the same than the one

of G_{II} at the two extremities of the crack front. The interest of this test can be described as following:

If $G_{IIC} < G_{IIIc}$, the onset of delamination should be at the two extremities of the crack front;

If $G_{IIC} > G_{IIIc}$, the onset of delamination should be at the center area of the crack front;

If $G_{IIC} = G_{IIIc}$, the onset of delamination should be simultaneously at all crack front.

In future work, it is valuable to realize MECT-1 tests to characterize the delamination behavior of composite.

In ECT-2 test, there is much less participation of G_I and G_{II} components. The distribution of G_{III} is uniform in the middle domain of the crack front while G_{III} drop to almost zero at the extremities. As ECT-1 test, the variation of G_{III} along the crack front is too important to use its average value as material toughness. Actually, $G_{IIIc-FEM}$ for ECT-2 listed in Table 18 represents the average value of those calculated by finite element analysis, which becomes 20% higher than $G_{IIIc-CC}$. Besides, the critical load corresponding to the onset of crack growth is not easy to define in this test because strong nonlinearity is observed before the maximum load is attained.

Concerning ERCT test, according to the results from finite element analysis the delamination mode in this test is pure mode III without the presence of mode I or mode II; the variation of G_{III} along the crack front decreased substantially compared to ECT tests, and it can be even less than 7.6% by optimization of the geometry of the specimen. So it's acceptable to consider its average value as the material toughness. Note that $G_{IIIc-FEM}$ for ERCT test with specimens $d=30$ mm and $d=50$ mm are 26.6% and 3.3% smaller than the one from ECT-2 test respectively. However the variation of G_{III} along the crack front can still not be eliminated. The bigger the diameter d , the more important the variation of G_{III} and then the more different the average value of G_{III} obtained from EFM and that determined by Tada's formula.

Then the factors affecting the evolution of G_{III} along the crack front were studied. It demonstrates that the distribution of G_{III} depends on the superposition of all influence factors, in particular that of device factor and laminate factor. Moreover, the device factor can mitigate the variation of G_{III} due to the ratio d/D_{ring} so in a positive manner, but the laminate factor can accentuate the variation of G_{III} due to the ratio d/D_{ring} , so in a negative manner. The main influence factor is the device factor, especially for a specimen with a big d/D_{ring} . Tada's formula is found a simple and practical approach to determiner G_{IIIc} , which gives the results good enough only when the variation of G_{III} is small. An optimal ratio d/D_{ring} equal to approximately 0.5 is recommended because the values of G_{III} are nearly uniform and the non-delaminated area is big enough for observing the crack propagation.

Finally, modified ERCT (MERCT) tests were developed and evaluated in two versions based on the finite element analysis above, aiming at achieving a pure mode III delamination test with uniform distribution of G_{III} along the circular crack front. The modification on the original ERCT test concerns in particular the geometry of the device parts for transmitting the load to the specimens in an axisymmetrical manner. For ERC-III-1 tests, the load is applied on the surfaces of the specimen through a ring adhesive joint; while in ERC-III-2 tests it is applied at the circular edge of specimen through the contact between the screws and nicks machined in the specimen. Finite element analysis (FEA) was used to evaluate the quality and the robustness of the tests, as well.

The most significant advantages of MERCT tests are:

- The fracture mode does be pure mode III without the participation of mode I or mode II components;
- Good distribution of G_{III} along the crack front. Δ is much smaller than ECT tests and original ERCT test. In fact, a nearly constant value of G_{III} along the crack front is obtained in the MERCT tests. So it's more acceptable to consider the average value, $G_{III-FEM}$, as the material toughness;
- The agreement between $G_{III-Tada}$ and $G_{III-FEM}$ is good with a difference only approximately 8% for both MERCT tests. $G_{III-Tada}$ is smaller than $G_{III-FEM}$, which guarantees the security to consider $G_{III-Tada}$ as the delamination toughness;
- The robustness of MERCT tests is well confirmed. Some defaults introduced by the manufacture process and test process are generally inevitable. Unwanted fracture mode introduced by different defaults seems no significant. But the variation of G_{III} along the crack front is more sensitive to certain defaults,

In conclusion, MERCT tests are promising testing methods to characterize mode III delamination behavior. In ERC-III-1 test, an unstable crack growth was observed. And in ERC-III-2 test, at onset of delamination the crack propagated a step suddenly, following by a stable crack growth. This phenomenon makes it possible to stop the test before the final fracture of the specimen to observe the crack growth at the onset.

IV.5.2. Comparison of G_{IC} , G_{IIC} and G_{III}

The delamination toughness under the three pure modes is listed in Table. 20. They were obtained from DCB, ENF and ERC-III-2 tests. ERC-III-2 test was preferred because it has smaller standard deviation. It is shown that in the cases of DCB and ENF tests the average value from finite element analysis can be quite different from the one determined by compliance calibration method. For DCB test, the distribution of G_I along its straight crack front is not uniform with $\Delta=29.1\%$. In addition, the length of the crack front is much shorter compared to ECT and ERC tests so that the variation has a bigger influence on the result. So G_{IC-FEM} given here should be not meaningful. Instead, the maximum value $G_{IC-FEM-max}$ should be considered, which is shown in Table. 20. For the rest, average values by FEM are considered. Concerning ENF test, the distribution of G_{II} is relatively good with $\Delta=7.2\%$, so $G_{IIC-FEM}$ given here should be meaningful. Recall that the participation of mode III at the edges of the crack front is observed in ENF test, which could interfere with the measurement of G_{IIC} . However in the case of ERC-III-2 where the variation of G_{III} is small with $\Delta=2.7\%$, the difference between the value from FEM and the one from Tada's formula is only 8%. Based on the toughness obtained from CC or Tada's methods, G_{III} is 27% higher than G_{IIC} , the former becomes 62% than the later if we refer to the average values from FEM. The difference between G_{IIC} and G_{III} does seem significant for the composite tested. This observation should be generalized, because the pure mode II and pure mode III are two independent fracture modes. So the corresponding behavior can be very different one from another for some materials, or similar for others materials.

Mode	G_{C-FEM} (N/m)	G_{C-CC} or G_{C-Tada} (N/m)	Test
I	450	460±23	DCB
II	776	914±63	ENF
III	1254	1159±59	ERC-III-2

Table. 20. Toughness of pure mode I, pure mode II and pure mode III

CHAPTER V. DELAMINATION UNDER PURE MODE I, PURE MODE II AND MIXED MODE USING MODIFIED EDGE RING CRACK SPECIMEN

V.1. Pure mode I and pure mode II

In chapter III, the Edge Ring Crack Torsion test was studied. The main advantage of the Edge Ring Crack specimen, called ERC thereafter, is the total absence of the extremities of crack front and so no edge effects on the results. The application of ERC specimen can be spread into other modes of delamination.

With the help of the test devices developed in our study, different loading modes can be introduced so that the behavior of delamination in laminated composites can be investigated under every pure mode load, even under some mixed modes ones.

In this section pure mode I and pure mode II delamination tests were developed using ERC specimen. In this way, the three pure modes toughness measured should be more representatives with no additional effects on the results due to geometry change.

V.1.1. Experimental

According to the stacking sequence described in chapter I, 32 plies were set up to obtain quasi-isotropic and quasi-homogeneous ERC specimens, where the crack plane separates symmetrically the whole laminate into two sub-laminates, exactly like the specimens in ERC-III tests.

ERC specimens can be loaded under pure mode I condition, named ERC-I test. The same device as in ERC-III-1 test can be used while the loading condition is changed into traction instead of torsion, shown in Figure V. 1. ERC specimen under pure mode II loading, named ERC-II test, uses a new device, shown in Figure V. 2. Herein, the specimen was put on a rigid supporting ring of diameter $D=110\pm 2\text{mm}$, and then loaded under compression in the centre of the specimen. Note that ERC specimen under pure mode I load has to be pasted to the testing device, where the adhesive joints must be strong enough to guarantee the crack propagation in the mid-plane of the composite specimen, but not in the adhesive joint between the rigid plates of the test device and the surfaces of the specimen. A structural adhesive ARALDITE 2012 has been used for this purpose. For all of these tests, great care was paid to keep the coincidence between the center of the crack of the specimens and the loading axis of the testing machine in order to ensure the wanted pure loading mode.

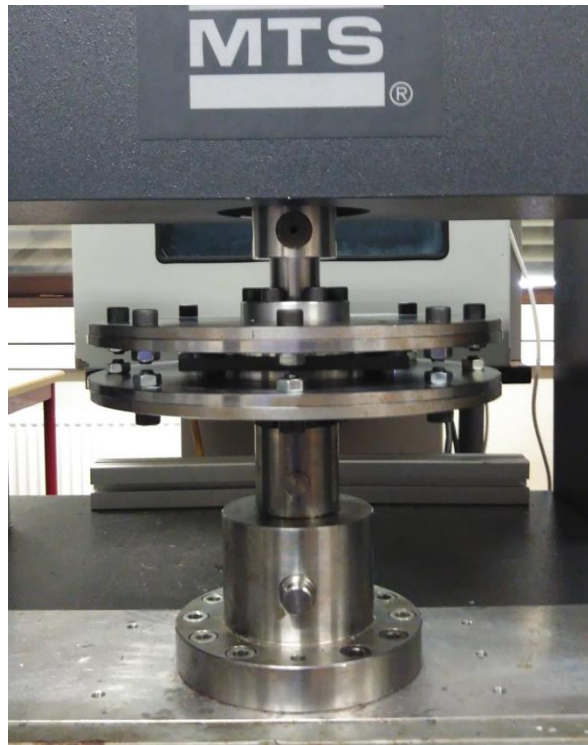


Figure V. 1. A picture of ERC-I test

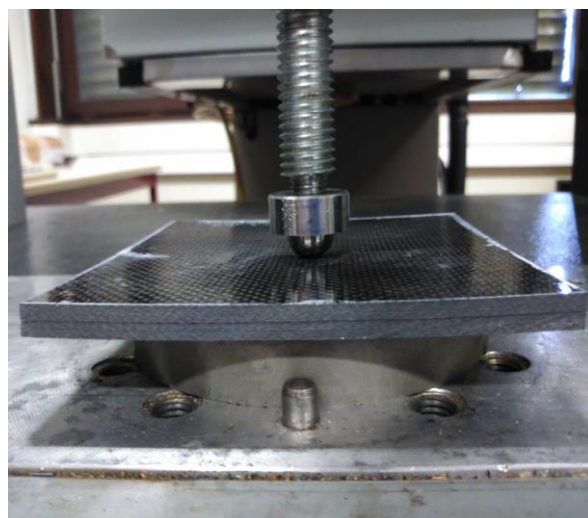


Figure V. 2. A picture of ERC-II test

V.1.2. Finite element analysis

The numerical model of ERC-I and ERC-II test are shown in Figure V. 3 and Figure V. 4 respectively.

In ERC-I model, a displacement curve 8mm was employed on both of the loading axes in order to impose a traction load. All the rest parameters were set as in ERC-III model. In ERC-II model, a displacement curve 3mm was employed on the loading ball while the supporting

ring was fixed. A surface to surface contact was set between the specimen surface and the balls, between the supporting ring and specimen surface and between the two sub-laminates of the specimen. The other parameters were set the same as in ERC-III model.

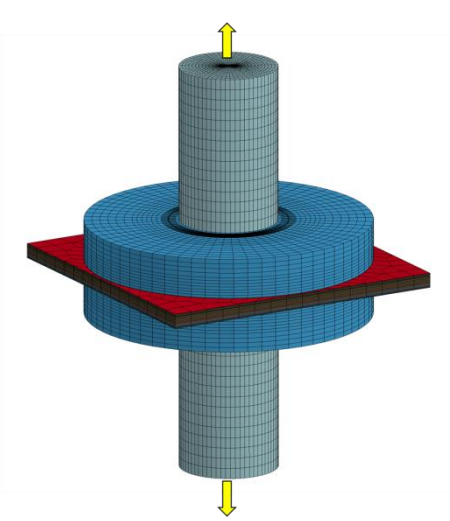


Figure V. 3. Mesh for ERC-I test

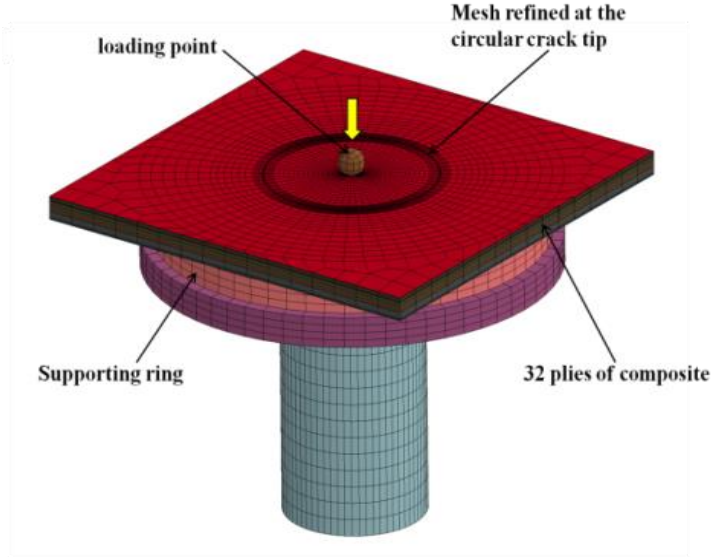


Figure V. 4. Mesh for ERC-II test

V.1.3. Results and discussions

V.1.3.1. Edge Ring Crack mode I test (ERC-I)

Typical experimental force/displacement curve from the ERC-I test is shown in Figure V. 5. It is shown that the peak load is very different from the load at the end of linear part, where a stable propagation of the crack could occur before an unstable crack growth. The simulation results in Figure V. 6 indicate that there is no participation of mode II and mode III

components. The distribution of G_I is practically constant as shown Figure V. 7. However, in Double Cantilever Beam (DCB) test Δ is 29.1% when DCB specimens have the same stacking sequence as the one of ERC ones.

In conclusion, ERC-I test is a pure mode I delamination test with uniform distribution of G_I along the crack front. Therefore, with the average critical load measured, we can determine the pure mode I toughness G_{IC} . In this work, if the peak tensile load is defined as the critical load, the value of G_{IC} determined as the average value from FEM is given as 319N/m, which is quite close to the value 348N/m measured by DCB test on the same composite. However, the definition of critical load corresponding to the crack onset needs further experimental observations. However, evident nonlinearity appears before reaching the peak tensile load. In this case, the end of the linear part should be considered as the critical load as well. By applying the force at the linear end, G_{IC} is equal to 184N/m, which is 42.3% smaller than that calculated by peak load. By applying the load at the intersection of the curve and a line at 95% of initial slope of the linear domain, G_{IC} is given as 210 N/m, which is 34.2% smaller than the one calculated with the peak load value. In our test, the loading axis of our testing device is not strictly corresponding to the jaws of the tensile machine. As a result, the loading axis may be not perpendicular to the crack plane. The small tilt angle may induce errors. Anyway, more ERC-I tests should be repeated in order to give a typical experimental force/displacement curve of ERC-I test and the crack onset should be verified in the future.

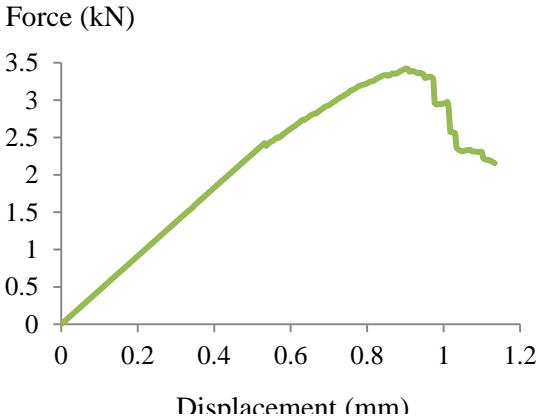


Figure V. 5. Experimental force/displacement curve of ERC-I test

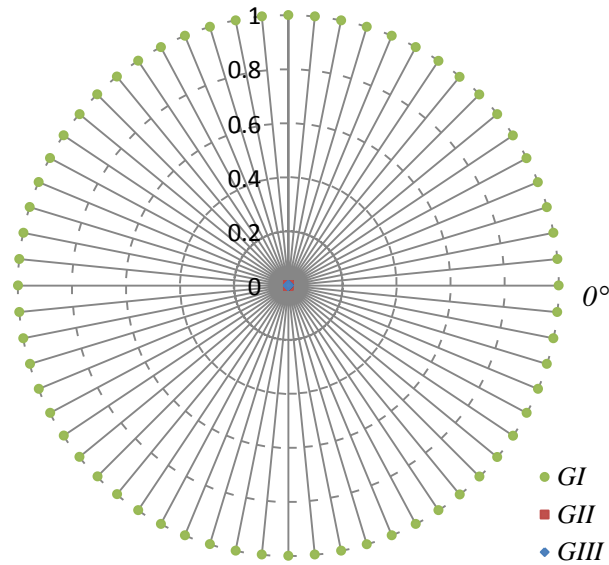


Figure V. 6. Evolution along the crack front of G_I , G_{II} , G_{III} normalized by G_T in ERC-I test

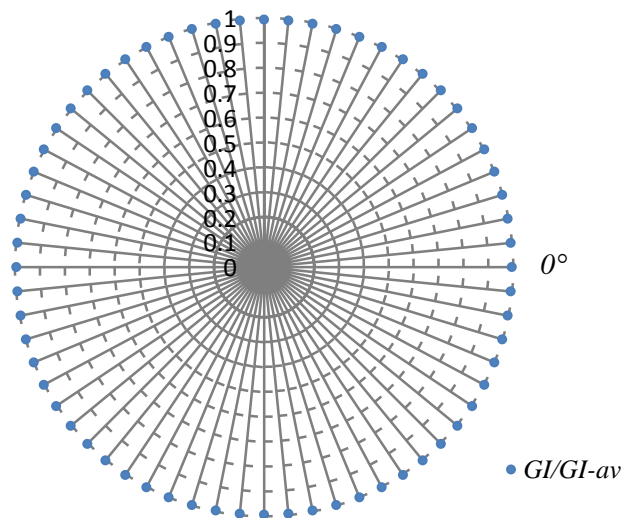


Figure V. 7. Evolution along the crack front of G_I normalized by G_{I-av} in ERC-I test

V.1.3.2. Edge Ring Crack mode II test (ERC-II)

Figure V. 8 shows a typical experimental force/displacement curve from the ERC-II test. After a small non linear part, an unstable propagation of the crack is observed, which is corresponding to a sudden drop in the compression load. Actually, most of the advantages of ERC-III are kept in the ERC-II test. Figure V. 9 shows the evolution along the crack front of G_I , G_{II} , G_{III} normalized by G_T in ERC-II test. It is seen that the relative mode I and mode III components are less than 1.5%, so they can be considered as negligible. Moreover, the distribution of G_{II} along the crack front (Figure V. 10) is more uniform than that in ENF test. As a comparison, Δ is approximately 4.0% in ERC-II test while Δ is approximately 7.2% in ENF test on the same composite with the same stacking sequence.

In conclusion, a pure mode II delamination test is achieved by using ERC-II test with uniform distribution of G_{II} along the crack front. By introducing the average peak load obtained by series of ERC-II tests, the pure mode II toughness G_{IIC} of the tested composite is measured at 1109 (N/m), which is determined as the average value from FEM. However, the value of G_{IIC} measured by ENF test on the same composite is much lower, valued at 776 (N/m) from the same numerical method. The difference can be explained by the facts including the bigger Δ , the participation of mode III and the geometry effect in ENF test. The nonlinearity appears before force reaching the peak value but the nonlinear part is much smaller than in ERC-I test. By introducing the load at the end of the linear domain, the pure mode II toughness G_{IIC} of the tested composite is measured at 829N/m.

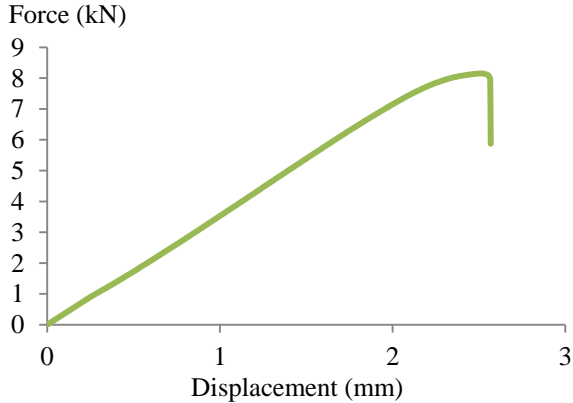


Figure V. 8. Typical experimental force/displacement curve of ERC-II test

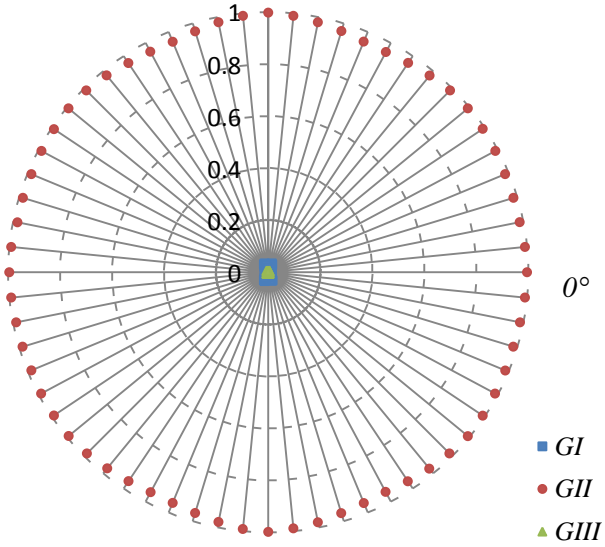


Figure V. 9. Evolution along the crack front of G_b , G_{Ib} , G_{III} normalized by G_T in ERC-II test

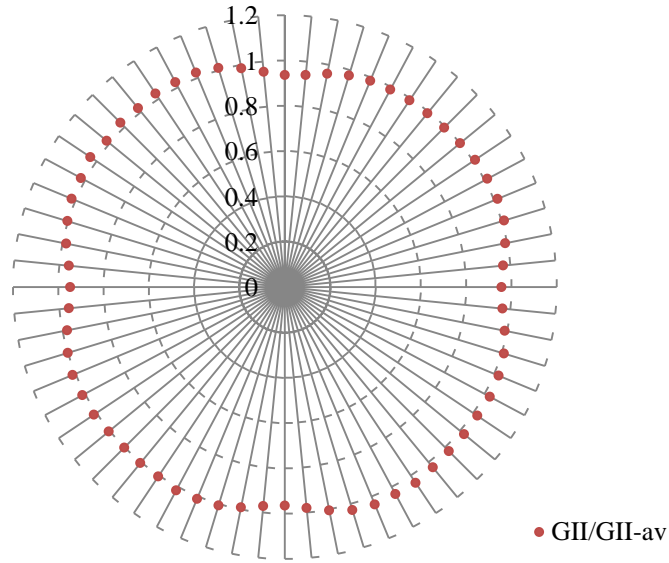


Figure V. 10. Evolution along the crack front of G_{II} normalized by G_{II-av} in ERC-II test

V.1.4. Conclusions

ERC specimen is very promising in order to characterize the delamination behavior of laminated composites.

Firstly, by introducing different loadings, the pure mode I, the pure mode II and the pure mode III delamination tests can be performed on the ERC specimens of the same geometry. So the influence of the geometry of the specimens on the toughness measured can be avoided.

Secondly, the evolution of the strain energy release rate along the crack front is fairly uniform, where the average value is more meaningful. It is important to develop a closed-form expression to determine easily the toughness for each ERC test.

Thirdly, if the effect of adjacent fiber orientation on the delamination resistance is important so that the delamination toughness varies along the crack front of an ERC specimen, the toughness measured in ERC tests should be the smallest one, which is also meaningful. In this case, we can imagine that the points at the crack front with the lowest resistance to delamination could be detected by ERC tests.

Finally, it is important to develop a closed-form expression to determine easily the toughness for each of ERC-I and ERC-II tests.

V.2. Mixed mode I+II

V.2.1. Introduction

Actually, the ERC specimens can also be tested under some mixed mode delamination loadings. For example, a mixed mode I+II delamination test can be realized under tensile load if the two sub-laminates are not symmetrical relative to the crack plane, and a mixed mode I+III test can be realized under a combined torsion and tensile load when the two sub-

laminates are symmetrical relative to the crack plane. In the next parts, only finite element analysis (FEA) will be described, it was carried out in order to study the feasibility of any mixed mode loading on ERC specimens.

Based on the achievement of pure mode I, II and III delamination test with ERC specimen, mixed mode I+II delamination test was proposed in this work, named ERC-I+II for short. FEA was carried out in order to validate the ability of the ERC-I+II test.

This test is modified from ERC-I test, the participation of mode II can be introduced under traction when the specimen is not symmetrical relative to the crack plane. As the result of Poisson's ratio, the elastic strain in the (r, θ) plane for two sub-laminates created by the crack are different under the tensile loading in z direction. That results in a mode II delamination component.

V.2.2. Finite element analysis

In the FE model of mixed I+II delamination test, all of the geometric and material parameters are the same as pure mode ERC tests except for the stacking sequence (0/45/45/0/45/0/0/45/45/0/0/45/0/45/45/0)//crack//(0/45/45/0), which is highlighted in Chapter I. A displacement curve 2mm was employed on both of the loading axes in order to impose a traction load. All the other parameters were set as in ERC-I model.

V.2.3. Results and discussions

Figure V. 11 shows the evolution of G_I , G_{II} and G_{III} normalized by G_T along the crack front obtained by FEA using the VCCT. It is shown that there is no participation of mode I component. A mixed mode I+II delamination is realized indeed. The proportion of mode I over mode II component is approximately 2.0, which is controlled by the stacking sequence of the specimen.

Moreover, the variation of mode I and mode II along the crack front is similar which increases approaching $\pm 45^\circ$ and decreases approaching 0° and 90° . Δ of G_I is approximately 12.5% and Δ of G_{II} is 9.3%, which is relatively small compared to traditional mixed mode I+II delamination tests generally.

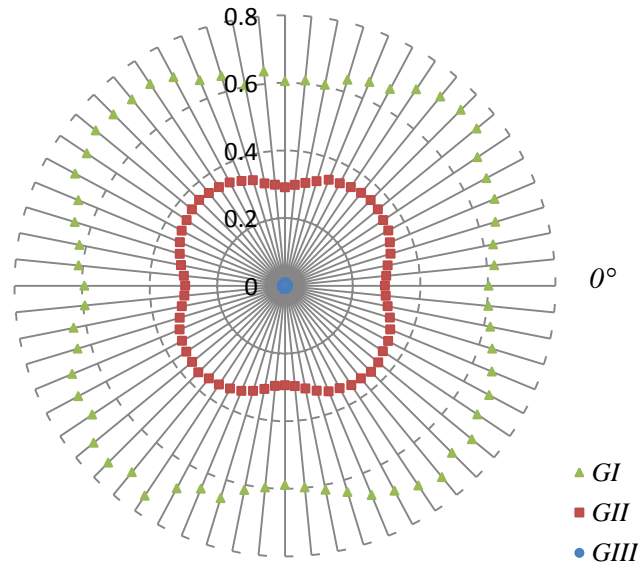


Figure V. 11. Evolution along the crack front of G_I , G_{II} , G_{III} normalized by G_T in ERC-I+II test

V.2.4. Summary

A mixed mode I+II delamination test is proposed by using the ERC specimen. FEA demonstrates that there is no participation of mode III component in this test. The evolution of mode I and mode II is relatively small compared to traditional mode I+II delamination tests generally. The mixed mode ratio in term of G_I/G_{II} is controlled by the stacking sequence of each sub-laminate of the specimen.

V.3. Tests of delamination under mixed mode I+III

V.3.1. Introduction

A mixed mode I+III delamination test was proposed making use of ERC specimen, named ERC-I+III. The mixed mode I+III can be obtained by a combination of traction and torsion using the machine MTS809, when the stacking sequence of the specimen is symmetrical relative to the crack plan, the same as pure mode ERC test.

V.3.2. Finite element analysis

In the FE model of mixed mode I+III delamination test, all the parameters are same as those used in pure mode ERC tests except for boundary conditions. A displacement curve 0.5mm and a rotation curve 0.0025rad were set in order to apply the mixed loading mode. The different mixed mode ratio in terms of G_{II}/G_{III} , can be obtained by combining the tensile and torsion rate.

V.3.3. Results and discussions

The evolution of G_I , G_{II} and G_{III} normalized by G_T along the crack front obtained by FEA using the VCCT is shown in Figure V. 12. A mixed mode I+III delamination is demonstrated to be realized indeed because there is no participation of mode II component. The proportion

of mode I over mode III component is approximately 2.6, which is controlled by the proportion of traction and torsion.

Moreover, the distribution of mode I component along the crack front is uniform while mode III component increases close to $\pm 0^\circ$ and $\pm 90^\circ$ and decreases approaching $\pm 45^\circ$. Δ of G_{III} is approximately 5.0%, which is relatively small compared to traditional mixed mode I+III delamination tests generally.

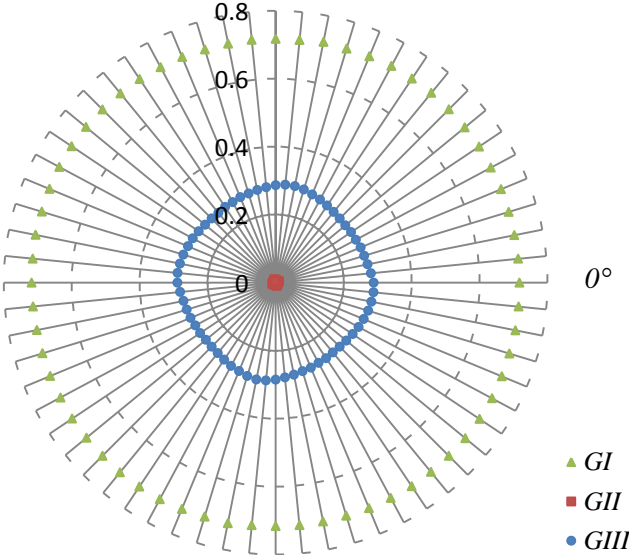


Figure V. 12. Evolution along the crack front of G_I , G_{II} , G_{III} normalized by G_T in ERC-I+III test

V.3.4. Summary

A mixed mode I+III delamination test is proposed by using ERC specimen, which is realized under a combination load of traction and torsion. The proportion of mode I and mode III component can be controlled by modifying the proportion of traction over torsion. The result of FEA show that the distribution of mode I component along the crack front is uniform while mode III component increases close to 0° , $\pm 90^\circ$ and 180° and decreases approaching $\pm 45^\circ$. The evolution of mode III is small with a $\Delta=5.0\%$.

V.4. Delamination tests under mixed mode I+II+III

V.4.1. Introduction

In the former two sections, the mixed mode I+II and mode I+III ERC tests are studied. The combination of these two tests can form a mixed mode I+II+III delamination test, named ERC-I+II+III. In this test, the stacking sequence is the same as ERC-I+II test and the load is the same combination of traction and torsion like that in ERC-I+III.

V.4.2. Finite element analysis

In the FE model of mixed I+II+III delamination test, all the parameters are same as pure mode ERC tests except for the stacking sequence and loading conditions. The stacking sequence is (0/45/45/0/45/0/0/45/45/0/0/45/0/45/45/0)//crack//(0/45/45/0), which is the same as in ERC-

I+II test and highlighted in Chapter I. A displacement curve 0.5mm and a rotation curve 0.0025 were set.

V.4.3. Results and discussions

The evolution of G_I , G_{II} and G_{III} normalized by G_T along the crack front obtained by FEA using the VCCT is shown in Figure V. 13. A mixed mode I+II+III delamination is demonstrated to be realized indeed. The mixed mode ratio in terms of G_I/G_T for the participation of mode I, G_{II}/G_T for that of mode II and G_{III}/G_T for that of mode III is 27%: 11%: 62%, respectively. The mixed ratio can be controlled by the stacking sequence of the specimen, as well as the proportion of traction and torsion.

It is interesting to note that the variation of the mode I and mode II components seems following the same tendency: they decrease close to 0° , $\pm 90^\circ$ and 180° , and increase close to $\pm 45^\circ$. But the variation tendency of mode III component is just on the contrary, it increases while mode I and mode II components decrease. Δ of mode I component is approximately 14.8%, Δ of mode II component is approximately 27.5% and Δ of mode III component is approximately 9.0%. The level of the variation for mode II is too high to be validated.

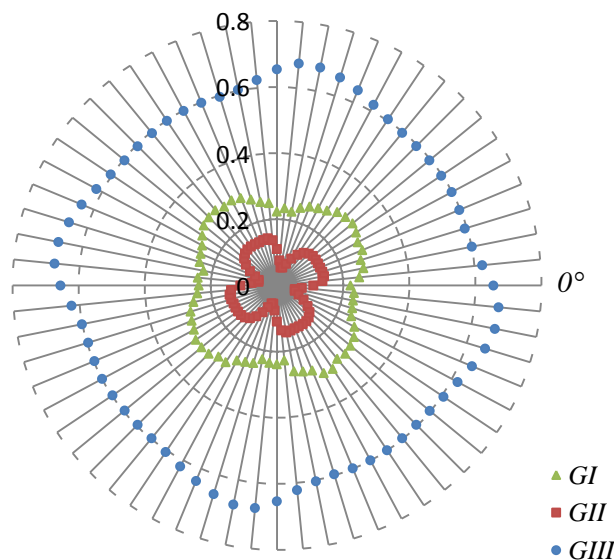


Figure V. 13. Evolution along the crack front of G_I , G_{II} , G_{III} normalized by G_T in ERC-I+II+III test

V.4.4. Summary

A mixed mode I+II+III delamination test is proposed and evaluated by FEA. This test is simple to achieve and easy to control the proportion of three delamination modes. The values of G_I , G_{II} and G_{III} are not constant along the crack front. Especially the level of the variation of G_{II} is too high to be validated. Above all, ERC-I+II+III delamination test is a promising test to characterize mixed mode delamination behavior. Some improvements are necessary in the future work.

V.5. Conclusions

In this chapter, pure mode I and pure mode II delamination tests were achieved using ERC specimens. Their delamination behaviors were investigated by experiments and finite element analysis. Thus pure mode I, II and III delamination tests can be performed on the same ERC specimens. The influence of the geometry of the specimens on the toughness measured can be avoided.

In addition, the evolution of the strain energy release rate along the crack front is fairly uniform, where the average value is more meaningful. It is important to develop a closed-form expression to determine easily the toughness for each ERC test.

Moreover, a mixed mode I+II delamination test using the ERC specimen is investigated by finite element analysis. There is no participation of mode III component in this test. The evolution of mode I and mode II is relatively small compared to traditional mode I+II delamination tests generally. The mixed mode ratio in term of G_I/G_{II} is controlled by the stacking sequence of each sub-laminate.

Based on the success of pure mode I and III tests, a mixed mode I+III delamination test using ERC specimen was investigated by finite element analysis, which is realized under a combination load of traction and torsion. The proportion of mode I and mode III component can be controlled by modifying the proportion of traction over torsion. The distribution of mode I component along the crack front is uniform while mode III component has a small evolution.

Finally, a mixed mode I+II+III delamination test is proposed and evaluated by finite element analysis. This test is simple to achieve and easy to control the proportion of three delamination modes. The values of G_I , G_{II} and G_{III} are not constant along the crack front. Above all, ERC-I+II+III delamination test is a promising test to characterize mixed mode delamination behavior. Some improvements are necessary in the future work.

CHAPTER VI. CONCLUSIONS AND PERSPECTIVES

VI.1. Concluding remarks

The object of the study presented in the thesis is to develop the testing methods for characterization of the delamination behavior under pure modes and mixed modes. Especially most of our attention has been paid to the testing methods for pure mode III delamination. We focus on the onset of crack growth and the distribution of strain energy release rate along the crack front. These are fundamental work for the purpose to establish a general mixed mode delamination criterion with the participation of mode I, mode II and mode III.

Therefore, this work contains not only experimental observations, but also finite element analysis (FEA). Correlation between the results obtained aims, on the one hand to better understand the crack growth especially the crack onset; on the other hand, to propose and improve testing methods, and to propose and validate simple approaches to calculate delamination toughness.

Pure mode III testing methods are studied. Firstly, two kinds of Edge Crack Torsion tests widely used in literature were carried out. The achievements of these tests are compromised by the drawbacks. The main disadvantages are on three aspects: (1) A participation of mode II component cannot be completely eliminated; (2) The distribution of G_{III} along the crack front is not uniform especially near their edges; (3) Nonlinearity is always observed before reaching peak load in a load/displacement curve so that it's not easy to define the critical load. The disadvantages result in difficulty of determination of delamination toughness under pure mode III.

After the study of the two existing tests, a novel original mode III testing methods, named Edge Ring Crack Torsion tests (ERCT), were evaluated by experiment and FEA. The Edge Ring Crack (ERC) specimen was employed in these tests. The circular crack front in the specimen has no extremities so that it can avoid edge effects.

Some factors affecting the evolution of G_{III} along the crack front in ERCT test were studied. It demonstrates that the distribution of G_{III} depends on the superposition of all influence factors, in particular that of device factor and laminate factor. Moreover, the device factor is in a positive correlation with the ratio d/D_{ring} while laminate factor is in a negative correlation with d/D_{ring} . In ERCT test, the main influence factor is the device factor, especially for a specimen with a big d/D_{ring} . Tada's formula is found to be a simple and practical approach to determiner G_{IIIc} , which gives the results good enough only when the variation of G_{III} is small. The optimal ratio d/D_{ring} approximately equal to 0.5 is recommended because the values of G_{III} are nearly uniform and the non-delaminated area is big enough for observation of crack propagation.

Finally, modified ERCT (MERCT) tests in two versions were developed and evaluated based on the FEA, aiming at achieving a pure mode III delamination test with uniform distribution of G_{III} along the circular crack front. The modification on the original ERCT test is concerning especially the geometry of the device parts for transmitting the applying load to

the specimens in an axisymmetrical manner. For ERC-III-1 tests, the load is applied on the surfaces of the specimen through a ring adhesive joint while it is applied at the circular edge of the specimen through the contact between the screws and nicks in the specimen in ERC-III-2 tests. FEA was used to evaluate the quality and the robustness of the tests as well.

The most significant advantages of MERCT tests are shown including:

- The fracture mode does be pure mode III without the participation of mode I or mode II components;
- Uniform distribution of G_{III} along the crack front is achieved. Δ is much smaller than ECT tests and original ERCT test. In fact, a nearly constant value of G_{III} along the crack front is obtained in MERCT tests. Then it's more acceptable to consider the average value, $G_{III-C-FEM}$, as the delamination toughness;
- The agreement between $G_{III-C-Tada}$ and $G_{III-C-FEM}$ is good with a difference of only approximately 8% for both MERCT tests. $G_{III-C-Tada}$ is smaller than $G_{III-C-FEM}$, which guarantees the security when considering $G_{III-C-Tada}$ as the delamination toughness;
- The robustness of MERCT tests is well confirmed. Some defaults introduced by the manufacturing process and test process are generally inevitable. Unwanted fracture mode introduced by different defaults seems no significant. But the variation of G_{III} along the crack front is more sensitive to certain defaults.

In conclusion, MERCT tests are promising testing methods to characterize mode III delamination behavior. In ERC-III-1 test, an unstable crack growth was observed. And in ERC-III-2 test, at onset of delamination the crack propagated a step suddenly, following by a stable crack growth. This phenomenon makes it possible to stop the test before the final fracture of the specimen to observe the crack growth onset.

The application of ERC specimen was also spread into other pure modes delamination tests. Actually, by introducing different loadings, the pure mode I (ERC-I), the pure mode II (ERC-II) and the pure mode III (ERC-III) delamination tests can be performed on the ERC specimens of the same geometry. The influence of the geometry of the specimens on the toughness measured can then be avoided. The tests ERC-I and ERC-II keep most advantages of ERC-III test. The evolution of the strain energy releases rate along the crack front is fairly, where the average value is more meaningful.

Finally, it is important to develop a closed-form expression to determine easily the toughness for both ERC-I and ERC-II tests.

Moreover, it is possible to realize delamination tests of mixed mode I+II, mixed mode I+III and mixed mode I+II+III using ERC specimens. The numerical simulation has shown that no unwanted mode is produced for mixed mode I+II and mixed mode I+III; the distribution of the strain energy release rate is not completely uniform but the variation is limited. As a result the determination of delamination toughness based on average value is still acceptable. In each mixed mode I+II+III test, the proportion of each mode is easy to control so that it is possible to study any mixed mode delamination behavior by using ERC specimens.

It is interesting to note that if the effect of adjacent fiber orientation on the delamination resistance is important and that the delamination toughness varies along the crack front of an ERC specimen, the toughness measured in ERC tests should be the smallest one, which is also meaningful. In this case, we can imagine that the points at the crack front with the lowest resistance to delamination could be detected by ERC tests.

VI.2. Suggestions for future work

As a continuation from the work presented in this thesis, the three pure mode delamination tests using Edge Ring Crack specimens: ERC-I, ERC-II and ERC-III, need further study.

Firstly, the data reduction methods for tests based on ERC specimen need further studies. For ERC-I and ERC-II tests, the development of a closed-form expression based on the plate theory is in progress, and Tada's formula may be improved for ERC-III test by modifying the factor f , which needs more experimental and numerical data. In fact we attempted also to propose a formula based on laminated plate theory for ERC-III. Otherwise, for practical reasons, the experimental compliance calibration methods for ERC tests should be developed. The specimens with different d can be employed in ERC tests while D_{ring} and d_{ring} remains same values. Thus, a series of data (d, C) can be obtained. Then an interpolation method may proposed such as in data (d, C) or ($d/D_{ring}, C$). Recall that all of the data reduction methods mentioned here can be applied to determine precisely the fracture toughness only if the variation of the strain energy release rate along the crack front is small enough. So the optimization of the specimen geometry is necessary.

Next, the observation about the onset of crack growth and the process of propagation should be continued. Actually, limited by experimental conditions and the time, the observation of the crack onset and the crack growth by C-SCAN and of fracture surface by SEM were not realized on all specimens, the former provides the information about the adjacent fiber orientation effects; the later should be essential to understand the damage mechanisms in the tested composite under different delamination loadings. But these observations need to stop the test and unload the specimen in the current conditions of the laboratory. Sometimes, it is difficult to stop the test in time after the critical load is reached in certain ERC tests since delaminating growth is unstable. In these cases, others in-situ non-destructive monitoring methods have to be adopted.

Concerning the mixed mode delamination testing, the methods presented in the thesis needs to be evaluated experimentally. Series of mixed mode I+II, I+III, and I+II+III delamination tests should be carried out with different mixed mode ratios by experiment and finite element analysis.

Finally, it's now possible to propose a semi-empirical criterion to predict delamination resistance for any mixed mode ratio, especially with the participation of mode III. The delamination resistance can be expressed by a general criterion as $f(G_I, G_{II}, G_{III}, G_{IC}, G_{IIC}, G_{IIIC})=0$. It should be based on the measurement of the toughness under pure mode I, pure mode II and pure mode III loading. As in Eq. 21 proposed for mixed mode I+II, the empirical constant can be determined by the interpolation of G_{TC} as a function of the mixed mode ratio G_{II}/G_I . In the same manner, mixed mode I+III constant could be determined by the interpolation of G_{TC} as a function of the mixed mode ratio G_{III}/G_I . Finally, the measurement of the toughness by mode I+II+III delamination testing will allow validating the criterion.

REFERENCE

- [1] Vannucci P, Gong XJ, VERCHERY G. Design with anisotropy. PART2†: Laminates without membrane-flexure coupling. PART3†: Quasi-homogeneous anisotropic laminates. Pap572, Proceedings of the Twelfth International Conference on Composite Materials, ICCM12, Paris, France, July 5th-9th, 1999.
- [2] Vannucci P, Gong XJ. Détermination des stratifiés quasi-homogènes par l'approche polaire, Comptes-rendus Onzième Journées Nationales sur les Matériaux Composites, JNC11, à Arcachon, 18-20 Nov 1998, pp205-214
- [3] Berthelot JM. Composite Materials: Mechanical Behavior and Structural Analysis. New York. 1998.
- [4] Irwin GR, Kies JA. Critical energy rate analysis of fracture strength. Welding Journal Research Supplement. 1954; 33: 193-198.
- [5] Hill R. A theory of the yielding and plastic flow of anisotropic metals. Proc Royal Soc London A, 1948;193:281-297.
- [6] Azzi V, Tsai S. Anisotropic strength of composites. Experimental Mechanics, 17 September 1965;5: 283-288.
- [7] Hoffman O, The brittle strength of orthotropic materials. J Compos Mater 1967;1:200-206.
- [8] Tsai, SW, Wu, EM. A General Theory of Strength for Anisotropic Materials. J Comp Mater 1971;5:58-80
- [9] Hashin Z, Failure criteria for unidirectional fibre composites, ASME Journal of Applied Mechanics, 1980;47, pp.329-334.
- [10] Chang FK, Chang KY. A progressive damage model for laminated composites containing stress concentrations. J Compos Mater, 21, 1987, pp. 834-855.
- [11] Gong XJ. Rupture interlaminaire en mode mixte I+II de composites stratifiés unidirectionnels et multidirectionnels Verre/Epoxy. Thèse de doctorat, Université de Technologie de Compiègne, 1991.
- [12] Gong XJ, Benzeggagh ML. Mixed mode interlaminar fracture toughness of unidirectional Glass/Epoxy composite. Composite Materials: Fatigue and Fracture, 5, ASTM STP 1230, R.H. Martin, Ed., American Society for Testing and Materials, Philadelphia, 1995. pp. 100-123.
- [13] Campilho R, de Moura M, Ramantani D, Morais J, Domingues J. Tensile behaviour of three-dimensional carbon-epoxy adhesively bonded single- and double-strap repairs. International Journal of Adhesion and Adhesives, 2009;29, pp. 678-686.
- [14] Reeder JR. 3D mixed mode delamination fracture criteria-an experimentalist's perspective. In: Proceedings of American Society for Composites, 21st annual technical conference, Dearborn, MI, United States, 17-20 September; 2006.
- [15] NASA, Standard Tests for Toughened Resin Composites. Reference publication 1092, Langley Research Center, 1982.
- [16] ASTM, ASTM standard test method for mode I interlaminar fracture toughness of unidirectional continuous fiber reinforced composite materials.
- [17] Peng LL. Modélisation numérique d'assemblages collés : Application à la réparation de structures en composites. Thèse de doctorat, Université de Bourgogne, 2013.
- [18] Determination of mode-I fracture toughness and non-uniformity for GFRP double cantilever beam specimens with an adhesive layer. Eng Fract Mech 2014;128 :139-156.
- [19] A. J. Russell and K. N. Street, Factors affecting the interlaminar fracture energy of graphite/epoxy laminates, in Progress in Science and Engineering of Composites (Eds T. Hayashi, K. Kawata and S. Umekawa), ICCM-IV, Tokyo, 1982, p. 279.
- [20] Carlsson LA, Gillespie Jr JW, Pipes RB. On the analysis and design of end notched flexure (ENF) for mode II testing. J Compos Mater 1986;20:594-604.
- [21] Yoshihara H. Mode II fracture mechanics properties of solid wood measured by the three-point eccentric end-notched flexure test. Eng Fract Mech 2015; 141:140-151.
- [22] Becht G, Gillespie Jr, JW. Design and analysis of the crack rail shear specimen for mode III interlaminar fracture. Compos Sci Technol 1988;31:143-157.
- [23] Donaldson SL. Mode III intelaminar fracture characterization of composite materials. Compos Sci Technol 1988;32,225-249.
- [24] Martin RH. Evaluation of the split cantilever beam for mode III interlaminar delamination testing. In: O'Brien TK, editor. Composite Materials: fatigue and fracture, vol. 3. Philadelphia, PA: ASTM STP 1110; 1991. p. 243-66.
- [25] Robinson P, Song DQ. The development of an improved mode III delamination test for composites. Compos Sci Technol 1994;52:217-33.

- [26] Sharif F, Kortschot, MT, Martin, RH. Mode III delamination using a split cantilever beam. In: Martin, R.H. (Ed.), *Composite Materials: Fatigue and Fracture*, vol. 5, ASTM STP 1230, ASTM, Philadelphia, 1995. pp. 85–99.
- [27] Szekrényes A. Interlaminar fracture analysis in the GI–GIII plane using prestressed composite beams. *Compos Part A* 2009;40:1621–31.
- [28] Szekrényes A. Improved analysis of the modified split-cantilever beam for mode-III fracture. *Int J Mech Sci* 2009;51:682–93.
- [29] Khoshravan MR, R Moslemi. Investigation on mode III interlaminar fracture of glass/epoxy laminates using a modified split cantilever beam test. *Eng Fract Mech* 2014;127:267–279.
- [30] Szekrényes A. Delamination fracture analysis in the GII–GIII plane using prestressed transparent composite beams. *Int J Solids Struct* 2007;44:3359–78.
- [31] Davidson BD, Sediles FO. Mixed-mode I–II–III delamination toughness determination via a shear–torsion–bending test. *Compos Part A* 2011;42:589–603.
- [32] Lee SM. An edge crack torsion method for mode III delamination fracture testing. *J Compos Technol Res* 1993;15(3):193–201.
- [33] Li J, O'Brien TK. Simplified data reduction methods for the ECT test for mode III interlaminar fracture toughness. *J Compos Technol Res* 1996;18:96–101.
- [34] Liao WC, Sun CT. The determination of mode III fracture toughness in thick composite laminates. *Compos Sci Technol* 1996;56:489–99.
- [35] Li J, Lee SM, Lee EW, O'Brien TK. Evaluation of the edge crack torsion (ECT) test for mode III interlaminar fracture toughness of laminated composites. *J Compos Technol Res* 1997;19:174–83.
- [36] Zhao D, Wang Y. Mode III fracture behaviour of laminated composite with edge crack in torsion. *Theor Appl Fract Mech* 1998;29:109–23.
- [37] Li X, Carlsson LA, Davies P. Influence of fiber volume fraction on mode III interlaminar fracture toughness of glass/epoxy composites. *Compos Sci Technol* 2004;64:1279–86.
- [38] Marat-Mendes R, de Freitas M. Characterisation of the edge crack torsion (ECT) test for the measurement of the mode III interlaminar fracture toughness. *Eng Fract Mech* 2009;76:2799–2809.
- [39] Ratcliffe JG. Characterization of the edge crack torsion (ECT) test for mode III fracture toughness measurement of laminated composites. NASA/TM-2004-213269.
- [40] Pennas D, Cantwell WJ, Compston P. The influence of strain rate on the mode III interlaminar fracture of composite materials. *J Compos Mater* 2007;41:2595–614.
- [41] Pennas D, Cantwell WJ, Compston P. The influence of loading rate on the mode III fracture properties of adhesively bonded composites. *J Reinf Plast Compos* 2009;28:1999–2012.
- [42] de Morais AB, Pereira AB, de Moura MFSF, Magalhães AG. Mode III interlaminar fracture of carbon/epoxy laminates using the edge crack torsion (ECT) test. *Compos Sci Technol* 2009;69:670–6.
- [43] Marat-Mendes R, de Freitas M. Failure criteria for mixed mode delamination in glass fibre epoxy composites. *Compos Struct* 2010;92:2292–2298
- [44] Suemasu H. An experimental method to measure the mode III interlaminar fracture toughness of composite laminates. *Compos Sci Technol* 1999;59:1015–1021
- [45] Browning G, Carlsson LA, Ratcliffe JG. Redesign of the ECT test for mode III delamination testing. Part I: finite element analysis. *J Compos Mater* 2010;44:1867–81.
- [46] de Morais AB, Pereira AB. Mixed mode II + III interlaminar fracture of carbon/epoxy laminates. *Compos Sci Technol* 2008;68:2022–7.
- [47] Pereira AB, de Morais AB. Mixed mode I + III interlaminar fracture of carbon/epoxy laminates. *Compos Part A* 2009;40:518–23.
- [48] de Morais AB, Pereira AB. Mode III interlaminar fracture of carbon/epoxy laminates using a four-point bending plate test. *Compos Part A* 2009;40:1741–6.
- [49] Pereira AB, de Morais AB, de Moura MFSF. Design and analysis of a new sixpoint edge crack torsion (6ECT) specimen for mode III interlaminar fracture characterisation. *Compos Part A* 2011;42:131–9.
- [50] Cricri G, Perrella M, Sessa S, Valoroso N. A novel fixture for measuring mode III toughness of bonded assemblies. *Eng Fract Mech* 2015;138 :1-18
- [51] X.J. Gong, A. Hurez, Y.Y. Ge, L.L. Peng, De Luycker E. Edge Ring Crack Torsion (ERCT) test for pure mode III toughness. *Proceedings of the 19th Journées Nationales sur les Composites (JNC/19)*, Villeurbanne, France, 29 June–1 July 2015.
- [52] Szekrényes A. Application of prestressed transparent composite beams in fracture mechanics *Mechanical Engineering*. *Mech Eng* 2007;51(2):89-97
- [53] ASTM Standard D6671/D6671M. Standard test method for mixed mode I-mode II interlaminar fracture toughness of unidirectional fiber reinforced polymer matrix composites. ASTM International. West Conshohocken, PA;2006, doi:10.1520/D6671_D6671M-06.

-
- [54] Rybicki EF, Kanninen MF. A finite element calculation of stress intensity factors by a modified crack closure integral. *Eng Fract Mech* 1977;9:931-8.
- [55] Krueger R. The Virtual crack closure technique: history, approach and applications. NASA/CR-2002-211628.
- [56] Shokrieh MM, Rajabpour-Shirazi H, Heidari-Rarani M, Haghpanahi M. Simulation of mode I delamination propagation in multidirectional composites with R-curve effects using VCCT method. *Comput Mater Sci* 2012;65:66–73
- [57] Ahna JS, Woo KS. Delamination of laminated composite plates by p-convergent partial discrete-layer elements with VCCT. *Mech Res Commun* 2015;66: 60–69
- [58] Marjanovic M, Meschke G, Vuksanovic D. A finite element model for propagating delamination in laminated composite plates based on the Virtual Crack Closure method. *Compos Struct* 2016;150:8–19.
- [59] Rice JR. A Path Independent Integral and the Approximate Analysis of Strain Concentration by Notches and Cracks. *J Appl Mech* 1968;35:379-386,
- [60] Habbitt, Karlsson, Sorensen. ABAQUS user's manual, version 6.9.1. Pawtucket (USA): Habbitt, Karlsson & Sorensen, Inc. 2009.
- [61] Hamed MA, Nosier A, Farrahi GH. Separation of delamination modes in composite beams with symmetric delaminations. *Mater Des* 2006;27:900-10.
- [62] Barenblatt, GI. Mathematical theory of equilibrium cracks in brittle fracture. *Adv Appl Mech* 1962;7:55-129
- [63] De Morais A.B. Mode I cohesive zone model for delamination in composite beams. *Eng Fract Mech* 2013;109:236–245.
- [64] De Morais A.B. Cohesive zone beam modelling of mixed-mode I–II delamination. *Compos Part A* 2014 ; 64:124–131.
- [65] Xie JW, Waas AM, Rassaian M. Closed-form solutions for cohesive zone modeling of delamination toughness tests. *Inter J Solids Struct* 2016;88–89:379–400.
- [66] Farmand-Ashtiani E, Alanis D, Cugnoni J, Botsis J. Delamination in cross-ply laminates: Identification of tractionseparation relations and cohesive zone modeling. *Compos Sci Technol* 2015;119 :85-92.
- [67] Alfano G, Crisfield MA. Finite element interface models for the delamination analysis of laminated composites: mechanical and computational issues. *Int. J. Numer Meth Engng* 2001;77: 111-170.
- [68] Xu XP, Needleman A, Numerical simulations of fast crack growth in brittle solids. *J Mech Phys Solids* 1994;42:1397-1434.
- [69] Dugdale, DS. Yielding of steel sheets containing slits. *J Mech Phys* 1960;8:100-104.
- [70] Needleman A. A continuum model for void nucleation by inclusion debonding. *Appl Mech* 1987;54: 525-532
- [71] Davidson BD, Krueger R, Koenig M. Effect of stacking sequence on energy release rate distributions in multidirectional DCB and ENF specimens. *Eng Fract Mech* 1996;55(4):557–69.
- [72] Davidson BD, Krueger R, Koenig M. Three-dimensional analysis of centerdelaminated unidirectional and multidirectional single-leg bending specimens. *Compos Sci Technol* 1995;54(4):385–94.
- [73] Samborski S. Numerical analysis of the DCB test configuration applicability to mechanically coupled Fiber Reinforced Laminated Composite beams. *Compos Struct* 2016;152:477-487.
- [74] Theotokoglou EE, Vrettos CD. A finite element analysis of angle-ply laminate end-notched flexure specimens. *Compos Struct* 2006;73:370–379.
- [75] Tada H. Paris CP, Irwin GR. *The stress analysis of cracks handbook*, 1973.
- [76] J.M. Berthelot. *Matériaux composites: comportement mécanique et analyse des structures*. pp. 365-366, 1999.